

## ABSTRACT

Title of Dissertation: **SPECTROSCOPIC AND STRUCTURAL INVESTIGATION OF THE THERMAL EVOLUTION OF UNDOPED AND PHOSPHORUS-DOPED ZnO AND IMPLICATIONS FOR UNIPOLAR AND BIPOLAR DEVICE FABRICATION**

Diane Elizabeth Pugel, Doctor of Philosophy, 2006

Dissertation Directed By: Professor T. Venky Venkatesan  
Department of Physics  
University of Maryland, College Park, MD 20742

The main objective of this dissertation was to explore the structural, electrical, and optical properties of undoped and extrinsically doped thin film and single crystal ZnO under various growth and processing thermal conditions in the context of understanding intrinsic defect formation and extrinsic dopant incorporation.

Undoped  $(000\bar{1})$  ZnO thin films were grown by on-axis RF sputter deposition at a range of temperatures and in oxygen-rich and oxygen-deficient atmospheres. For comparison,  $(000\bar{1})$  ZnO single crystals were thermally processed under similar conditions. Samples were examined for temperature-dependent effects on surface and bulk properties for temperature-dependent changes in structure, semiconducting band gap, and Schottky barrier height in order to isolate temperature regions that may support conditions that minimize defect production.

Phosphorus-doped  $(000\bar{1})$  ZnO thin films were grown and doped ZnO crystals were prepared under the same conditions described above. Phosphorus was selected as a potential *p*-type dopant due to reduced concerns for outdiffusion of the dopant from the host crystal. Films were grown via sputter deposition. Crystals were prepared via planar (vapor) doping.

By investigating undoped ZnO, this work expands current understanding of the fabrication of ZnO-based unipolar devices, such as Schottky diodes. To this end, the structure (surface and bulk), composition, optical, and electrical properties of ZnO single crystals were investigated as a function of annealing temperature and atmosphere. Near-surface diffusion of Zn atoms was found to influence the Schottky barrier height. Annealing conditions that minimize donor defect states, as detected by photoluminescence, were found.

By investigating extrinsically doped ZnO, this work sheds light on the feasibility of bipolar device fabrication using ZnO. For film growth, we found a narrow window of deposition temperature and pressure that optimizes crystallinity and transmission in the ultraviolet spectrum for the preparation of *p*-type doped material. For single crystals, we found optimal conditions for *p*-type doping ZnO using phosphorus vapor. Results from Hall measurements of these doped single crystals allowed for a revision of the limits defined by previously existing experimental results in the “failure to dope” rule for ZnO.

**SPECTROSCOPIC AND STRUCTURAL INVESTIGATION OF  
THE THERMAL EVOLUTION OF UNDOPED AND  
PHOSPHORUS-DOPED ZnO AND IMPLICATIONS FOR  
UNIPOLAR AND BIPOLAR DEVICE FABRICATION**

By

Diane Elizabeth Pugel

Dissertation submitted to the Faculty of the Graduate School of the  
University of Maryland, College Park, in partial fulfillment  
of the requirements for the degree of  
Doctor of Philosophy  
2006

Advisory Committee:  
Professor T. Venkatesan, Chair  
Professor Robert Anderson  
Professor Michael Fuhrer  
Professor Richard Greene  
Professor Ichiro Takeuchi

© Copyright by  
Diane Elizabeth Pugel  
2006

## Acknowledgements

Many people contributed to this thesis, directly and indirectly. I extend my gratitude to all of you. If you're reading this and you're not on the list, consider it an error of my mind and not of my heart:

- Professor Venkatesan, you've been a lighthouse to me throughout my graduate career here. Thank you for always taking the time to talk with me, even when it was 3AM in India. Thank you also for being a guru in and out of physics. You have taught me many things about life as well as physics.
- Professor Greene, Director of the Center for Superconductivity and all-around nice guy. Thank you and the Center for Superconductivity for your support and for such great facilities.
- Professor Chris van de Walle, Materials Department from the University of California at Santa Barbara—I am grateful for the time and effort that you put in to reading sections of this dissertation and providing feedback associated with the more theoretical portions. It was an honor to have the opportunity to interact with you.
- Dr. Carl M. Stahle, Detector Systems Branch at NASA Goddard Space Flight Center. A heartfelt thank you for believing in me from the very beginning. It is because of your thoughtful nature that I decided to believe in the physics community again.
- Dr. Laddawan R. Miko, Detector Systems Branch at NASA—thank you for your support over the years as a scientist and a mentor.

- Dr. R.D. Vispute, for his sage advice and support.
- My research group: Shiva Hullavarad, Darshan Kundaliya and Sanjay Shinde answered my questions, helped me feed the trips and indulged me in Indian food. I also thank their families who provided much joy and laughter in my years in the group. I consider their kind efforts to teach me about the different aspects of Indian culture the second half of my education, ahaa?
- To the leaders at Goddard Space Flight Center that I've been fortunate to work with in different capacities: Ed Weiler, Dolly Perkins, Mike R., Bruce Butterworth, Mark Matsumura, Peter Hughes Peter Shu, Shelly Standiford, Janine Dolinka and countless others—thank you for your support, guidance and enthusiasm. It is truly an honor to work with such talented and thoughtful people.
- The many undergrads that I have worked--Alexandra Curtin, Al Godinez, Greg Langham, Arun Lukyx and Patrick Valdivia—I've watched you mature over the years--you are living proof that the next generation of scientists and engineers will hold themselves to high standards.
- Dr. Bindhu Varughese for her assistance in XPS measurements
- Dr. Shankar Dhar for his assistance in RBS measurements and fruitful discussions surrounding the single crystal work and for his critical mind.
- Dr. Satish Ogale for his inspiring leadership, presentations and support.
- Visitors to our group: Professor M.S.R. Rao, IIT-Chennai; Professor Wegdan Ramadan—Alexandria, Egypt; and Dr. Kulkarni for their friendship and scientific insights.

- My fellow graduate students—Shige Fujimoto, Tarek Ghanem, and now-Doctors Maria Aranova, Todd Britlinger, and Benga Famudo. Thank you for your welcoming spirit when I came to UMD and for bringing your joyful spirits into the lab.
- The postdocs I interacted with in CSR—Alexandre Zimmers: I will never look at Stevie Wonder the same way again; Rupert Lewis: thank you for keeping me on my toes with your puns.
- The faculty in CSR—Professors Anderson, Fuhrer, and Takeuchi for taking interest in my work and serving on my committee; Thank you to Professors Lobb and Wellstood for asking critical questions during my seminars.
- Aerospace Engineering Professors David Akin and Mary Bowden for bringing out my curiosity towards the design and construction of spacecraft.
- The Staff at CSR—to Brian Straughn and Doug Bensen for sharing their wisdom and always lending a kind ear; to Cleopatra White, Brian Barnaby and Grace Sewall always made the mundane tasks of paperwork enjoyable and Belta Pollard, who let me write in her “hideout” and was a source of great wisdom.
- In the Physics Department: Dr. Nicholas Chant always surprised me with his interest in making my life easier as a graduate student. I kept waiting for him to make it harder, but nope...he’s a nice guy with his students’ interests in his heart. Thank you. Ms. Jane Hessing is simply a superstar. I can’t express my gratitude enough to her for her persistence, her support and effort in helping me with registration and course issues. Ms. Linda O’Hara always brought levity to the situations at hand (thanks for the trips to the Dairy!). Jesse Anderson, for bringing

lightness to the world of red tape. Sr. Godinez--por supuesto, te doy mil gracias de mi corazon por todo!

- To my PHYS 838 Classmates—thank you for all of your questions and input during my seminar talks.
- My colleagues at Goddard—Dan Krieger, Carolyn Casey, Michael Hartman, Brian Ottens, Dave Franz, Audrey Ewin, the UV Group and the countless others in and out of 553 who inspired me, supported me and just plain old made me laugh along the way. Thank you for your gleeful consumption of my science-inspired desserts.
- To all the kids that I interacted with during science outreach at Goddard & at UMd. Your laughter and smiles are a constant reminder to me that it is in the joyful pursuit of learning that we come to understand the beauty of the world around us.
- To Gina Buntz, Thomas Lux, and Edwina Burness who encouraged me, as a physicist, to continue in my pursuit of the arts and bring together the beauty in physics with the beauty of dance and poetry. You've enriched my soul.
- To Mr. Ward for encouraging my return to physics.
- To the nation's (and possibly the world's) best women's rugby team: the Washington D.C. Furies. Thank you, dear Furballs for your sisterhood, your sportswomanship and for making playing wing and fullback such a blast. It is an honor to play with women of your caliber.
- To the American Association for the Advancement of Science (AAAS): Jinny Stern, Latasha Mason and of course, Lauren Summers, for their financial and emotional support of my efforts.

- A scatological shout out from Ace to those in the know—David Tobias, Sudeep Kumar Dutta, and Josh Higgins—thank you for making me laugh.
- My dear friends who always found reasons to make me laugh and provided endless encouragement. My heartfelt thanks to William Ratcliff II, Aileen Wang, Vivian Crespo (Think piononos!), the Crespos, and Toljagas.
- My family: the Pugels and Plečniks, both past and present. I am lucky to have been born into a family with histories of soulful pursuits for knowledge coupled with a deep love for humanity. For this, I feel blessed. Thank you for teaching me how to live & love all that life may bring and for teaching me to find the lessons that are to be learned in the midst of hardships rather than focus on the hardship itself.
- Special thank yous go out to my dear 7-year-old niece, Elise, Tara Venkatesan, Dan Krieger, Bernice Weiss, and Carolyn Casey for their positive energy during the final stages of completing this work.



- And , thank you.

# Table of Contents

<b>Acknowledgements</b> .....	<b>ii</b>
<b>List of Tables</b> .....	<b>x</b>
<b>List of Figures</b> .....	<b>xi</b>
<b>List of Acronyms and Abbreviations</b> .....	<b>xv</b>
<b>Chapter 1: Background and Overview</b> .....	<b>1</b>
<b>1.1 Basic Properties of ZnO</b> .....	<b>1</b>
<b>1.2 Basic Notions of Defects and Doping</b> .....	<b>3</b>
1.2.1 Intrinsic Defects .....	3
1.2.2 Extrinsic Defects .....	3
1.2.3 Thermodynamics of Defect Formation .....	5
1.2.4 Defect Energy Levels .....	8
<b>1.3 Doping Asymmetry of the Wide Band Gap Semiconductors</b> .....	<b>8</b>
<b>Chapter 2: Doping ZnO</b> .....	<b>13</b>
<b>2.1 n-type Doping ZnO</b> .....	<b>13</b>
2.1.1 Intrinsic n-type doping .....	13
2.1.2 Extrinsic n-type doping .....	14
<b>2.2 p-type Doping ZnO</b> .....	<b>14</b>
2.2.1 The Challenges Associated with p-type Doping ZnO .....	15
2.2.2 Intrinsic p-type doping .....	18
2.2.3 Extrinsic p-type doping .....	20
2.2.4 Group V Elements as Extrinsic p-type Dopants for ZnO.....	22
<b>Chapter 3: Conceptual Map of this Effort</b> .....	<b>30</b>
<b>Chapter 4: Thermal Evolution of Bulk Properties of Undoped ZnO Thin Films</b> .....	<b>32</b>
<b>4.1 Introduction and Approach</b> .....	<b>32</b>
4.1.1 The Role of Low Deposition Temperatures .....	33
4.1.2 The Role of $p(O_2)$ .....	33
4.1.3 The Role of Strain.....	36
<b>4.2 Growth Parameter Influence on Structural Properties</b> .....	<b>39</b>
4.2.1 Crystallinity .....	39
4.2.2 c-axis length.....	42
4.2.3 c-axis Strain.....	44
<b>4.4 Relationship between Strain and Optical Properties</b> .....	<b>45</b>
4.4.1 Background.....	45

4.4.2	<i>Results</i> .....	49
4.4.3	<i>T<sub>dep</sub> Influence on the Distribution of Defect States</i> .....	52
4.5	<b>Conclusions</b> .....	53

## **Chapter 5: Thermal Evolution of Surface and Bulk Properties of Undoped ZnO Single Crystals.....54**

5.1	<b>Background</b> .....	54
5.2	<b>Approach</b> .....	56
5.3	<b>Results</b> .....	58
5.3.1	<i>Surface Roughness</i> .....	58
5.3.2	<i>Schottky Barrier Height</i> .....	63
5.3.3	<i>X-Ray Photoelectron Spectroscopy</i> .....	66
5.3.4	<i>Rutherford Backscattering Spectrometry</i> .....	73
5.3.5	<i>X-ray Diffraction</i> .....	76
5.3.6	<i>Photoluminescence Spectroscopy</i> .....	82

## **Chapter 6: Phosphorus Dopant Incorporation in ZnO Thin Films and Single Crystals .....91**

6.1	<b>The History of Phosphorus as a p-type Dopant in ZnO</b> .....	91
6.1.1	<i>Thin Film Doping</i> .....	91
6.1.2	<i>Single Crystal Doping</i> .....	92
6.2	<b>P<sub>2</sub>O<sub>5</sub> as a Dopant Material</b> .....	92
6.2.1	<i>Basic Properties</i> .....	92
6.3	<b>Phosphorus-Doped Thin Film Deposition</b> .....	94
6.3.1	<i>Background</i> .....	94
6.3.2	<i>Growth Parameter Influence on Structural Properties of P-Doped Films</i> .....	95
6.3.3	<i>Relationship between Strain and Optical Properties</i> .....	95
6.3.4	<i>Electrical Properties</i> .....	105
6.4	<b>Planar Doping of P<sub>2</sub>O<sub>5</sub> into ZnO Single Crystals</b> .....	105

## **Chapter 7: Implications for Unipolar and Bipolar Device Fabrication.....110**

7.1	<b>Unipolar Devices</b> .....	110
7.2	<b>Bipolar Devices</b> .....	111
7.2.1	<i>Updating the Experimental Limits of the Failure to Dope Rule</i> .....	111
7.2.2	<i>Single Crystal Planar Doping Conditions</i> .....	114
7.2.3	<i>Phosphorus-Doped Thin Film Growth Conditions</i> .....	115

## **Appendices .....117**

<b>Appendix 1: RF Sputter Deposition</b> .....	118
A1.1 <i>Introduction to Sputter Deposition</i> .....	118

A1.2	Experimental Details.....	119
<b><i>Appendix 2: Atomic Force Microscopy.....</i></b>		<b>124</b>
A2.1	Introduction.....	124
A2.2	Experimental Details.....	124
A2.3	Analysis.....	125
<b><i>Appendix 3: UV Spectroscopy.....</i></b>		<b>126</b>
A3.1	Introduction.....	126
A3.2	UV-Visible Spectrophotometry—Experimental Details & Analysis .....	126
A3.3	Photoluminescence—Theory and Experimental Details .....	129
<b><i>Appendix 4: Rutherford Backscattering Spectrometry and Channeling.....</i></b>		<b>131</b>
A4.1	Introduction.....	131
A4.2	Experimental Details.....	135
<b><i>Appendix 5: X-ray Photoelectron Spectroscopy.....</i></b>		<b>137</b>
A5.1	Introduction.....	137
A5.2	Experimental Details.....	138
A5.3	Analysis.....	139
<b><i>Appendix 6: Four-Circle X-ray Diffraction.....</i></b>		<b>141</b>
A6.1	Introduction.....	141
A6.2	Experimental Details.....	142
<b><i>Appendix 7: I-V and Schottky Barrier Measurements.....</i></b>		<b>144</b>
A7.1	Introduction.....	144
A7.2	Experimental Details.....	145
A7.3	Analysis.....	146
<b>Suggested Interview Questions for the Dissertation Defense ....</b>		<b>148</b>
<b>Bibliography .....</b>		<b>149</b>

## List of Tables

Table 1:	Basic Properties of ZnO.....	2
Table 2:	Oxidation states of Group V elements.....	24
Table 3:	Electronegativity difference and % ionic character of Zn, O and dopant elements.....	24
Table 4:	Comparison of ionic radii for Zn, O and candidate dopant material.....	25
Table 5:	List of potential competitive phases & their conductivity types.....	26
Table 6:	Common peaks found in ZnO photoluminescence spectra.....	83
Table 7:	Comparison of Undoped and P <sub>2</sub> O <sub>5</sub> -planar doped ZnO transport properties..	107

## List of Figures

Figure 1	Hexagonal lattice structure of ZnO.....	2
Figure 2	p-type doping Silicon: (a) Lattice structure of Si, showing the position of the boron dopant. (b) Effect of p-type doping Silicon on band structure. ....	4
Figure 3	Band diagram for II-VI and I-II-VI <sub>2</sub> compounds. Values for the valence band maximum and conduction band minimum energies are indicated by the lower and upper numbers in a given column, respectively. Dashed lines indicate $E_{Fermi, Experimental}^{(pin, n)}$ (upper dashed line) and $E_{Fermi, Experimental}^{(pin, p)}$ (lower dashed line) calculated from theoretical first principles. Short solid lines indicate $E_{Fermi, Theoretical}^{(pin, n/p)}$ “C/D” indicates that the position of the pinned level is consistent with data. ....	12
Figure 4	Predicted energy levels of anion impurities introduced into different wurtzite lattices vs. energy of a given element’s p-orbital <sup>70</sup> .....	21
Figure 5	Conceptual map of this investigation.....	30
Figure 6	Schematic depiction of the formation energies of general intrinsic donors	34
Figure 7	Left—Schematic of epitaxial film layer under tensile strain. Right—Schematic of epitaxial film layer under compressive strain. Interface between film and substrate is denoted by a dotted line. ....	37
Figure 8	Rocking curve data for (0002) orientation of undoped ZnO thin films grown on (000-1) Al <sub>2</sub> O <sub>3</sub> for Ar-rich and O-rich ambients at various T <sub>dep</sub> .....	41
Figure 9	(a)(0002) FWHM vs. T <sub>dep</sub> and (b) c-axis length vs T <sub>dep</sub> for undoped ZnO thin films grown in either Ar-rich or O-rich ambients at 16 mTorr.....	43
Figure 10	$\epsilon_{zz}$ vs. T <sub>dep</sub> for undoped ZnO thin films grown in either oxygen rich or argon rich atmospheres. ....	44
Figure 11	Schematic of band structure as perturbed by strain .....	48
Figure 12	% Transmission vs. $\lambda$ (excitation wavelength) for undoped ZnO grown at various T <sub>dep</sub> for Ar-rich (top) or O-rich (bottom) atmospheres. Insets: Transition width $\Delta\lambda$ vs. T <sub>dep</sub> . ....	50
Figure 13	Band Gap ( $E_{gap}$ ) vs. T <sub>dep</sub> for undoped ZnO films grown in either Ar-rich or O-rich atmospheres. ....	51

Figure 14	Band Gap ( $E_{\text{gap}}$ ) vs. $\epsilon_{zz}$ for undoped ZnO films grown in either Ar-rich or O-rich atmospheres. ....	52
Figure 15	Schematic of the approach and techniques used in this chapter. ....	56
Figure 16	(a) RMS roughness as a function of $T_{\text{ANNEAL}}$ for ZnO single crystals annealed in air. Error bars are within the size of the points on the plot. AFM surface morphology plots for (b) Unannealed single crystal ZnO, (c) 400°C and (d) 1000°C anneals. Diagonal lines are artifacts of the scanning process. ....	60
Figure 17	AFM images of samples annealed non-oxidizing ambients as a function of $T_{\text{ANNEAL}}$ . ....	61
Figure 18	r.m.s. roughness for both non-oxidizing ambients—argon and vacuum. ....	62
Figure 19	Percent change in r.m.s. roughness, relative to unannealed samples for all three annealing ambients. ....	62
Figure 20	Schottky barrier height ( $\phi_B$ ) vs. $T_{\text{Anneal}}$ for air annealed crystals. ....	64
Figure 21	$T_{\text{ANNEAL}}$ dependence of Schottky barrier for argon- and vacuum- annealed samples. ....	65
Figure 22	(a) O1s spectra for ZnO samples annealed in air at $T_{\text{anneal}} =$ unannealed, 400, 600 and 1000°C. (b) An example of an O1s spectrum, uncorrected for adventitious carbon peak $E_B$ , with fits. ....	68
Figure 23	(a) O1s mass concentration of off-stoichiometry ZnO (ZnO, squares), on-stoichiometry ZnO (circles) and Zn(OH) <sub>2</sub> (triangles) as a function of $T_A$ . (b) Zn 2p mass concentration vs. $T_A$ . ....	69
Figure 24	Comparison of total oxygen mass concentration (squares) with total zinc mass concentration (circles) as a function of annealing temperature. Mass concentration for oxygen and for zinc were calculated independently using the approach discussed in Appendix 5. ....	72
Figure 25	RBS Spectra for air-annealed single crystals at various $T_{\text{ANNEAL}}$ . ....	74
Figure 26	Channeling yield vs. annealing temperature for single crystal ZnO annealed in air. ....	74
Figure 27	RBS channeling yield for argon- and vacuum-annealed samples. ....	76
Figure 28	Strain vs. $T_{\text{anneal}}$ for air-annealed (a), argon-annealed (b) and vacuum-annealed samples (c). ....	77

Figure 29	c-axis FWHM vs. $T_{\text{Anneal}}$ for (a) air-, (b) argon- and (c) vacuum-annealed samples. ....	80
Figure 30	PL spectra of band edge peak for different $T_{\text{ANNEAL}}$ for vacuum-annealed samples. ....	85
Figure 31	PL spectra of band edge peak for different $T_{\text{ANNEAL}}$ for air-annealed samples. ....	86
Figure 32	Green band region of PL spectrum for undoped single crystal ZnO annealed in air (top) and argon (bottom) at a range of $T_{\text{Anneal}}$ .....	89
Figure 33	Green band region of PL spectrum for undoped single crystal ZnO annealed in vacuum at a range of $T_{\text{Anneal}}$ .....	90
Figure 34	ZnO-P <sub>2</sub> O <sub>5</sub> phase diagram. Adapted from Reference .....	93
Figure 35	ZnO-Phosphorus phase diagram. Adapted from Of the $T_{\text{dep}}$ studied in the thin film section, those on the phase diagram are labeled with .....	93
Figure 36	(0002) FWHM vs. $T_{\text{deposition}}$ for Phosphorus-doped ZnO thin films (% Phosphorus = 1, 2, 5, 10% at. wt.) grown in an (a) an argon-rich atmosphere (b) oxygen-rich atmosphere.....	97
Figure 37	$\epsilon_{zz}$ vs. $T_{\text{deposition}}$ for Phosphorus-doped ZnO thin films (% Phosphorus = 1, 2, 5, 10% at. wt.) grown in an (a) argon-rich atmosphere or (b) an oxygen-rich atmosphere.....	98
Figure 38	$E_{\text{gap}}$ as a function of % phosphorus (RBS) for oxygen-rich grown samples (top) and argon-rich grown samples (bottom) .....	102
Figure 39	$E_{\text{gap}}$ vs. $T_{\text{deposition}}$ for Phosphorus-doped ZnO thin films (% Phosphorus = 1, 2, 5, 10% at. wt.) grown in an argon-rich atmosphere (top) or an oxygen-rich atmosphere (bottom). ....	103
Figure 40	$\Delta\lambda$ vs. $T_{\text{deposition}}$ for various % P doped films grown under Ar-rich deposition conditions (top) and Oxygen-rich deposition conditions (bottom) .....	104
Figure 41	Device geometry of planar-doped p-n junctions.....	107
Figure 42	(a) Comparison of I-V Characteristics of undoped ZnO and phosphorus-doped ZnO, both prepared by heating in air at 800°C for 12 hours, followed by contact deposition (described in the text) and subsequent anneal at 600°C, 25 min. (b) I-V Characteristics of p-doped ZnO with room lights on (solid, red) and off (dashed, black). ....	108

Figure 43	Modified band diagram from Figure 4. Modification schematically reflects a change of $E_{Fermi,Experimental}^{(pin,p)}$ (thick solid line) value as recalculated in the text. Originally, $E_{Fermi,Experimental}^{(pin,p)}$ appeared at the dashed line labeled “C/D” .....	114
Figure 44	Top view schematic of rf sputter deposition chamber and associated electronics and gas handlers.....	122
Figure 45	Photograph of rf sputter chamber and electronics rack .....	123
Figure 46	UV-Visible Spectroscopy, Transmission Mode. The beam path is indicated by the cyan arrows and the position of Reflectance Mode attachment is indicated by a gray box around the sample and reference. (Adapted from W. Yang, thesis).....	128
Figure 47	Top view schematic of PL system. ....	130
Figure 48	Diagram of RBS in randomly aligned mode for a binary system (such as ZnO). Arrows indicate incident and backscattered energy.....	132
Figure 49	RBS Channeling Modes. (a) Channeling in a perfectly aligned lattice. (b) Channeling in an imperfect lattice. The backscattered element, a consequence of the imperfection of the lattice is represented by the dashed arrow.....	135
Figure 50	Photograph of Pelletron accelerator and RBS beam line (Courtesy of S. Dhar) .....	136
Figure 51	Top view schematic of X-ray Photoelectron Spectroscopy setup. ....	138
Figure 52	Diagram of XRD four-circle. ....	143
Figure 53	Diagram of band-bending and Schottky barrier for various applied voltages .....	145

## List of Acronyms and Abbreviations

A/D	Analog to Digital
AFM	Atomic Force Microscopy
AX	acceptor defect complex
DC	Direct Current
DX	donor defect complex
eV	electron volts
FWHM	full width at half-maximum
I-V	Current-Voltage
JCPDS	Joint Committee on Powder Diffraction Standards
nm	nanometers
O <sub>i</sub>	oxygen interstitial
p(O <sub>2</sub> )	oxygen pressure
PID	Proportional-Integrative-Derivative
PL	Photoluminescence Spectroscopy
PLD	pulsed laser deposition
RBS	Rutherford Backscattering Spectrometry
RF	radio frequency
T <sub>anneal</sub>	annealing temperature
T <sub>dep</sub>	deposition temperature
UHV	Ultrahigh Vacuum
UV	ultraviolet
UV-Vis	UV-Visible Spectrophotometry
V <sub>o</sub>	Oxygen vacancy
V <sub>Zn</sub>	Zn vacancy
XPS	X-ray Photoelectron Spectroscopy
XRD	X-ray Diffraction
Zn <sub>i</sub>	Zn interstitial

# Chapter 1: Background and Overview

## 1.1 Basic Properties of ZnO

ZnO is a wide band gap optoelectronic material belonging to the II-VI family of semiconductors. It was discovered during the Bronze Age<sup>1</sup>. The band gap of undoped ZnO is direct and is equal to 3.37 eV<sup>2</sup>. It is transparent to visible light.

ZnO has received increased attention over the past few years because of its ease in fabrication<sup>3,4</sup>, its presumed radiation hardness properties (attributed to its large displacement energy = 57 eV)<sup>5</sup>, availability of large-area substrates<sup>6</sup> and most importantly, its wide band gap, which makes it an excellent candidate for producing unipolar devices (for example, Schottky detectors) and bipolar devices (for example, ultraviolet (UV)-emitting diodes). The challenge in producing unipolar and bipolar devices lies in the ability to control the *n*-type conductivity of ZnO and the ability to reliably *p*-type dope ZnO.

ZnO has a near-perfect hexagonal wurtzite structure, as depicted in Figure 1, consisting of Zn and O planes which are alternately stacked along the *c*-axis direction. The surface of ZnO may be Zn terminated ([0001]-oriented) or oxygen terminated ([000 $\bar{1}$ ]-oriented). Each Zn atom is tetrahedrally coordinated to four oxygen atoms. ZnO is a near-perfect hexagonal lattice in the sense that the ratio between lattice parameters, *c/a*, is 1.601 as compared to the standard 1.633 value for a hexagonal lattice. This is only a 2% deviation from the ideal hexagonal lattice. The lattice parameters and the basic properties of ZnO are listed in Table 1.

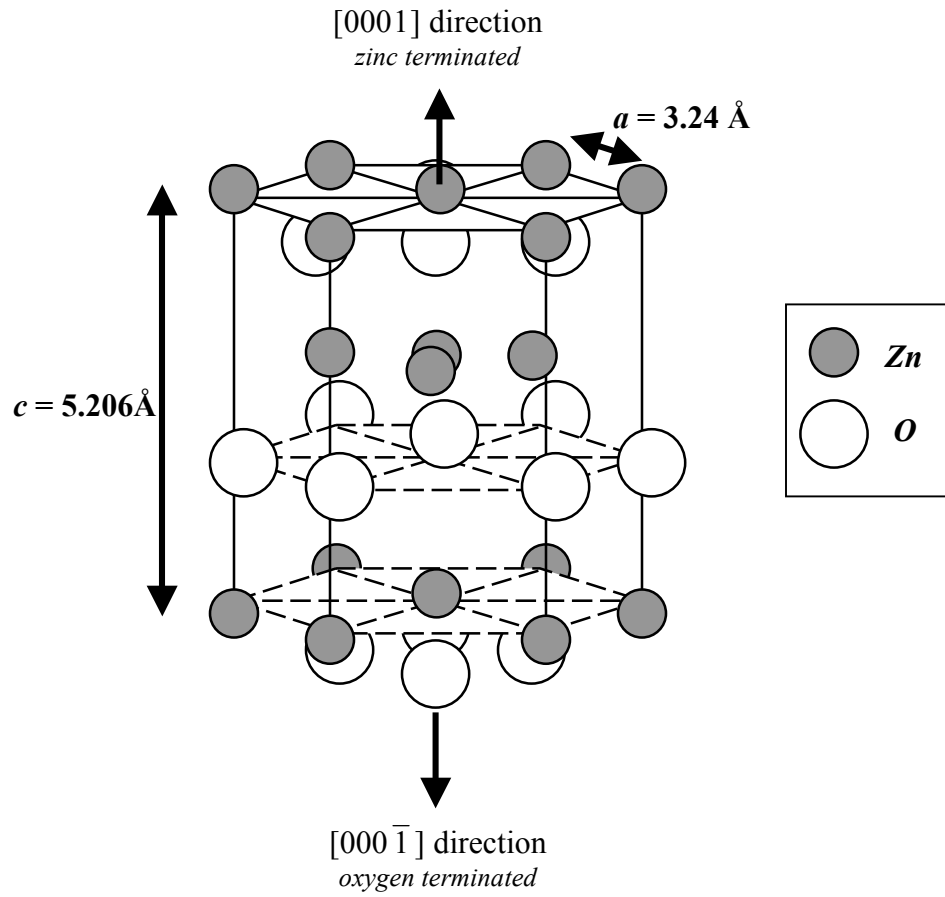


Figure 1 Hexagonal lattice structure of ZnO

Table 1: Basic Properties of ZnO

Crystal System	<i>Wurtzite</i>
Lattice Constant	$a = 3.2465 \text{ \AA}, c = 5.2066 \text{ \AA}$
Sublimation Point	$1975 \pm 25 \text{ }^\circ\text{C}$
Density	$5.665 \times 10^3 \text{ kg/m}^3$
Dielectric Constant	$\epsilon_{11} = 8.55, \epsilon_{33} = 10.20 \times 10^{-11} \text{ F/m}$
Band Gap	$E_{gap} = 3.37 \text{ eV}$
Optical Transparency Range	$0.4 - 2.5 \text{ }\mu\text{m}$

## **1.2 Basic Notions of Defects and Doping**

### ***1.2.1 Intrinsic Defects***

In its native state, an undoped semiconductor will contain defects that arise during growth and fabrication processes. These intrinsic or native defects may be one-dimensional—point defects—missing atoms (vacancies), additional atoms appearing in sites other than substitution sites (interstitials) and atoms in the wrong place (antisites—e.g. a cation sitting on an anion site). Defects may also have higher dimensions—such as dislocations, grain boundaries, twins, or stacking faults.

### ***1.2.2 Extrinsic Defects***

Left in their native, undoped, state most semiconductors would have few electrical applications since on average, the electrical conductivity of a semiconductor is lower than that of a metal. For this reason, it is necessary to introduce defects into a semiconductor, *extrinsic defects*, which modify the electrical conductivity. These defects can be introduced as single elements or multiple elements (*co-doping*).

Consider the example of substituting boron into a silicon lattice (Figure 2 (a)). Silicon has a valence state of +4 and boron has a valence state of +3. In the undoped state, each silicon atom forms four covalent bonds, one with each of its nearest neighbors. Boron has three valence electrons, so it can complete bonding only if it takes an electron from the valence band associated with the Si-Si bond. This leaves behind a hole that is able to participate in conduction. Boron is called an *acceptor* in Si

because it accepts an electron from the valence band, leaving behind mobile holes. The hole can be ionized from the valence band (Figure 2(b)).

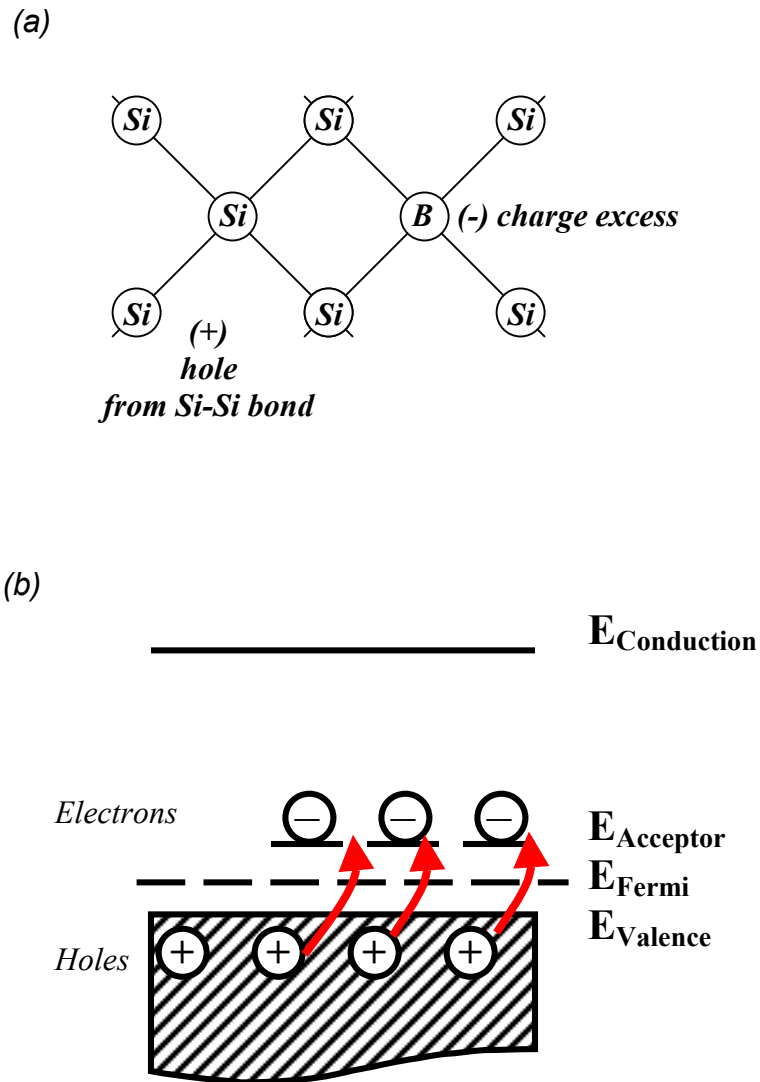


Figure 2 p-type doping Silicon: (a) Lattice structure of Si, showing the position of the boron dopant. (b) Effect of p-type doping Silicon on band structure.

The ionization energy of the acceptor impurity is modeled as an analog to the hydrogen atom with the dielectric constant ( $\epsilon$ ) and effective mass ( $m^*$ ) of the host

material. A hydrogen atom has a binding energy of  $\frac{-e^4 m}{2(4\pi\epsilon_0 \hbar)^2}$ . For the semiconductor,  $e^2$  is replaced by  $e^2/\epsilon$  and  $m$  by the effective mass,  $m^*$ . The acceptor ionization energy is written as:

$$E_{acceptor} = \frac{e^4 m^*}{2(4\pi\epsilon\epsilon_0 \hbar)^2} \quad (1.1)$$

Analogously, the Bohr radius of the hydrogen atom,  $[(4\pi\epsilon_0 \hbar^2)/me^2]$ , is converted to the Bohr radius of an acceptor impurity<sup>7</sup>:

$$a_{acceptor} = \frac{4\pi\epsilon\epsilon_0 \hbar^2}{m^* e^2} \quad (1.2)$$

### ***1.2.3 Thermodynamics of Defect Formation***

The concentration of a defect (intrinsic or extrinsic) is determined by its formation energy. The formation energy is influenced by the concentration of existing defects in the host material, the host's stoichiometry, dopant concentration and other growth/processing conditions (for example,  $p(O_2)$  and deposition temperature). Basic thermodynamics can be used to write out the formations for defects in a semiconductor.

#### **1.2.3.a Formation Energy: Uncharged Defects**

Introducing an uncharged impurity into a host crystal,  $A^0$ , depends upon the chemical potential of the impurity,  $\mu_A$ , because the impurity is taken from a reservoir

with finite energy. The formation energy required to introduce an uncharged impurity into a host lattice can be written as<sup>8</sup>:

$$\Delta E(A^0) = E^{host}(A^0) - E^{total}(0) - \mu_A - \mu_{host} \quad (1.3)$$

Where  $E^{host}(A^0)$  = the total energy of the host crystal containing one uncharged impurity;  $E^{total}(0)$  = the total energy of the host crystal without an impurity;  $\mu_A$  = the chemical potential of the impurity in the reservoir from which it is taken and  $\mu_{Host}$  = the energy of the host atom(s) in its reservoir. For a binary compound,  $\mu_{Host} = \mu_{Anion} + \mu_{Cation}$ .

### 1.2.3.b Formation Energy: Charged Defects

Introducing a charged defect incurs two energy costs to the host lattice:

- (1) Energy is required to ionize a neutral defect state. (For example, the acceptor,  $A^0$ , could ionize into a positively charged donor state,  $A^+$ )
- (2) Energy to extract/replace a charge into the Fermi sea.

Knowing this, the formation energy for introducing a charged donor impurity,  $A^+$ , to a host lattice can be written as:

$$\Delta E(A^+) = E^{host}(A^0) + E^{total}(A^0 \rightarrow A^+) + q E_{Fermi} \quad (1.4)$$

Where  $E^{host}(A^0)$  = the total energy of the host crystal containing one uncharged impurity;  $E^{total}(A^0 \rightarrow A^+)$  = the total energy of the host crystal containing an impurity of charge  $q$ ;  $qE_{Fermi}$  = the energy associated with the charge which resides in the Fermi reservoir.

An equivalent equation can be written for the formation energy required to introduce a charged acceptor impurity,  $A^-$ , to a host lattice:

$$\Delta E(A^-) = E^{host}(A^0) + E^{total}(A^0 \rightarrow A^-) - q E_{Fermi} \quad (1.5)$$

### 1.2.3.c Compensation

The introduction of a charged impurity into the host material may induce the formation of an oppositely charged native defect, known as *compensation*<sup>9,10</sup>. Compensation is an attempt to return the system to its lowest energy state—the original  $E_{Fermi}$ , by reversing the dopant's effects on the band structure. By reversing the effects of the dopant, the Fermi level is shifted back to its original position.

For example, when an acceptor defect is introduced into an  $n$ -type material, a defect level is formed below  $E_{Fermi}$  and near the valence band edge. The host lattice can come into equilibrium by dropping an electron from a filled state (a donor state within the gap or perhaps the conduction band) into the newly created acceptor state level, filling the acceptor state. Thus, the acceptor state is trapped and unable to participate in modifying the conductivity type of the host material.

From the previous subsection, if a host lattice is doped with donor impurities ( $A^+$ ),  $E_{Fermi}$  will increase (move closer to the conduction band minimum). As  $E_{Fermi}$

increases, the formation energy of native acceptors in the host lattice,  $\Delta E(A^-)$ , will decrease due to the minus sign in front of  $qE_{\text{Fermi}}$  term (Eqn. 1.4). At some point,  $\Delta E(A^+)$  could be low enough to spontaneously generate defects that would negate the effects of intentional doping.<sup>11</sup>

As we will see in Section 1.3, doping limits in wide band gap semiconductors are believed to originate from interplays between intentional defect introduction and the formation of compensating states.

#### ***1.2.4 Defect Energy Levels***

Independent of whether the defect is intrinsic or extrinsic, the periodicity of the host lattice is disrupted. This disruption manifests itself as a perturbation of the host's band structure—defect energy levels appear. Defect energy levels are classified as *deep* levels if they are 0.1 eV or more away from the valence band (acceptor defect level) or conduction band (donor defect level). Deep levels have an insignificant ionization of carriers at room temperature. Defect energy levels are classified as *shallow* levels if they are less than 0.1 eV or more away from the valence or conduction band. Shallow levels have a measurable number of thermally excited carriers at room temperature.

### **1.3 Doping Asymmetry of the Wide Band Gap Semiconductors**

Almost twenty years ago, it was observed that several wide band gap semiconductors were readily doped (either intrinsically or extrinsically) as one conductivity type, but not as readily doped as the other conductivity type<sup>12</sup>. For

example, MgTe and MgSe can be *p*-type doped, but *n*-type doping is challenging. Similarly, CdS and ZnS can be doped to form good *n*-type conductors, but *p*-type doping is challenging<sup>13</sup>.

Other semiconductors, such as Si and Ge, can be readily *n*- or *p*-type doped, that is to say that they can be *symmetrically doped*. The wide band gap semiconductors were deemed *asymmetrically doped*. The observed doping asymmetry was initially believed to arise from sample growth and preparation conditions—dopant quality, dopant solubility and other conditions that were not fundamentally tied to the electronic structure of the material.

By 1998, the term “doping asymmetry” underwent a change in nomenclature, taking on a connotation of grim proportions—the failure to dope rule<sup>14,15</sup>. The failure to dope rule, which will be discussed in detail in Chapter 2, used phenomenological arguments to come to the conclusion that if a certain wide band gap semiconductor could be readily *p*- (*n*-) type doped any efforts to dope that material *n*- (*p*-) type would fail.

The failure to dope rule originates from our discussion in Subsection 1.2.3.b and c—the formation energy required in order to introduce a charged impurity into the host lattice may become low enough to generate a compensating defect. The failure to dope rule states that some wide band gap semiconductors may thwart their own doping processes in this way. This is because during the introduction of the intended dopant, the formation energy of a compensating defect may be driven to such a low value that a large concentration of these compensating defects is spontaneously generated. These

spontaneously generated compensating defects are capable of negating the effect of the intended dopant.

For example, if a donor is introduced into a semiconductor that is readily rendered  $n$ -type, such as CdS or ZnO, as the donor dopant concentration increases, the formation energy for the compensating acceptor in the host lattice decreases. Eventually, the host lattice will reach a point when the efforts to intentionally dope are at risk of compensation due to the lowered formation energy of the defect state that is capable of compensation. In this situation,  $E_{\text{Fermi}}$  is pinned ( $E_{\text{Fermi}}^{\text{pin}}$ ).  $E_{\text{Fermi}}^{\text{pin}}$  represents the limit for  $E_{\text{Fermi}}$  in order for an intentionally doped system to remain uncompensated.

There are two  $E_{\text{Fermi}}^{\text{pin}}$  values:  $E_{\text{Fermi}}^{(\text{pin},n)}$  and  $E_{\text{Fermi}}^{(\text{pin},p)}$ .  $E_{\text{Fermi}}^{(\text{pin},n)}$  is defined relative to the conduction band minimum and sets a limit on the  $n$ -type doping behavior of a semiconductor.  $E_{\text{Fermi}}^{(\text{pin},p)}$  is defined relative to the valence band maximum and sets a limit on the  $p$ -type doping behavior. The position of  $E_{\text{Fermi}}^{\text{pin}}$  is influenced heavily by the position of the conduction band minimum ( $E_{\text{Fermi}}^{(\text{pin},n)}$ ) or the valence band maximum ( $E_{\text{Fermi}}^{(\text{pin},p)}$ ). The valence band maximum and conduction band minimum for a range of semiconductors and insulators have been calculated from first-principles<sup>16</sup>.

In the failure to dope rule, limits to  $E_{\text{Fermi},\text{Experimental}}^{(\text{pin},n/p)}$  are set based on reported experimental results. This approach relates  $E_{\text{Fermi},\text{Experimental}}^{(\text{pin},n/p)}$  to the measured carrier concentration of a wide band gap semiconductor,  $N^{n/p}$ , via simple Fermi-Dirac statistics<sup>17</sup>:

$$N^{n/p}[T, E_{Fermi, Experimental}^{(pin, n/p)}] = \frac{1}{2\pi^2} [2m_{n/p}^*]^{3/2} \int_0^\infty \frac{E^{1/2}}{[\exp(\beta(E - E_{Fermi, Experimental}^{(pin, n/p)})) + 1]} dE \quad (1.6)$$

Where  $m_p^*$  = hole effective mass and  $\beta = 1/k_B T$ . The position of  $E_{Fermi, Experimental}^{(pin, n/p)}$  is determined by inverting the above equation and using experimental values of  $m_p^*$  and  $N^{n/p}$

When comparing the band diagrams for various semiconductors and including pinned  $E_{Fermi}$ , it is easier to plot and compare if the  $E_{Fermi}^{(pin, n/p)}$  levels are set to constant values and the conduction band minimum and valence band maximum are scaled accordingly. This is depicted in Figure 3, where  $E_{Fermi, Experimental}^{(pin, n/p)}$  are represented by solid lines and  $E_{Fermi}^{(pin, n/p)}$  calculations from first principles are drawn as dashed lines. Some materials, such as ZnO, had only “negligible”  $E_{Fermi, Experimental}^{(pin, n/p)}$  values and thus, in those cases, there is no solid line printed in the figure.

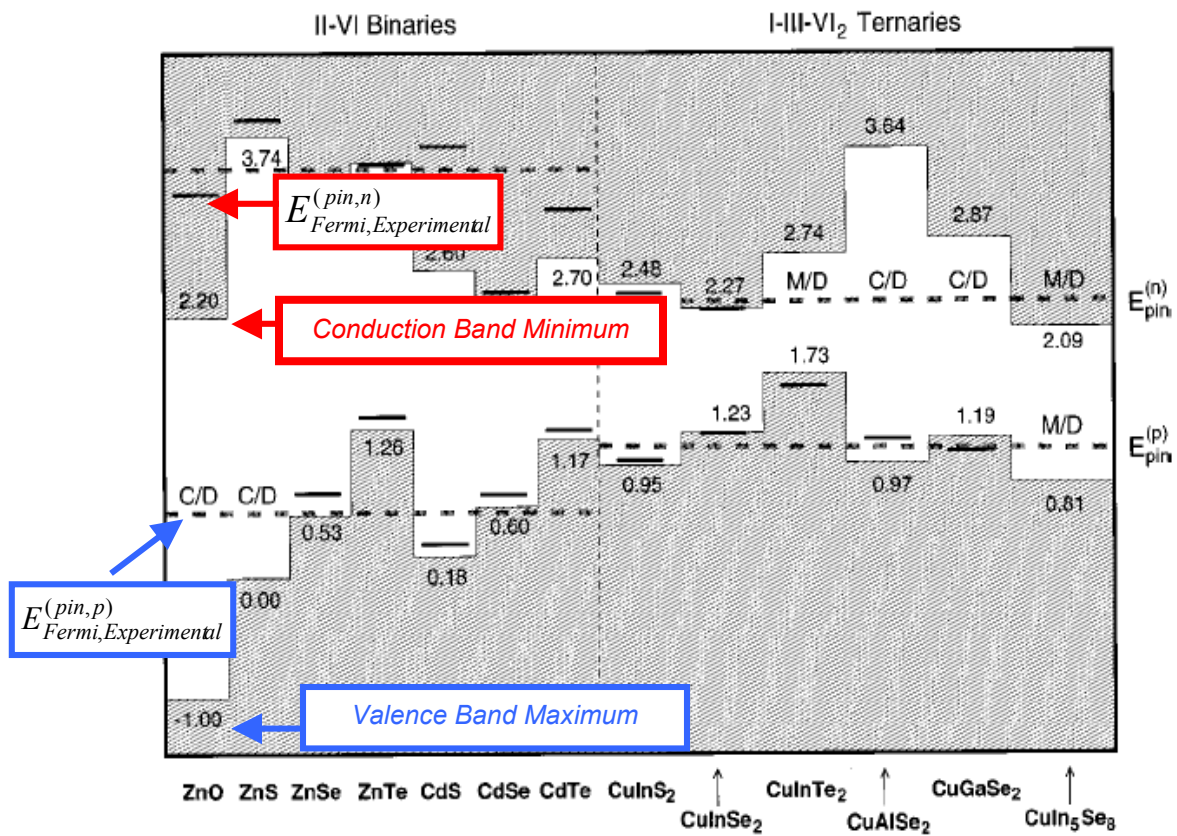


Figure 3 Band diagram for II-VI and I-II-VI<sub>2</sub> compounds<sup>18</sup>. Values for the valence band maximum and conduction band minimum energies are indicated by the lower and upper numbers in a given column, respectively. Dashed lines indicate  $E_{Fermi,Experimental}^{(pin,n)}$  (upper dashed line) and  $E_{Fermi,Experimental}^{(pin,p)}$  (lower dashed line) calculated from theoretical first principles. Short solid lines indicate  $E_{Fermi,Theoretical}^{(pin,n/p)}$ . “C/D” indicates that the position of the pinned level is consistent with data.

## Chapter 2: Doping ZnO

As Figure 3 illustrated, ZnO is one of the many wide band gap semiconductors that is believed to exhibit a doping asymmetry.  $E_{Fermi}^{(pin,n)}$  is inside the conduction band--  $n$ -type conducting ZnO is readily achievable via either native or extrinsic defects.  $E_{Fermi}^{(pin,p)}$  for ZnO is predicted to be 1.00 eV above the valence band, which if the failure to dope rule is correct, would imply that p-type doping ZnO will not be simple to achieve with either intrinsic or extrinsic defects.

We introduce the following shorthand for the discussion of defect states in ZnO (Kroger-Vink notation<sup>19</sup>):  $Zn_i \equiv$  Zn interstitial;  $O_i \equiv$  O interstitial;  $V_{Zn} \equiv$  Zn vacancy and  $V_O \equiv$  oxygen vacancy.

### 2.1 n-type Doping ZnO

#### *2.1.1 Intrinsic n-type doping*

$n$ -type ZnO is easily formed by native defects. The evidence for this can be found by simply picking up any film or crystal that has not been subjected to any other doping process—any “undoped” (extrinsically) ZnO film or crystal will likely exhibit  $n$ -type conductivity. The formation of intrinsic defects stabilizes ZnO as an  $n$ -type conductor<sup>20</sup>. This is a consequence of low formation energies of native  $n$ -type defects-- Zn interstitials ( $Zn_i$ ) and oxygen vacancies ( $V_O$ )<sup>21,22,23</sup>. Calculations have predicted that

$\Delta E(\text{Zn}_i) = 0.7 \text{ eV}$  and  $\Delta E(\text{V}_o) = 0.05 \text{ eV}$ , between 1/3 to 1/10 the formation energies for native acceptor defects.

Although it is commonly accepted that ZnO is *n*-type due to zinc interstitials or oxygen vacancies, it is not clear if specific thermodynamic conditions drive only one of these defects or if both of them are responsible in equal concentrations for *n*-type conductivity in ZnO<sup>24,25,26</sup>.

### **2.1.2 Extrinsic *n*-type doping**

Native defects have a limited capacity to controllably modify the properties of *n*-type ZnO. In order to controllably modify the electrical conductivity of *n*-type ZnO, extrinsic defects are introduced.

*n*-type enhancers have typically been found among Group I or Group III elements. Group III elements such as aluminum,<sup>27,28,29</sup> gallium,<sup>30</sup> and indium<sup>31</sup> are often selected to enhance *n*-type doping capabilities. Films have comparable mobilities to that of undoped ZnO (~20 –60 cm<sup>2</sup>/(V-s)), carrier concentrations of  $10^{20} - 10^{21} \text{ cm}^{-3}$  and resistivities as low as  $10^{-4} \Omega\text{-cm}$ .

## **2.2 p-type Doping ZnO**

The ease by which ZnO is doped *n*-type contrasts to the historical difficulties associated with *p*-type ZnO. Efforts to *p*-type dope ZnO by driving native defects or by the introduction of single or multi-element extrinsic dopants have been ongoing for the

past two decades. In this chapter, we discuss the challenges associated with *p*-type doping ZnO and review efforts to intrinsically and extrinsically *p*-type dope ZnO.

### **2.2.1 The Challenges Associated with *p*-type Doping ZnO**

In Section 1.3, we briefly introduced two concepts associated with the challenge of doping wide band gap semiconductors:

- a. Doping asymmetry/failure to dope rule
- b. Process- and dopant-associated conditions

We now discuss these two concepts as they apply to *p*-type doping ZnO.

#### **2.2.1.a ZnO and the Failure-to-Dope Rule**

The formation energy of a defect that can kill off efforts to *p*-type dope a wide band gap semiconductor (Subsection 1.2.3.b) can be simplified to:  $\Delta E^p \sim q E_{Fermi}^{(pin,p)}$ .

For *p*-type ZnO, the authors of the seminal failure-to-dope rule article determined that  $q E_{Fermi}^{(pin,p)}$  was 1.00 eV above the valence band maximum (Fig. 4). This is far enough away from the Fermi level to indicate that any effort to *p*-type dope ZnO would likely be met with compensating defects. That is,  $E_{Fermi}^{(pin,p)}$  is far away from the valence band maximum and so, the formation energy of the compensating donor defect,  $\Delta E(A^+)$ , will be low. The result—difficulty in *p*-type doping ZnO due to the low formation energies of compensating defects. Local Density Approximation calculations determined that the formation of donor defects were indeed low relative to the

formation energies of acceptor defects- at least  $1/3^{\text{rd}}$ , if not  $1/10^{\text{th}}$  the value of the formation energy of acceptor defects<sup>32</sup>.

$q E_{Fermi}^{(pin,p)}$  was determined to be 1.00 eV above the valence band by assuming that the hole concentration of  $p$ -type ZnO was “negligible.” Since the Fermi-Dirac equation used to determine the carrier concentration has only two free parameters: the carrier concentration and the effective mass, assuming that the carrier concentration is “negligible” will naturally paint a dismal picture for the ability to  $p$ -type dope ZnO.

In this dissertation, we update the failure-to-dope rule. We describe the approach that we took to develop a process for  $p$ -type doping ZnO single crystals with hole concentrations that could hardly be called “negligible.” (Chapters 5 and 6). In Chapter 7, we use our experimental results in order to update the failure-to-dope rule. We show that the position of  $E_{Fermi}^{(pin,p)}$  is not 1.00 eV from the valence band maximum, painting a slightly more optimistic picture for the future of  $p$ -type doping of ZnO.

### **2.2.1.b Process- and Dopant-Associated Conditions**

While the failure-to-dope rule sets constraints based on the pinning of  $E_{Fermi}$ , there are other terms in the formation energy equations introduced in Section 1.2.3.b—chemical potentials—influenced by the exchange of host and dopant particles in and out of their respective reservoirs. These chemical potentials can be modified by process-associated conditions (growth/processing temperature) and dopant-associated conditions (relative electronegativity of the dopant & host atoms, solubility, competitive phases).

*Growth/Processing Temperature:* Influences the resulting concentration of dopant incorporated into the lattice by modifying  $E_{formation}$ . For example, heating in order to reduce the chemical potential is believed to facilitate the dissolution of dopants into a host material<sup>33</sup>.

*Electronegativity Differences:* Linus Pauling spearheaded efforts in chemistry to understand the nature of chemical bonds in compounds<sup>34</sup>. He developed a series of rules that simplify the mechanism of lattice formation down to its bare electrostatics. Of significance to this discussion is Pauling Rule #5—Environmental Homogeneity—chemically similar atoms will prefer similar environments. In other words, it is energetically favorable to insert a dopant material of comparable electronegativity to that of the host elements. In addition to the electronegativity difference between the dopant atom and the appropriate host atom, one must also consider the ability of the dopant atom to coordinate with the structure's existing coordination.

*Limited solubility of dopant atoms:* The ability of one material to dissolve into another is a variation on Pauling Rule #5: materials that are chemically similar or have similar sizes tend to dissolve into one another with ease compared to materials with significant chemical or physical differences. The solubility is the maximum equilibrium concentration that can be attained in the semiconducting host material. The equilibrium concentration,  $c$ , is<sup>35</sup>:

$$c = N_{sites} e^{-E_{formation} / k_B T} \quad (2.1)$$

Where  $E_{formation}$  = formation energy;  $N_{sites}$  = the number of sites that the impurity can be incorporated onto;  $T$  = temperature and  $k_B$  = Boltzmann's constant.

### 2.2.2 *Intrinsic p-type doping*

In principle, ZnO could be *p*-type doped via intrinsic defects, namely: oxygen interstitials ( $O_i$ ) and Zn vacancies ( $V_{Zn}$ ). However possible it may seem, there is one significant factor that would steer any sensible experimentalist away from attempting to *p*-type dope ZnO solely by intrinsic defects: formation energy. Firstly, as stated in Section 2.2.1.a, the formation energies for acceptor defects ( $O_i$  and  $V_{Zn}$ ) are large in comparison to those for donor defects. So, under equilibrium conditions, the donors would win out. Even if it were possible to somehow minimize or even drive out the *n*-type native defects, the formation energies for acceptor defects may still be high and thus, only a small concentration of *p*-type defects would form<sup>36</sup>.

*Competitive Phase Formation:* The introduction of a large concentration of dopant material does not guarantee that the host material will allow the dopant to substitute onto the appropriate lattice site. Some fraction of the dopant material may interact with host atoms to form other phases whose properties may compete with the properties of the desired doped phase<sup>37,38</sup>.

*Unintentional Introduction of Compensating Donor Defects:* Atmospheric hydrogen, which is ubiquitous in even the most pristine deposition ambients, may be an

unintentional culprit of compensation<sup>39,40</sup>. If this is the case, hydrogen would pose a significant challenge to the doping process, as it can act as an amphoteric dopant, countering whichever conductivity is prevailing at the time of exposure. O-H bonds have a *negative* energy of formation for all H<sup>+</sup> charge states (-1.84 to -1.59 eV) and locations along the wurtzite structure, H<sub>2</sub>, H<sup>-</sup> and H<sup>0</sup> all have positive energies of formation (0.84, 3.92, and 1.07 eV, respectively)<sup>41</sup>. Thus, the H<sup>+</sup> form of hydrogen would be the predominant charge state at an oxygen-terminated ZnO surface (as is the case with our samples). The H<sup>+</sup> state would serve as a donor to ZnO in the form of Zn(OH)<sub>2</sub>.

*Limited impurity ionization at room temperature caused by deep level impurities:* The impurity ionization energy determines the fraction of carriers doped into the host material that will be thermally activated and free to participate in conduction. As discussed earlier, it is determined by the intrinsic properties of the host material (effective mass, dielectric constant). At room temperature, the ionization energy must be  $k_B T = 26$  meV or less in order to have a significant number of carriers to participate in conduction. If the dopant's impurity level is deep, meaning that it is positioned at greater than 26 meV (relative to the valence band edge for *p*-type semiconductors) the probability of thermal excitation of carriers will be low. For example, an impurity level of 200 meV would have only roughly 1% of its carriers free to participate in conduction.

### 2.2.3 *Extrinsic p-type doping*

Although there have been some reports in the literature of *p*-type doping ZnO with intrinsic dopants those reports are not commonplace<sup>42,43,44,45</sup>. More commonly, *p*-type doping ZnO has been pursued by introducing extrinsic defects. Extrinsic dopants for *p*-type doping ZnO include single element substitutions as well as multi-element (co-doping) efforts. To *p*-type dope ZnO using a single element substitution, an excess of holes is required. So the impurities introduced should have a valence state of +1 or -3. Either one of these states would produce an excess of holes.

#### 2.2.3.a **Single Element Substitutions: +1 and -3 Valence States**

Group I elements such as K, Li and Na all have a +1 valence state and thus, have the potential to substitute on the Zn site. Experimentally, they have not been proven to be effective *p*-type dopants. For example, K enters ZnO as an interstitial, rather than substituting onto the Zn site<sup>46</sup>. It is predicted that Li or Na as dopants for *p*-typing ZnO may form inclusions (Na<sub>2</sub>O or Li<sub>2</sub>O) and/or hydrogen complexes (Na-H or Li-H), both of which have lower energies of formation in comparison to the energy of formation for dopant insertion into the ZnO lattice<sup>47,48</sup>. Other +1 valence state elements outside of Group I, such as Ag, which was predicted to have a near-deep acceptor state<sup>49</sup>, were attempted during the investigatory stages of this thesis and were, due to sample preparation issues, not reported in the body of this work.

Group V elements such as N, P, As and Sb have a -3 oxidation state that would satisfy the constraint for *p*-doping ZnO by substituting at the oxygen site. We will

discuss Group V dopants in more detail in subsection 5. Theoretical calculations of the energy levels of N, P, As and Sb as substitutional impurities for ZnO are shown in Figure 4.

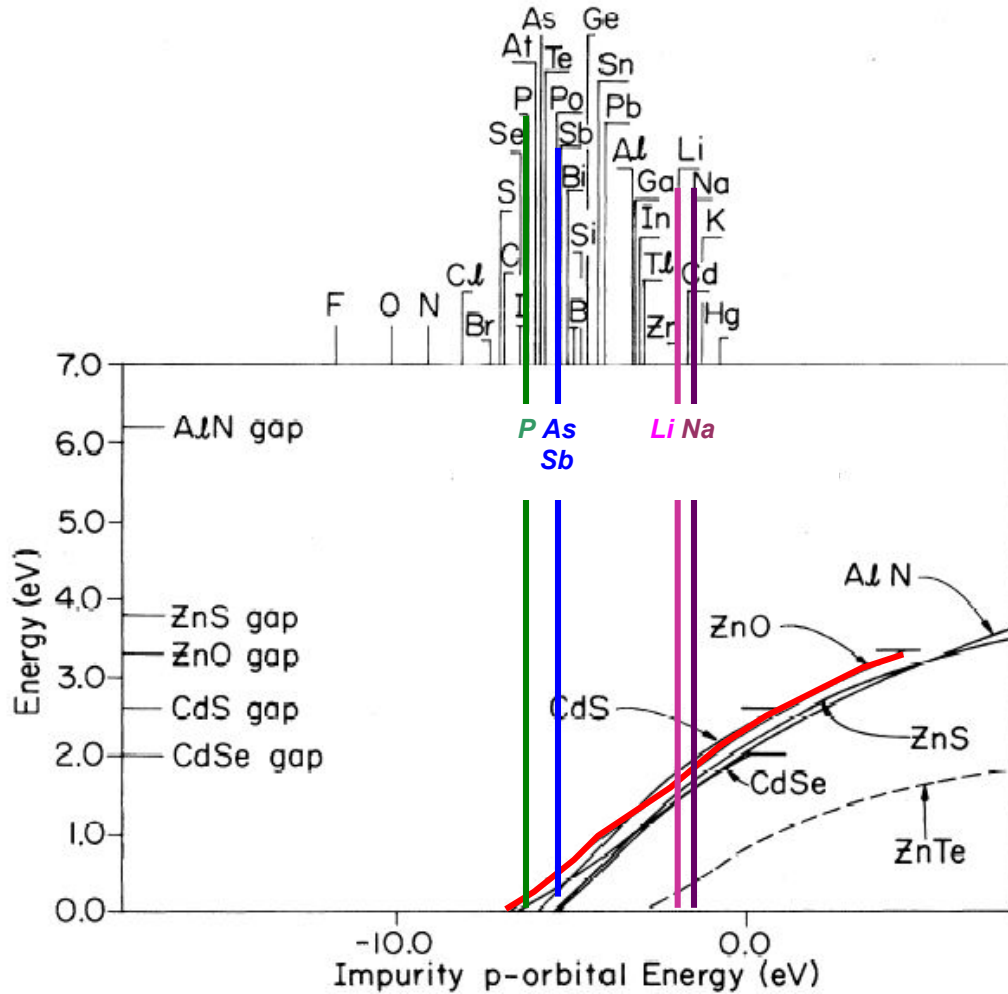


Figure 4 Predicted energy levels of anion impurities introduced into different wurtzite lattices vs. energy of a given element's p-orbital<sup>70</sup>

**2.2.3.b Co-Doping**

Co-doping using metal donors (for example, Al or Ga) along with an acceptor state element (for example, N, Cu or Li) has been attempted for p-type doping ZnO with

limited reproducibility<sup>50,51</sup>. With co-doping, an acceptor-donor complex is formed. The thought here is that the acceptor is introduced with overall lower activation energy, enhancing the ability of the acceptor to be incorporated into the ZnO lattice<sup>52</sup>.

While co-doping improves the chance of incorporation by substitution, the issue of localized hole states still remains unsolved by this method. For this reason, co-doping approaches were not considered for this investigation.

#### **2.2.4 Group V Elements as Extrinsic *p*-type Dopants for ZnO**

Group V elements such as N, P, As, and Sb have been suggested as possible dopants for *p*-type doping ZnO<sup>53</sup>. Looking at their electron configurations, Group V dopants have the capacity to be *amphoteric*, that is, they have the capacity to act as a donor or acceptor. The outer orbitals for Group V elements are  $s^2p^3$ —so the *p* orbital can be filled completely (-3), it may be emptied (+3) or both *s* and *p* orbitals can be emptied (+5). The possible oxidation states for these elements are listed in Table 2. At the time of this writing, there was no published work on the amphoteric nature of Group V dopants in ZnO.

*Electronegativity Differences:* Of the possible Group V dopants, nitrogen and phosphorus are under vigorous investigation. Invoking Pauling Rule 5, we briefly examine the electronegativity differences of Group V elements bonded to either Zn or O in Table 3. The percent ionic character in the bond was calculated using an empirical

relationship proposed by Linus Pauling that is related to the electronegativity difference between the two constituent elements, A and B:

$$\text{percent ionic character} = 100 (1 - e^{0.25(\chi_A - \chi_B)}) \quad (2.2)$$

Where  $\chi_A$  and  $\chi_B$  are the electronegativities of element A and element B, respectively.

The key question is whether or not evidence exists for less disruption of the overall electrostatic background (hence, reduced Madelung potential and energy of lattice formation). While none of the Group V dopants has a close ionic character when bonded to Zn, the Zn-N bond is more ionic than the Zn-P bond, indicating that N may make a better *p*-type dopant than phosphorus since there is a smaller % difference between the nature of the Zn-N bond and the Zn-O bond compared to the Zn-P bond.

*Ionic Radii:* A comparison of ionic radii for Zn, O and candidate *p*-type doping elements along with coordination and oxidation numbers can be found in Table 4. Recall, that Zn and O are four-fold coordinated in the ZnO lattice. A general rule of thumb is that two elements can substitute for one another if their ionic radii are within 15% of one another.

**Table 2: Oxidation states of Group V elements**

<i>Element</i>	<i>Electron Configuration</i>	<i>Oxidation States</i>	
		<i>Positive</i>	<i>Negative</i>
N	[He] 2s <sup>2</sup> 2p <sup>3</sup>	+5, +4, +3, +2, +1	-1, -2, -3
P	[Ne] 3s <sup>2</sup> 3p <sup>3</sup>	+5, +3	-3
As	[Ar] 4s <sup>2</sup> 4p <sup>3</sup>	+5, +3	-3
Sb	[Kr] 5s <sup>2</sup> 5p <sup>3</sup>	+5, +3	-3
Bi	[Xe] 6s <sup>2</sup> 6p <sup>3</sup>	+5, +3	X

**Table 3: Electronegativity difference and % ionic character of Zn, O and dopant elements**

<i>Bond</i>	<i>Bond Length [nm]</i>	<i>Pauling Electronegativity Difference</i>	<i>% Ionic Character of Bond</i>
Zn-O	0.197	1.8	56
Zn-N	0.201	1.4	39
Zn-P	0.248	0.5	6
Zn-As	0.256	0.4	4
Zn-Sb	N/A	0.3	2
Zn-Bi	N/A	0.3	2

**Table 4: Comparison of ionic radii for Zn, O and candidate dopant material<sup>54</sup>**

<i>Element</i>	<i>Oxidation Number</i>	<i>Coordination</i>	<i>Ionic Radius[Å]</i>
Zn	+2	4	0.60
		5	0.68
		6	0.74
		8	0.90
O	-2	2	1.35
		3	1.36
		4	1.38
		5	1.40
		6	1.42
N	-3	4	1.46
	+3	6	0.16
	+5	6	0.13
P	-3	4	2.12
	+3	6	0.44
	+5	4	0.17
		5	0.29
		6	0.38
As	-3		2.22
	+3	6	0.58
	+5	4	0.34
		6	0.46
Sb	-3		2.45
	+3	4	0.76
		5	0.80
		6	0.76
	+5	6	0.6
Bi	+3	5	0.96
		6	1.03
		8	1.17

*Competitive Phase Formation:* ZnO, like many wide band gap materials, has a low dielectric constant, indicative of contracted outer orbitals. Consequently, a larger concentration of dopant material may be necessary in order to increase the outer orbitals to a size that will permit overlap and consequently, conduction, to take place<sup>55</sup>. Increasing the concentration of the dopant does not necessarily facilitate dopant incorporation, since competing compounds may form. For example, in the case of using phosphorus to attempt to *p*-type ZnO, Zn<sub>3</sub>P<sub>2</sub> may form, placing constraints on the concentration of P available for ZnO doping. Zn<sub>3</sub>P<sub>2</sub> is also a *p*-type material with a band gap of ~1.3 eV.<sup>56</sup> Table 5 is a comprehensive table of potential competitive phases and their conductivity types for group II elements combined with group V elements.

**Table 5: List of potential competitive phases & their conductivity types for Group II elements combined with Group V dopants<sup>57</sup>**

<b>Group II</b> → <b>Group V</b> ↓	<b>3d<sup>10</sup> 4s<sup>2</sup></b> <b>Zn</b>	<b>4d<sup>10</sup> 5s<sup>2</sup></b> <b>Cd</b>	<b>4s<sup>2</sup> 4p</b> <b>Ga</b>	<b>5s<sup>2</sup> 5p</b> <b>In</b>
<b>2p<sup>3</sup></b> <b>N</b>	X	X	<i>n</i> -type GaN	X
<b>3p<sup>3</sup></b> <b>P</b>	<i>p</i> -type Zn <sub>3</sub> P <sub>2</sub>	X	<i>n</i> -type GaP	<i>n</i> -type InP
<b>4p<sup>3</sup></b> <b>As</b>	<i>p</i> -type Zn <sub>3</sub> As <sub>2</sub> ZnAs <sub>2</sub>	<i>n</i> -type Cd <sub>3</sub> As <sub>2</sub> CdAs <sub>2</sub>	<i>n</i> -type GaAs	<i>n</i> -type InAs
<b>5p<sup>3</sup></b> <b>Sb</b>	<i>p</i> -type ZnSb	<i>p</i> -type CdSb	<i>p</i> -type GaSb	<i>p</i> -type InSb
<b>6p<sup>3</sup></b> <b>Bi</b>	X	X	X	X

*Note: "X" in Table 5 denotes that there is no known compound produced from this combination of elements.*

*Limited Solubility of Dopant Atoms:* Almost 20 years before the rush to produce *p*-type ZnO, a group of theorists speculated that while N is likely to be a shallow dopant in ZnO, it is not very soluble<sup>70</sup>. They speculated that ion implantation may be the only way to dope ZnO. Nitrogen, as N<sub>2</sub>, NO<sup>-</sup>, or NO<sub>2</sub>, has been attempted as a *p*-type dopant in ZnO<sup>58,59</sup>. It has been found that activation of N to a free radical form<sup>60</sup> or growth via temperature modulated epitaxy<sup>61</sup> does give rise to *p*-type conductivity; however, samples undergo conversion to their original *n*-type state after a few days in an ambient environment<sup>62</sup>.

We suspect that if there are minimal oxygen vacancies and Zn interstitials at the time of the initial film growth (*n*-type conductivity contributions), since no additional Zn is added post-deposition, oxygen vacancy formation by out-diffusion of nitrogen, which may have occupied oxygen's position in the lattice is the likely culprit for reversion to the original *n*-type state. The reported timescales of a few hours to a few days is suggestive of a rapid diffusion mechanism, such as diffusion of nitrogen along grain boundaries in the film out to the surface<sup>63</sup>.

While nitrogen may seem like an obvious and potentially successful candidate for *p*-type doping of ZnO, it may be solubility or outdiffusion limited. Thus, it is important to explore possible alternatives. Phosphorus is one of those alternatives. Given its electron configuration, for *p*-type doping ZnO, phosphorus should substitute on the anion-site with *p* orbital character. The impurity level for phosphorus in ZnO is not agreed upon; some predictions show that it is at the shallow-deep borderline<sup>64</sup>, while others predict that it is deep.<sup>65, 66</sup>

*Compensation by formation of undesirable dopant complexes:* It is possible that the dopant compensates itself by forming a defect complex. This is possible if the energy of formation of the defect complex is less than the energy of formation of the dopant impurity. Such complexes have been observed in efforts to *n*-type dope GaAs with Si<sup>67</sup>. The formation of compensating dopant complexes is predicted for II-VI semiconductors when doped with N, P, As or Sb, but not specifically for ZnO<sup>68</sup>.

The most common dopant complexes are extrinsic dopant defects known as DX (a complex composed of a donor, D, and another element in the complex, X) centers, in *n*-type systems and AX centers in *p*-type systems. We'll focus on AX centers here.

AX centers are a special class of deep-level defect capable of compensating for the introduction of acceptors. In the case of ZnO, an AX center could form by breaking two Zn-O bonds and forming one O-O bond<sup>69</sup>. In the process, two electrons are produced, thus adding to the overall balance of donors. This defect is known to be destabilized by large lattice distortions in other wide-band gap semiconductors, such as ZnSe and ZnMgSe<sup>70</sup>.

Arsenic has been reported to be a *p*-type dopant<sup>71,72</sup>. Reported carrier concentrations range from  $10^{15}$  to  $10^{18}$  cm<sup>-3</sup> and hole mobilities range from 6-35 cm<sup>2</sup>/(V-s) with no correlation between the carrier concentration and hole mobility. The defect level of As is predicted to be quite deep ( $E_{\text{acceptor}} = 930$  meV)<sup>73</sup>. There is some speculation that strain relief and Coulomb interactions between As and Zn may produce a new class of defects that have shallow levels—wherein As occupies a Zn antisite and two Zn vacancies are induced. The Zn vacancies would then represent a native kind of

*p*-type dopant. In this case, As would not act as the direct source of the *p*-type doping, but rather as a facilitator for the formation of a native *p*-type defects.

A similar complex formation that facilitates *p*-type doping has been predicted for antimony (Sb) doped into ZnO. Experimental efforts to dope Sb into ZnO have been equally limited. Results show *p*-type behavior with low mobilities ( $1.5 \text{ cm}^2/\text{V}\cdot\text{s}$ ) and high carrier concentrations ( $5 \times 10^{20} \text{ cm}^{-3}$ )<sup>74</sup>.

### Chapter 3: Conceptual Map of this Effort

The focus of this dissertation is best summarized as a “*bottom up*” approach, as indicated in the diagram below:

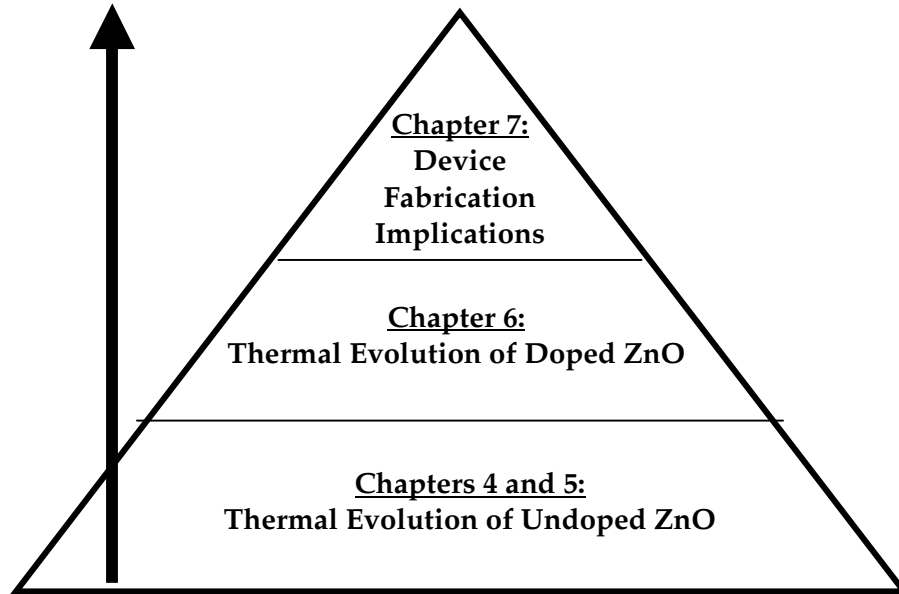


Figure 5 Conceptual map of this investigation

Efforts to *p*-type dope ZnO currently do not rest on a solid foundation of understanding the conditions that promote or suppress defect formation. In this dissertation, we approach the problem of producing *p*-type ZnO by understanding defect formation in the undoped material. In Chapters 4 and 5 of this dissertation, we begin to build this solid foundation by examining the thermal evolution of defects in undoped ZnO.

Using the foundation set in Chapters 4 and 5, in Chapter 6, we discuss our investigation of the thermal evolution of *doped* ZnO thin films and single crystals.

Finally, in Chapter 7 we discuss our findings in the context of unipolar (Schottky) and bipolar device fabrication.

# Chapter 4: Thermal Evolution of Bulk Properties of Undoped ZnO Thin Films

## 4.1 Introduction and Approach

In order to understand the conditions that minimize the presence of defects that may lead to self-compensation, competitive phase formation, or introduction of undesirable impurities that have the capacity to compete with *p*-type doping of ZnO, we began by optimizing the conditions under which undoped ZnO thin films may be grown. We investigated the effects of deposition temperature ( $T_{\text{dep}}$ ) and  $p(\text{O}_2)$  on structural and optical properties of undoped ZnO thin films.

While investigating process conditions that would minimize the concentration of undesirable, compensating defects, the following guideline was kept in mind: films should be prepared in such a way that, according to theory, would maximize the formation energy of the undesirable defect states.

RF sputter deposition was selected as the thin film deposition technique since well-oriented, on-stoichiometry thin-film ZnO can be deposited at low temperatures<sup>75</sup>. Other techniques, such as Pulsed Laser Deposition (PLD), can produce high-quality films, but they do so only at high temperatures (for ZnO,  $T_{\text{dep}} \sim 600\text{-}800^\circ\text{C}$ )<sup>76</sup>.

Low deposition temperatures were necessary for the following reasons: (1) to permit comparisons with existing efforts to *p*-type dope ZnO and (2) to minimize dopant loss associated with the low sublimation point of  $\text{P}_2\text{O}_5$ , the *p*-type dopant of

interest in this work, ( $T_{\text{sublimation}} \sim 350^{\circ}\text{C}$ ); and (3) to minimize donor carrier concentration.

There is a well-known interplay between thin film epitaxy (governed by the deposition temperature,  $T_{\text{dep}}$ ), the microstructure of the thin film (crystallinity) and strain and the optical and electronic properties of semiconducting thin films. We examine the interplay for undoped films in this chapter.

#### ***4.1.1 The Role of Low Deposition Temperatures***

Generally speaking, epitaxial growth via sputtering occurs above a critical temperature<sup>77</sup>,  $T_{\text{dep, critical}}$ , typically quoted at 25% of  $T_{\text{melt}}$ . For ZnO,  $T_{\text{dep, crit}} \sim 500^{\circ}\text{C}$ . So, we would expect a progressive narrowing of the (0002) FWHM as  $T_{\text{dep}}$  approached and then exceeded  $T_{\text{dep,crit}}$  as the growth approached epitaxy, limited only by film-substrate mismatch. Well-oriented films deposited at low temperatures demonstrate a clear advantage of using sputtering over other deposition techniques.

The range of deposition temperatures used was:  $T_{\text{dep}}$  = unassisted heating,  $125^{\circ}\text{C}$ ,  $250^{\circ}\text{C}$ , and  $550^{\circ}\text{C}$ . These were selected in order to allow for comparisons to previous studies of  $p$ -type doping in ZnO using phosphorus. The thought here is that if defects exist in the undoped host material for this range of deposition temperatures, then the likelihood of producing uncompensated  $p$ -type doped thin films would be small.

#### ***4.1.2 The Role of $p(\text{O}_2)$***

Using RF sputtering prepares the oxygen reservoir with unbound oxygen atoms, since  $\text{O}_2$  is dissociated in the atmosphere via the sputter plasma, setting  $\mu_{\text{Oxygen}} < 0$ .

Dissociation of oxygen in the sputter plasma raises the formation energy of the donor state ( $V_o$ ) and lowers the overall chemical potential of the acceptor state ( $O_i$ )<sup>78</sup>.

Zunger addressed this for wide band gap semiconductors by looking at general conditions for the minimization/maximization of the formation energy and enthalpy:

- Cation-rich deposition conditions produce: anion vacancies & cation interstitials
- Anion-rich deposition conditions produce: cation vacancies & anion interstitials.

This is depicted in Figure 6.

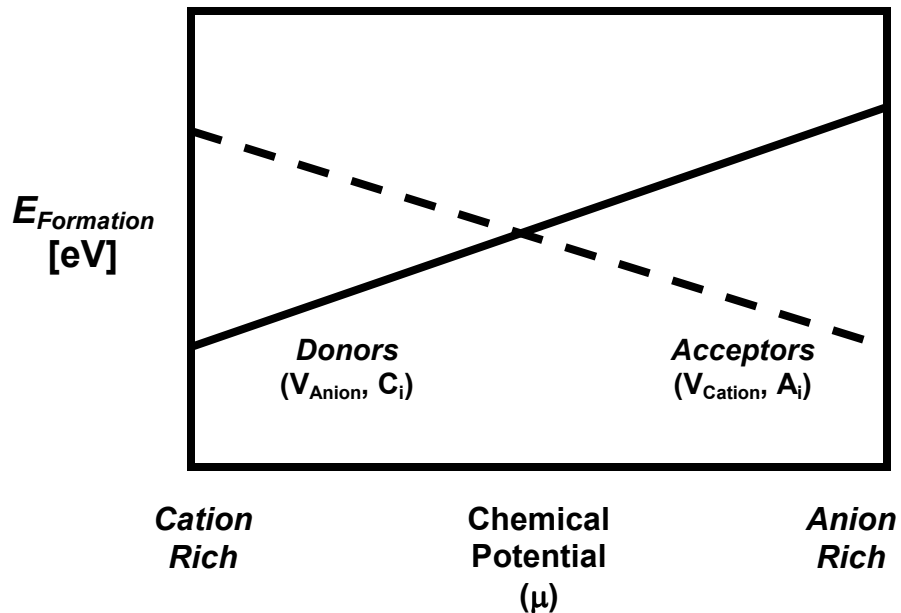


Figure 6 Schematic depiction of the formation energies of general intrinsic donors (anion vacancy  $V_A$ , cation interstitial  $C_i$ ) and intrinsic acceptors (cation vacancy  $V_C$  and anion interstitial  $A_i$ ) vs. the chemical potential. Adapted from Reference <sup>79</sup>

Thus, from the above discussion, an oxygen-rich deposition atmosphere is “anion-rich.” Under such conditions, the formation energies for  $V_{\text{Zn}}$  and  $O_i$  will be low. These two defect states do not compensate efforts to  $p$ -type dope ZnO and thus, an

anion-rich atmosphere will support efforts to *p*-type dope ZnO. An argon-rich atmosphere is “cation-rich”. Under these conditions, the formation energies of defects capable of compensating *p*-type conductivity are lowest. Thus, an cation-rich atmosphere will counter efforts to *p*-type dope ZnO.

Indirect experimental support for this theory has existed for quite some time, but has not been put in the context of formation energies and appropriate thin film deposition conditions. For example, undoped ZnO films grown in an argon-rich atmosphere have been observed to have high donor concentrations ( $10^{18} \text{ cm}^{-3}$ ), with the donor concentration associated with Zn interstitials (cation-rich).<sup>80</sup> Also, nucleation sites in films grown in an argon-rich atmosphere have been observed to be less dense in comparison to films grown in oxygen-rich ambients<sup>81</sup> with crystalline quality (as measured via the (0002) XRD FWHM) degrading as  $p(\text{O}_2)$  decreased<sup>82</sup>. A lower density of nucleation sites may result in more structural defects, since growth may not proceed as smoothly in the regions where there is a lower density of nucleation sites.

To test the effects of  $p(\text{O}_2)$  on the formation of defects in ZnO, a total pressure of 16 mTorr was selected. Pre-existing work on Al-doped (donor doped) ZnO films showed a rise in resistivity accompanied by a drop in donor mobility for films grown at this pressure<sup>83</sup>. This suggested that donor concentration is minimized at this sputter pressure and may support an effort to *p*-type dope ZnO.

Two deposition atmospheres were used: an argon-rich condition— $p(\text{Ar}) = 15$  mTorr and  $p(\text{O}_2) = 1$  mTorr and an oxygen-rich condition-- $p(\text{Ar})= 6$  mTorr and  $p(\text{O}_2) = 10$  mTorr. The condition of  $p(\text{Ar}) = 6$  mTorr was selected because it is the minimum Ar

pressure required in order to achieve a stable plasma power for a 100W setting of the RF source<sup>84</sup>.

#### 4.1.3 The Role of Strain

In addition to  $T_{\text{dep}}$  and  $p(\text{O}_2)$ , lattice strain plays a role in influencing the generation of defects in a semiconductor.

The addition or removal of atoms from a lattice structure modifies relative atomic positions, producing changes in the lattice parameters--*lattice strain*. Strain is calculated relative to the lattice parameter value from an accepted reference such as the JCPDS<sup>85</sup>.

Uniaxial strain along the  $c$ -axis direction,  $\epsilon_{zz}$ , is written as:

$$\epsilon_{zz} = \frac{c - c_0}{c_0} \times 100 \% \quad (4.1)$$

Where,  $\epsilon_{zz}$  is strain along the  $c$ -axis,  $c$  is the measured  $c$ -axis lattice parameter,  $c_0$  = the bulk  $c$ -axis lattice parameter value from the JCPDS powder diffraction database,  $c = 5.2066 \text{ \AA}$ <sup>86</sup>, which is a close approximation to the relaxed (unstrained) lattice parameter of a thin film.

As depicted in Fig. 7, there are two types of strain: *compressive* and *tensile*. In the above equation:

- $\epsilon_{zz} > 0$  is defined as tensile strain
- $\epsilon_{zz} < 0$  is defined as compressive strain.

Strain influences the chemical potential for defect formation. The chemical potential of a stressed solid in some atomic volume,  $\Omega$ , can be written as:

$$\mu = \pm \sigma\Omega \quad (4.2)$$

Where  $\sigma$ , stress, is related to the lattice strain via:

$$\sigma = Y\varepsilon \quad (4.3)$$

Where  $Y$  = Young's Modulus, which is equal to 111 GPa for ZnO<sup>87</sup>.

Strain can arise from four main sources:

- *substrate-film lattice mismatches*
- *thermal expansion mismatches between the film and substrate*
- *formation of native defects associated with the growth process*
- *incorporation of dopant atoms with a size that is different from that of the host atom.*

In this section, we focus on the first two sources of strain. We will focus on the third source in Chapter 6 when we discuss phosphorus doping in the ZnO lattice.

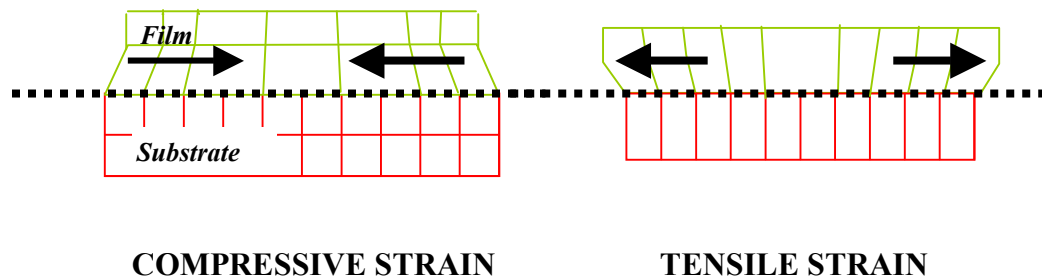


Figure 7 Left—Schematic of epitaxial film layer under tensile strain. Right—Schematic of epitaxial film layer under compressive strain. Interface between film and substrate is denoted by a dotted line.

*Strain associated with Substrate Mismatch:* When a film is under compressive strain, it is a consequence of a smaller lattice parameter of the desired film compared to the underlying substrate. In order for the film to grow with some degree of epitaxy, it must compress its lattice structure, in attempts to match the lattice parameter of the underlying substrate. Films with tensile strain result from the stretching of the lattice in attempts to accommodate the underlying lattice parameter of the substrate, which is larger. The lattice mismatch that is relevant to this work—the mismatch between  $(0001)\text{Al}_2\text{O}_3$  and  $(000\bar{1})\text{ZnO}$  is approximately 18 %.

In the limit of very thin films,  $<1000 \text{ \AA}$ , such a mismatch would produce noticeable variations in bulk properties of the film, such as the band gap,  $E_{\text{gap}}$ , since the strain associated with heteroepitaxial growth is confined to the narrow region of film-substrate interface. The film thicknesses used in this work are  $\sim 2500 - 5000 \text{ \AA}$ , making substrate-induced strain less of a concern for this thesis, since as the film thickness increases, a strain relaxation growth mode emerges.

*Strain Associated With Intrinsic Defect Formation:* Native defects in ZnO, oxygen vacancies or zinc interstitials, modify the lattice parameters of ZnO and thus, are sources of strain.

The presence of tensile strain in the ZnO host lattice (presumably from Zn interstitials) is predicted to lower the energy required to form oxygen vacancies<sup>88</sup>. *Thus, the presence of tensile strain may be used an indicator of poor conditions for p-type dopant incorporation.*

## **4.2 Growth Parameter Influence on Structural Properties**

ZnO thin films were grown via on-axis RF magnetron sputter deposition on double-sided polished (0001) Al<sub>2</sub>O<sub>3</sub> substrates at a total deposition pressure of 16 mTorr. The evolution of strain and lattice structure were examined as a function of two main sputtering variables:  $p(\text{O}_2)$  and deposition temperature ( $T_{\text{dep}}$ ). A detailed description of RF sputtering and the deposition system that was constructed for this dissertation can be found in Appendix 1.

Crystallinity and the c-axis lattice constant were among the properties we sought to optimize. The crystallinity is a direct measure of the degree of disorder in a lattice from a wide variety of sources.

In addition, we examined the temperature dependence of tensile strain in the ZnO host lattice. Tensile strain, primarily originating from Zn interstitials, is predicted to lower the energy required to form oxygen vacancies and the presence of strain lowers the formation energy for compensating defects around extrinsically introduced defects<sup>89</sup>.

### ***4.2.1 Crystallinity***

Although  $T_{\text{dep}}$  was low in comparison to conventional epitaxial growth temperatures for undoped ZnO, undoped films grown under both Ar-rich and O-rich atmospheres were (000 $\bar{1}$ )-oriented, with no additional orientations present. A FWHM  $\sim 2^\circ$  indicated that the films were mildly textured for films grown at  $T_{\text{dep}}$  = unassisted heating. This is consistent with reports in the literature<sup>90</sup>.

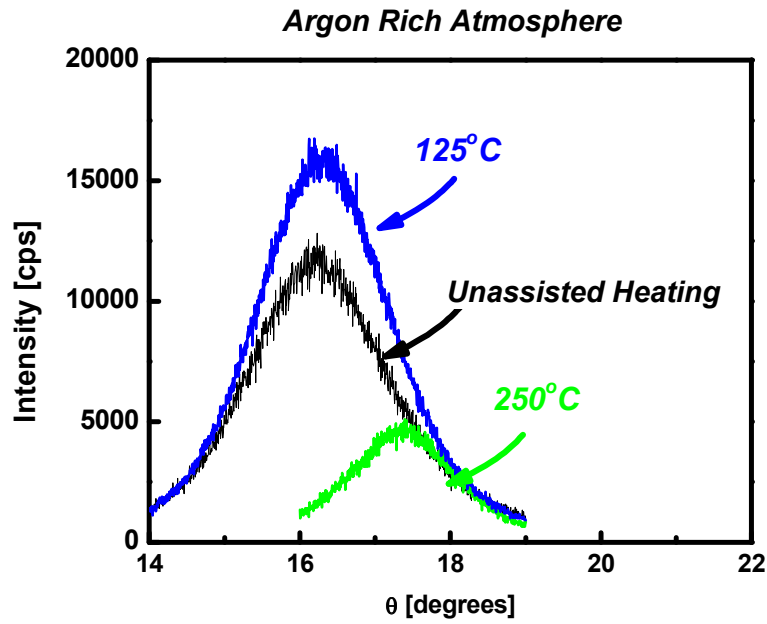
We observed minimal temperature-dependent changes in the x-ray FWHM of the (0002) peak for argon-rich films (raw data - Fig. 8(a), FWHM vs.  $T_{\text{dep}}$  - Fig. 9(a)). There are only minimal changes up to and including  $T_{\text{dep}} = 550^{\circ}\text{C}$ , which is greater than  $T_{\text{dep, crit}}$ . There is a minimum in the FWHM at  $T_{\text{dep}} = 250^{\circ}\text{C}$ , which is not consistent with the predicted  $T_{\text{dep, crit}}$  behavior.

Films grown under oxygen-rich conditions (raw data - Fig. 8(b), FWHM vs.  $T_{\text{dep}}$  - Fig. 9(a)) showed a monotonically decreasing FWHM with increasing  $T_{\text{dep}}$ , consistent with the predicted  $T_{\text{dep, crit}}$  behavior. This indicates that undoped films grown under argon-rich conditions are not optimally-oriented at the  $T_{\text{dep}}$  that have been used in previous studies of  $\text{P}_2\text{O}_5$  doping of ZnO for the purposes of  $p$ -type doping.

Given this data, it is not terribly surprising to see inconsistent reports of  $p$ -type conductivity. Simply stated, if the starting material is not well oriented, the host lattice is riddled with defects that will compete with efforts to  $p$ -type dope ZnO.

From the FWHM data, we observe that the oxygen rich condition,  $p(\text{O}_2) = 10$  mTorr, supports well-oriented ZnO film growth, particularly for  $T_{\text{dep}} \geq 250^{\circ}\text{C}$ . The argon-rich condition,  $p(\text{O}_2) = 1$  mTorr, supports the growth of quasi-epitaxial samples that have optimal crystallinity at  $T_{\text{dep}} = 250^{\circ}\text{C}$ .

(a)



(b)

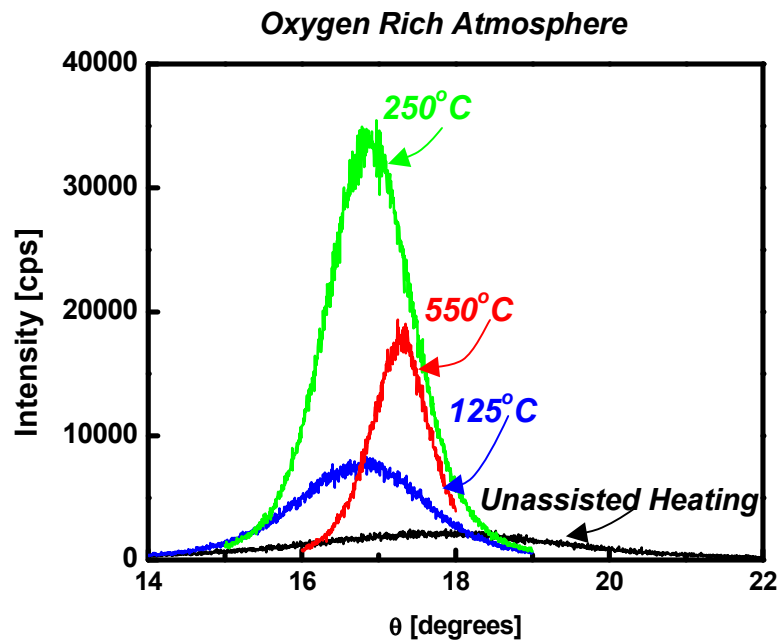


Figure 8 Rocking curve data for (0002) orientation of undoped ZnO thin films grown on (000-1)  $\text{Al}_2\text{O}_3$  for Ar-rich and O-rich ambients at various  $T_{\text{dep}}$

#### 4.2.2 *c*-axis length

Although there is little change in the FWHM with increasing  $T_{\text{dep}}$  for undoped films deposited in the argon-rich atmosphere, the *c*-axis length changes considerably for films grown in this atmosphere (Fig. 9(b)). For unheated samples, the *c*-axis lattice parameter is close to the value for bulk ZnO, as quoted in the JCPDS (5.2066Å). As  $T_{\text{dep}}$  increases to 250°C, the *c*-axis increases. This corresponds to the temperature at which the FWHM is at a minimum, indicating that lattice expansion is the likely source of improvements in crystallinity. For example, for a  $T_{\text{dep}} = 550^\circ\text{C}$ , the *c*-axis length approaches that of the bulk value.

Samples grown in an oxygen-rich atmosphere at  $T_{\text{dep}} \leq 250^\circ\text{C}$  have a *c*-axis length that is considerably longer than the bulk value. Across  $T_{\text{dep}}$ , the *c*-axis length shows similar  $T_{\text{dep}}$  dependence as the FWHM—there is a monotonic decrease in the *c*-axis length with increasing  $T_{\text{dep}}$ . As  $T_{\text{dep}}$  increases to 550°C, the *c*-axis length approaches the bulk ZnO value and is smaller than that of the argon-rich films grown at 550°C.

Undoped films grown at the same  $T_{\text{dep}}$  as in films grown in previous studies of phosphorus doping of ZnO, in an Ar-rich atmosphere show a lower degree of crystallinity vs. films grown at the same temperature range in an oxygen-rich atmosphere. That lower degree of crystallinity is likely the source of defects that may serve to counter efforts to *p*-type dope ZnO. This is observed to a lesser extent for the films deposited in oxygen. Thus, if structural defects are the culprits for compensation, efforts to *p*-type dope ZnO are best supported in an oxygen-rich atmosphere.

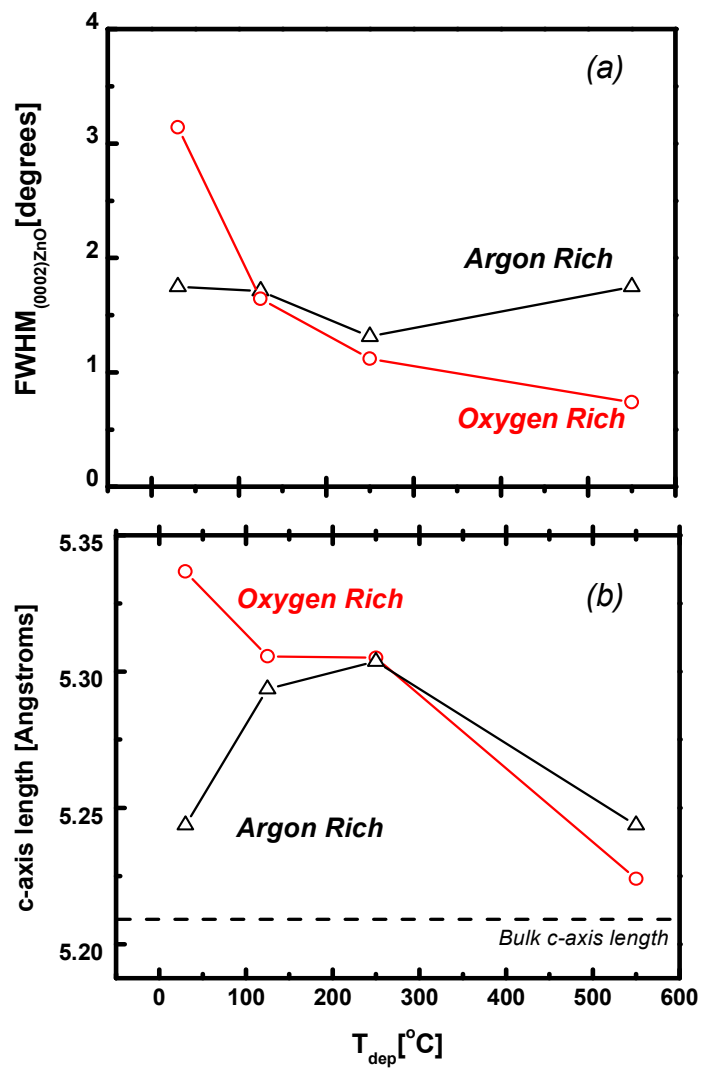


Figure 9 (a)(0002) FWHM vs.  $T_{dep}$  and (b) c-axis length vs.  $T_{dep}$  for undoped ZnO thin films grown in either Ar-rich or O-rich ambients at 16 mTorr.

### 4.2.3 *c*-axis Strain

Strain along the *c*-axis ( $\epsilon_{zz}$ ) of the undoped films was examined as a function of deposition temperature,  $T_{\text{dep}}$ , for both argon-rich and oxygen-rich deposition conditions (Fig. 10). Uniaxial strain measurements along the *c*-axis were determined via four-circle x-ray diffraction measurements of the lattice parameters of the film. The (0002) reflection of ZnO was selected, as it had the largest intensity.

Overall, films grown in the oxygen-rich atmosphere show tensile strain that progressively decreases with increasing  $T_{\text{dep}}$ . Films grown in the argon-rich atmosphere show a nonmonotonic dependence upon  $T_{\text{dep}}$  that is overall tensile in nature, with a region of compressive strain between  $T_{\text{dep}} = 250 - 400^\circ\text{C}$ .

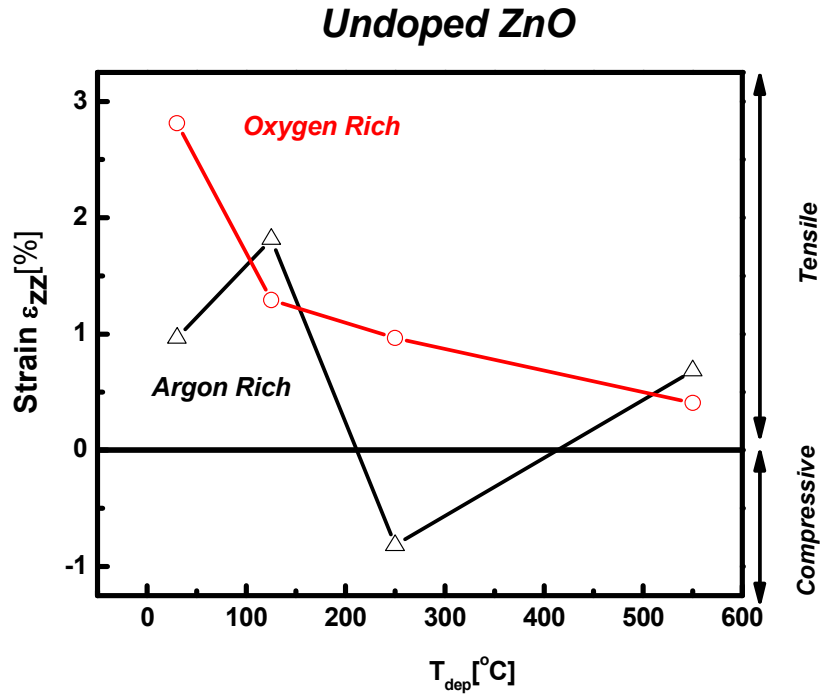


Figure 10  $\epsilon_{zz}$  vs.  $T_{\text{dep}}$  for undoped ZnO thin films grown in either oxygen rich or argon rich atmospheres.

So, while the oxygen-rich grown films show a better overall FWHM along the  $c$ -direction, indicating fewer defects in a film in comparison to the argon-rich deposited films, the films grown in oxygen show a large amount of tensile strain, which is, as we stated in Section 4.2, predicted to lower the energy of formation for compensatory defects in ZnO. This further places limitations on the available parameter space to minimize defects that are capable of compensatory behavior.

## **4.4 Relationship between Strain and Optical Properties**

### ***4.4.1 Background***

Strain perturbs energy levels in the band structure of a material, which manifests itself as changes in the optical and electrical properties of ZnO.

In its simplest form, electrons at the defect center are like electrons in a conventional one-dimensional quantum mechanical infinite square well. Strain deforms the dimensions of that box. A simple one-dimensional infinite square well potential has an energy  $E = h^2 n^2 / 8ma^2$ , where  $a$  is the width of the box, in this case, the  $c$ -axis lattice spacing. If strain changes the width of the box from  $a$  to  $\Delta a$ , then we can write:  $\Delta E/E = \Delta a/a \equiv \varepsilon_{zz}$ . Thus we can correlate the shift in the main peak position with the lattice strain<sup>91</sup>, using  $E = 3.37$  eV as the unstrained ZnO main peak position using this basic, non-perturbative quantum mechanical model.

As an additional level of complexity, a series of band-structure models for strain-perturbed wurtzite structures, such as ZnO, has been developed<sup>92,93</sup>. We focus on one model and its conclusions regarding the effects of strain on the energy gap.

Pikus initially presented the effect of any elastic deformation on the optical properties of a wurtzite lattice in 1962<sup>94</sup>. The effect of strain on the band gap of a wurtzite-type lattice was written as a linear approximation relative to the conduction band energy (which is fixed). The approximation looks only at the change in the position of the valence band position due to strain:

$$E_{gap, strained} = - (E_{valence, 0} + \Delta E_{valence}) \quad (4.4)$$

Where,  $E_{gap, strained}$  = band gap value for a strained material,  $E_{valence, 0}$  = the position of the valence band without lattice strain present and  $\Delta E_{valence}$  = the change in the position of the valence band in the presence of strain.

- If  $\Delta E_{valence} < 0$ , the result is a decrease in the measured band gap value
- If  $\Delta E_{valence} > 0$ , the result is an increase in the measured band gap value

The valence band maximum was written by Pikus in terms of strain in the wurtzite lattice as:

$$\Delta E_{valence} = \Delta_1 + \frac{\Delta_2}{2} \times \left\{ 1 + \frac{\Delta_{CF} - (\Delta_{SO}/3)}{[(\Delta_{CF} - (\Delta_{SO}/3))^2 + 8(\Delta_{SO}/3)^2]} \right\} \quad (4.5)$$

Where,  $\Delta_1 = C_1 \epsilon_{zz} + C_2(\epsilon_{xx} + \epsilon_{yy})$  and  $\Delta_2 = C_3 \epsilon_{zz} + C_4(\epsilon_{xx} + \epsilon_{yy})$ ; the  $C_i$  are the deformation potentials for ZnO (with  $C_1 = -2.66$ ,  $C_2 = +2.82$ ,  $C_3 = -1.34$ ,  $C_4 = 1.0\text{eV}$ )<sup>95</sup> and  $\epsilon_{xx}$ ,  $\epsilon_{yy}$ , and  $\epsilon_{zz}$  are strains along the respective crystallographic directions;  $\Delta_{CF}$  = crystal field splitting energy = 42 meV and  $\Delta_{SO}$  = spin orbit splitting energy = -5 meV<sup>96</sup>.

Substituting in the above constant values, Eqn 4.5 becomes:

$$\Delta E_{valence} = 5.88(\varepsilon_{xx} + \varepsilon_{yy}) - 5.90 \varepsilon_{zz} \quad (4.6)$$

Since, for a wurtzite lattice,  $\varepsilon_{xx} = \varepsilon_{yy}$ , for c-axis films, then:

$$\Delta E_{valence} = 11.76 \varepsilon_{xx} - 5.90 \varepsilon_{zz} \quad (4.7)$$

And Eqn. 4.4. becomes:

$$E_{gap, strained} = - [E_{valence, 0} + (11.76 \varepsilon_{xx} - 5.90 \varepsilon_{zz})] \quad (4.8)$$

For *c*-axis-oriented ZnO films grown by RF sputtering, the in plane strain,  $\varepsilon_{xx}$ , does not vary much with deposition temperature or pressure, with an average  $\varepsilon_{xx} = \varepsilon_{yy} = -0.02$  or 2%<sup>97</sup>. In addition, it is related to  $\varepsilon_{zz}$  by a constant prefactor associated with the elastic constants along the *c*- and *a*- axis directions<sup>98</sup>.

Knowing this, we are able to write the strained band gap in terms of only the out of plane strain component,  $\varepsilon_{zz}$  :

$$E_{gap, strained} = - [E_{valence, 0} + (0.235 - 5.90 \varepsilon_{zz})] \quad (4.9)$$

By this linear approximation, assuming a uniform in plane strain, a 1 % compressive strain  $\varepsilon_{zz}$  results in a shift in the band gap by +0.3 eV relative to the

unstrained valence band position. A 1% tensile strain produces a shift of  $-0.1$  eV. This is depicted schematically in Figure 11.

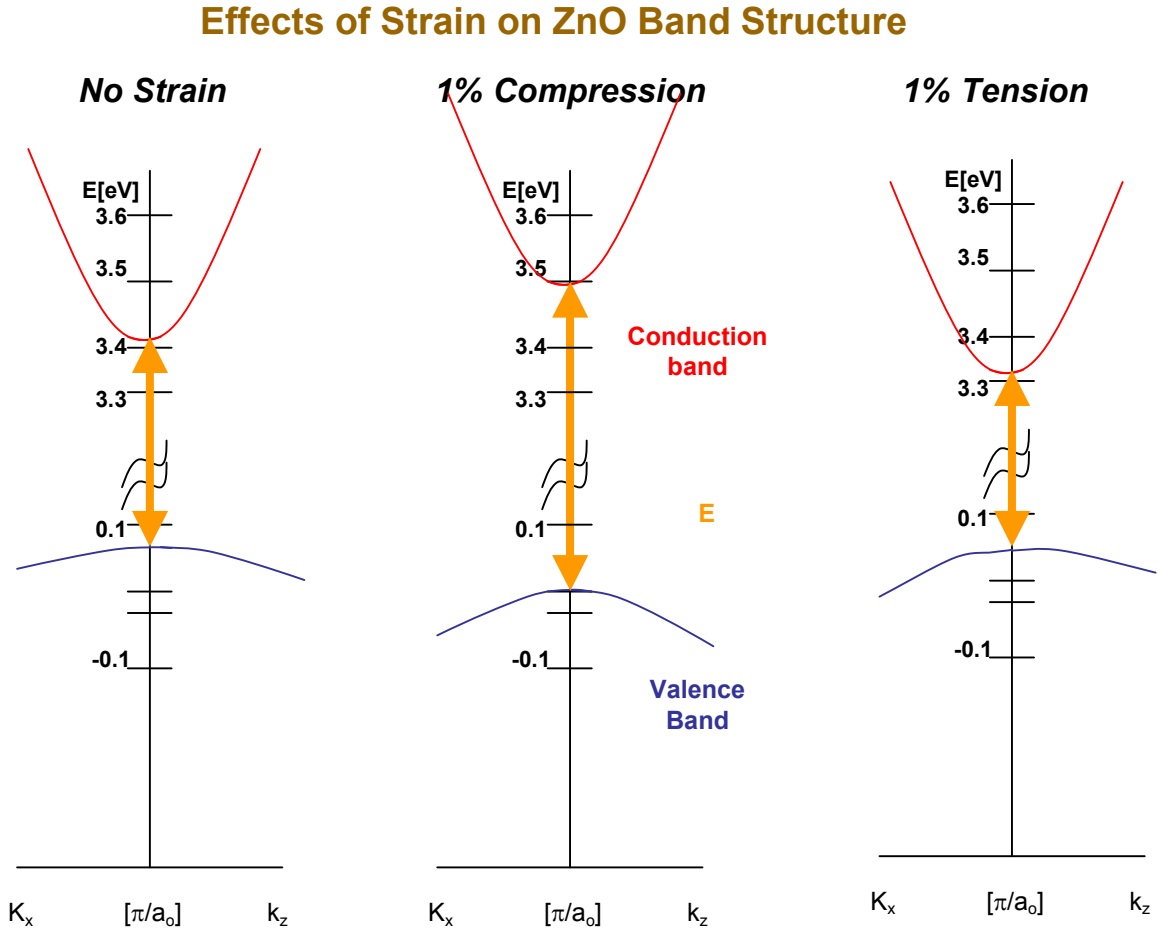


Figure 11 Schematic of band structure as perturbed by strain

This linear approximation can be used to find  $E_{valence, 0}$  and also to estimate any change in the valence band maximum position in the presence of strain. In doing so, it helps to refine limitations imposed by the failure-to-dope rule (Figure 3).

To check for this, films were analyzed via UV-visible spectrometry relative to a blank sapphire substrate, operating in transmission mode. Details of the measurement and analysis process can be found in Appendix 3.

#### 4.4.2 Results

Spectra for the argon-rich and oxygen-rich cases are shown in Fig. 12 (a) and (b), respectively.  $E_{\text{gap}}$  was extracted from the raw spectra, as discussed in the Appendix, and plotted as a function of  $T_{\text{dep}}$  (Fig. 13). For both deposition atmospheres, the band gap is smaller than what is observed for single crystal ZnO ( $E_{\text{gap}} = 3.37$  eV), indicating that both deposition atmospheres produce off-stoichiometry films. Films grown in the Ar-rich atmosphere have rather narrow  $E_{\text{gap}}$  values which reached a minimum at  $T_{\text{dep}} = 250^{\circ}\text{C}$ . The oxygen-rich films have an overall larger  $E_{\text{gap}}$ , a value that is lower, but still closer to the optimally-doped ZnO value.

Fig. 14 shows that the relationship between  $E_{\text{gap, strained}}$  and out of plane lattice strain,  $\epsilon_{zz}$ , is not linear for either deposition atmosphere. Fig. 14 also shows that the band gap value is nearly equal for films grown in the two different ambients at  $\epsilon_{zz} = 1\%$ .

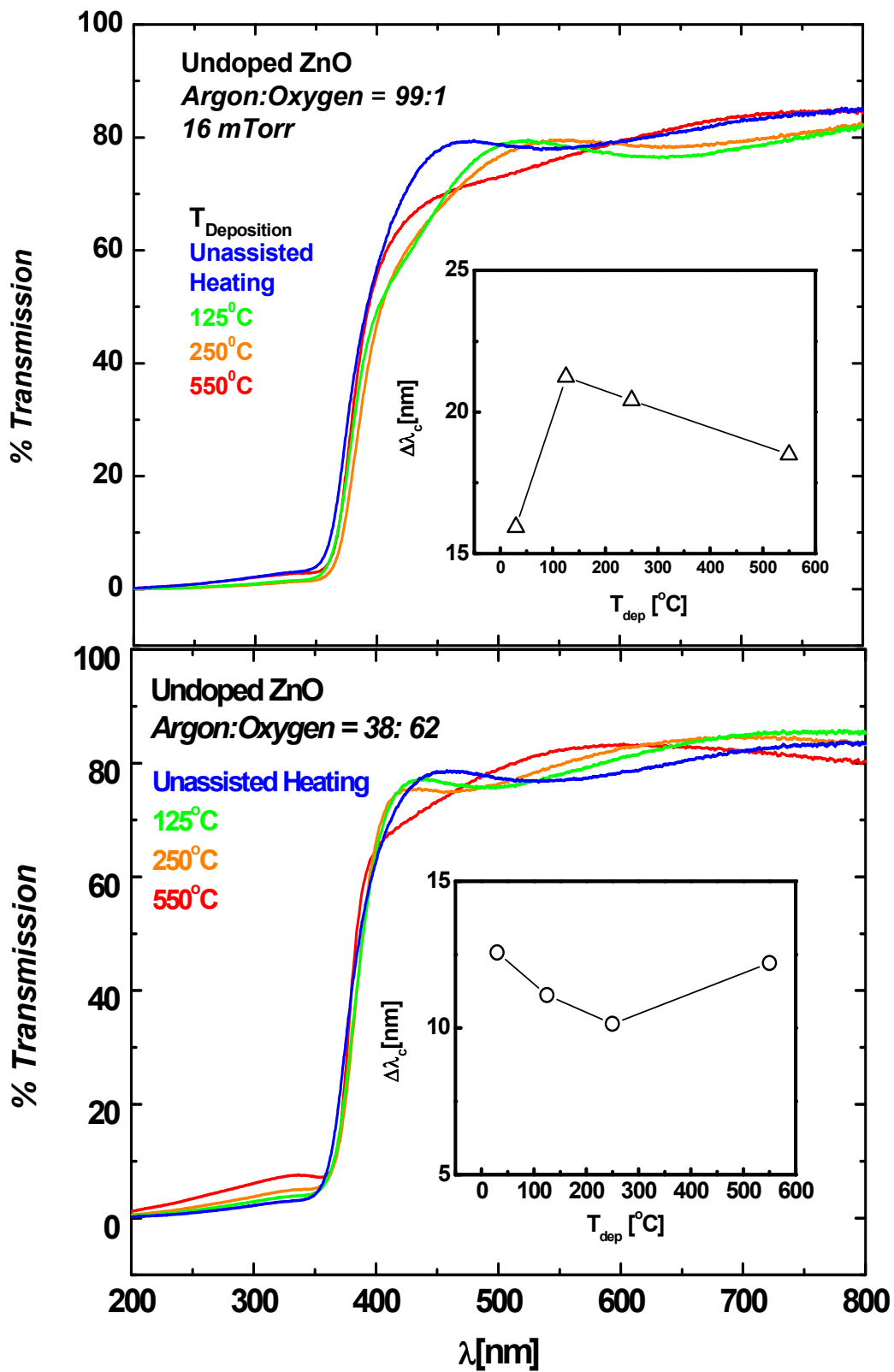


Figure 12 % Transmission vs.  $\lambda$  (excitation wavelength) for undoped ZnO grown at various  $T_{\text{dep}}$  for Ar-rich (top) or O-rich (bottom) atmospheres. Insets: Transition width  $\Delta\lambda$  vs.  $T_{\text{dep}}$ .

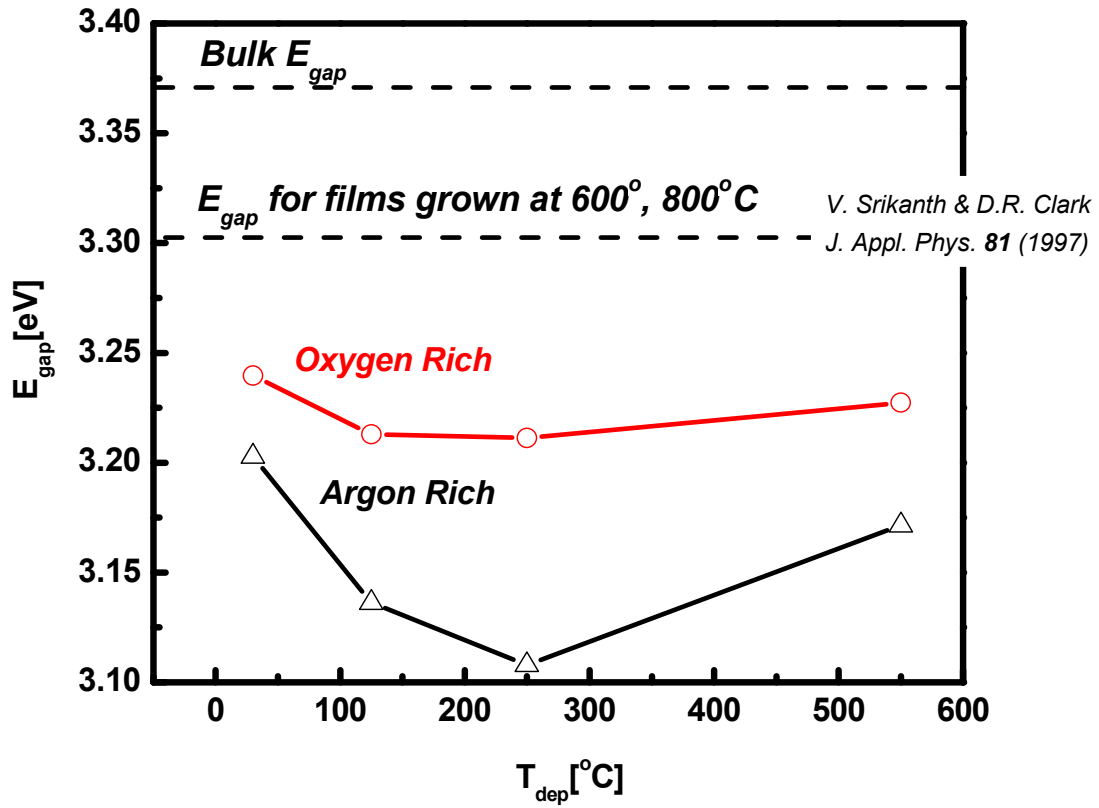


Figure 13 Band Gap ( $E_{gap}$ ) vs.  $T_{dep}$  for undoped ZnO films grown in either Ar-rich or O-rich atmospheres.

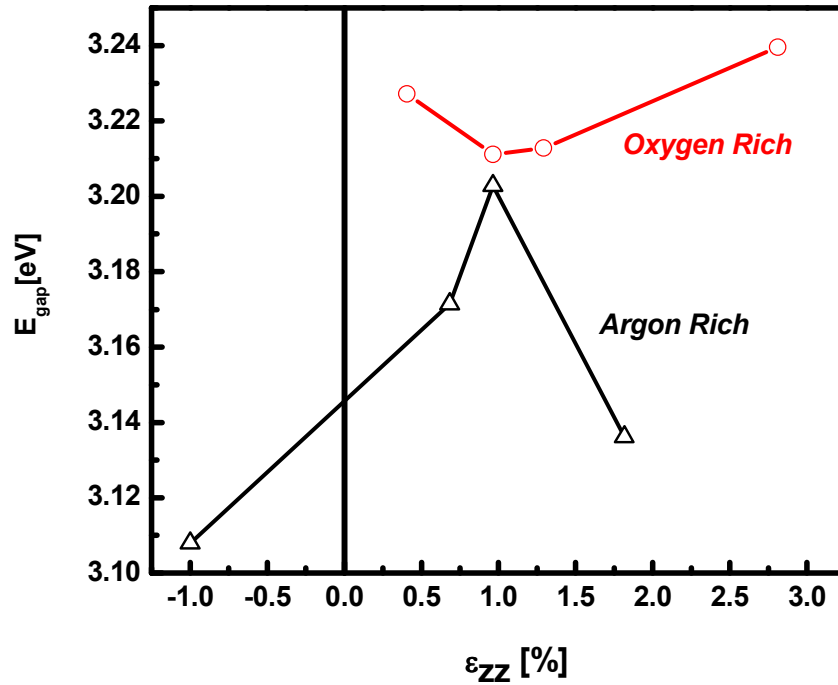


Figure 14 Band Gap ( $E_{gap}$ ) vs.  $\epsilon_{zz}$  for undoped ZnO films grown in either Ar-rich or O-rich atmospheres.

#### 4.4.3 $T_{dep}$ Influence on the Distribution of Defect States

$\Delta\lambda$ , the transition width of the UV-Vis transmission spectrum, provides information about the spread of defect states inside of the gap. We see that the width of the transmission spectrum (Fig. 12 insets for (a) and (b)) correlates with  $T_{dep}$ —as the sample becomes more oriented,  $\Delta\lambda$  decreases for the oxygen-rich case—there is a narrower distribution of states in the energy gap.

The argon-rich grown films show a minimum in the spread of defect states within the gap for films that were grown at 125°C (Fig. 12, top inset). This correlates to the maximum in uniaxial strain (Fig. 10). The oxygen-rich-grown films show a minimum in  $\Delta\lambda$  for samples deposited at  $T_{dep} = 250^\circ\text{C}$  (Fig. 12, bottom inset). This

correlates to the inflection point of the temperature-dependent strain behavior. So the degree of crystallinity influences the spread of states within the gap.  $\Delta\lambda$  is smaller for films grown in oxygen-rich atmospheres compared to those grown in Zn-rich atmospheres.

## **4.5 Conclusions**

Higher  $T_{\text{dep}}$  promotes overall better crystallinity. Crystallinity is better overall in the oxygen-rich ambient, but tensile strain is larger overall. While a better crystallinity will minimize the effects of self-compensating defects, the presence of strain may reduce the formation energy for compensating impurities. Strain in the oxygen-rich deposited films is overall less than the strain observed in those films grown in an argon-rich atmosphere.

# Chapter 5: Thermal Evolution of Surface and Bulk Properties of Undoped ZnO Single Crystals

## 5.1 Background

Understanding the thermal evolution of ZnO single crystals under non-ultrahigh vacuum (non-UHV) conditions is important when considering optimal conditions to dope *p*-type ZnO single crystals. Ion implantation<sup>99</sup> and planar doping<sup>100</sup> are commonly used in silicon, III-V, and II-VI semiconductor doping. Both of these methods contain a thermal processing step in a non-UHV atmosphere to either activate the dopant, as is the case with ion implantation, or to introduce the dopant via diffusion, as is the case for planar doping.

Planar doping of single crystal ZnO would involve diffusion of a solid dopant source into the crystal via the surface, so any significant compositional changes at the surface affects the extent of dopant diffusion into the sample.

While there have been extensive studies of the thermal evolution of the ZnO surface in the pristine environment of an ultrahigh vacuum (UHV) system<sup>101,102,103,104</sup>, prior to this work, studies of the behavior of single crystal ZnO upon thermal annealing under *non*-UHV conditions have been limited to low temperature anneals ( $T_{\text{ANNEAL}} < 400$  °C) or indirect measurements of surface effects<sup>105</sup>. These studies have been conducted in either nitrogen or air atmospheres.

A common conclusion drawn by both UHV and non-UHV studies is that the surface roughness of thermally treated ZnO changes, but the origin of the roughness has not been directly determined. Speculative origins, such as surface reordering associated

with limited out diffusion with Zn or O evaporation<sup>106</sup> --“metallization of the polar surface<sup>107</sup>”, or contaminant formation<sup>108</sup> have been raised.

In this chapter, we explore the behavior of ZnO upon thermal annealing in non-UHV conditions in a more comprehensive manner than previously reported efforts. Firstly, since there have been no direct investigations of the origin of surface roughness variations of ZnO single crystal samples annealed under non-UHV conditions<sup>109</sup>, we look at the surface and near-surface temperature evolution directly. Secondly, we expand extensively on the existing work on thermal annealing behavior of ZnO by examining thermal annealing response for  $T_{\text{ANNEAL}} \geq 400^{\circ}\text{C}$  in air other non-oxidizing ambients—argon and vacuum.

We compare both the argon-rich and oxygen-rich (in this case, air) atmospheres, as in Chapter 4. In addition, we look at the effects of vacuum annealing. Again, we invoke the argument that the formation energy for native *n*-type promoting defects is low for samples grown in atmospheres that promote Zn-richness, such as the argon-rich atmosphere used our film growth studies and we investigate the applicability of this argument to the promotion of Zn-richness during annealing.

Elucidating changes in surface composition has a two-fold impact: (1) Unipolar Schottky barrier height will be influenced by variations in surface composition and (2) Bipolar device fabrication processes may be directly influenced by the surface. Since thermal annealing in semiconductors is known to stimulate or suppress defect formation it also affects the capacity of the introduced dopant to *p*-type dope ZnO in single crystal form. This is observed in GaAs, where diffusion of dopants into the surface is affected by surface conditions, particularly surface defect states<sup>110</sup>.

## 5.2 Approach

Our approach probed the continuum of changes in single crystal ZnO, from the surface to the bulk, as depicted in Fig. 15. The surface region was sampled using Atomic Force Microscopy (AFM) and X-ray Photoelectron Spectroscopy (XPS). AFM samples the immediate surface morphology and XPS samples up to a depth of 15 nm into the material. In the near-bulk region, Rutherford Backscattering Spectrometry (RBS) was used to assess composition and crystallinity to a depth of 500 nm. In the bulk, x-ray diffraction (XRD), electrical transport, and optical measurements (photoluminescence) were used to assess structural changes, carrier changes and band structure changes, respectively. The minimum depth sampled by these techniques was  $\sim 2000$  nm ( $2 \mu\text{m}$ ). With information from these different length-scales, we were able to assess the thermal evolution in air of ZnO single crystals as a function of depth.

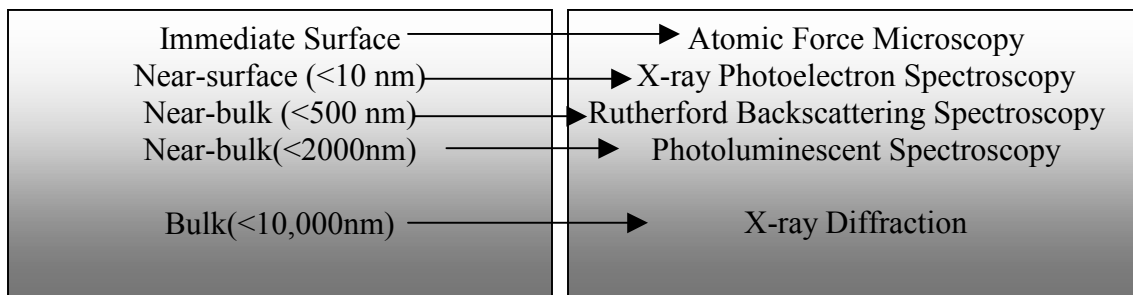


Figure 15 Schematic of the approach and techniques used in this chapter<sup>111</sup>.

Commercially available hydrothermally grown, single-side polished  $(000\bar{1})$  face ZnO single crystals (Cermet Incorporated) were isochronally annealed for 1 hour in air, argon ( $p \sim \text{atm.}$ ) or vacuum ( $p \sim 10^{-6}$  Torr) for  $T_a = 200 - 800^\circ\text{C}$ .

*Atomic Force Microscopy:* Subsequent to annealing, sample r.m.s. roughnesses were immediately measured using atomic force microscopy (AFM) in tapping mode ( $2 \times 2 \mu\text{m}^2$ ). Special care was taken to use a new AFM tip for each roughness measurement in order to avoid any error associated with tip wear. Further details may be found in Appendix 4.

*X-ray Photoelectron Spectroscopy:* X-ray Photoelectron Spectroscopy (XPS) was conducted using a Kratos AXIS 165 spectrometer with 165 nm hemispherical analyzer and 8 channeltron detection system. The system was set in hybrid lens mode with a 210W Mg anode. Adventitious carbon concentrations were determined for each sample and were used in the analysis to correct for offsets in the binding energy (average E(C1s)  $\sim$ 284 eV). No x-ray induced changes in the samples were observed. Zn 2p and O 1s data were fit using a standard least-squares fit with a multiple Gaussian peak approach (goodness of fit  $r^2$  values  $\sim$  0.990 or better, see Figure 20(b)). Further details may be found in Appendix 5.

*Rutherford Backscattering Spectroscopy:* RBS probes up to 500 nm in depth when a sample's crystallographic orientation is not aligned with respect to the incoming alpha particles (*random alignment*). When a crystallographic axis of a sample is aligned with the beam of incoming alpha particles, the particular mode of RBS in use is known as the *channeling mode*. Channeling is a near-surface measurement that is capable of probing the atomic displacement within a 20-100 nm depth from the surface (dependent upon

the ion energy).  $\chi_{\min}$ , is the minimum channeling yield, the ratio of the number of disordered ions to total ions. A minimum yield of 5% implies that greater than 95% of the total number of atoms are in the correct position. More details of RBS are discussed in Appendix 4.

## **5.3 Results**

### ***5.3.1 Surface Roughness***

We observed that the surface morphology of ZnO single crystals depends upon both the annealing temperature and the composition of the annealing atmosphere. annealed in air roughened for  $T_{\text{ANNEAL}} < 600^{\circ}\text{C}$  (Fig. 16(a)). In the unannealed state, AFM showed a moderately smooth surface, up to scratches lingering from the commercial provider's chemical-mechanical polishing process. The surface also contained pebble-like structures. The r.m.s. roughness of the unannealed surface is  $\sim 0.3$  nm. Crystal surfaces annealed at  $T_{\text{ANNEAL}} = 400^{\circ}\text{C}$  showed a striking change in morphology. Large valleys were visible in the AFM surface plot of samples annealed at this temperature (Fig. 16(b)). The overall roughness was a factor of four larger than the unannealed state. Crystals annealed at higher  $T_{\text{ANNEAL}} (> 400^{\circ}\text{C})$  had smooth surfaces, with roughnesses that are equivalent to the unannealed case. The pebble-like features that were observed on the unannealed samples are also seen for samples annealed at  $T_{\text{ANNEAL}} > 400^{\circ}\text{C}$  (Figs. 16(c), (d)). When compared to the unannealed case, the distribution of these pebbles across the crystal surface is less dense and the pebbles have larger diameters.

The immediate difference between crystals annealed in air versus in non-oxidizing ambients is apparent in the surface roughness (Fig. 17). Samples annealed in argon (Fig. 17, left column) do not show the rough, spherical features observed in vacuum- and air-annealed samples. Argon-annealed samples have a morphology that does not significantly vary with  $T_{\text{ANNEAL}}$ . Vacuum-annealed samples (Fig. 17, right column) show a dramatic morphological change when annealed at 200°C. Broad, feathery structures  $\sim 0.25 \mu\text{m}$  wide, appear. As  $T_{\text{ANNEAL}}$  increases, these structures condense into small, near-spherical structures that are  $< 0.1 \mu\text{m}$  in diameter.

While roughnesses for samples annealed in argon and vacuum are of a similar magnitude (Fig. 18), the morphologies of samples annealed under the two non-oxidizing ambients are quite different. The absolute values of the r.m.s. roughness for samples annealed in either of the non-oxidizing ambients are less overall than those of the air-annealed samples for the full range of  $T_{\text{ANNEAL}}$  (Fig. 19). This indicates that oxidation plays a role in determining the behavior of ZnO surfaces annealed in air at  $T_{\text{ANNEAL}} > 400^\circ\text{C}$ .

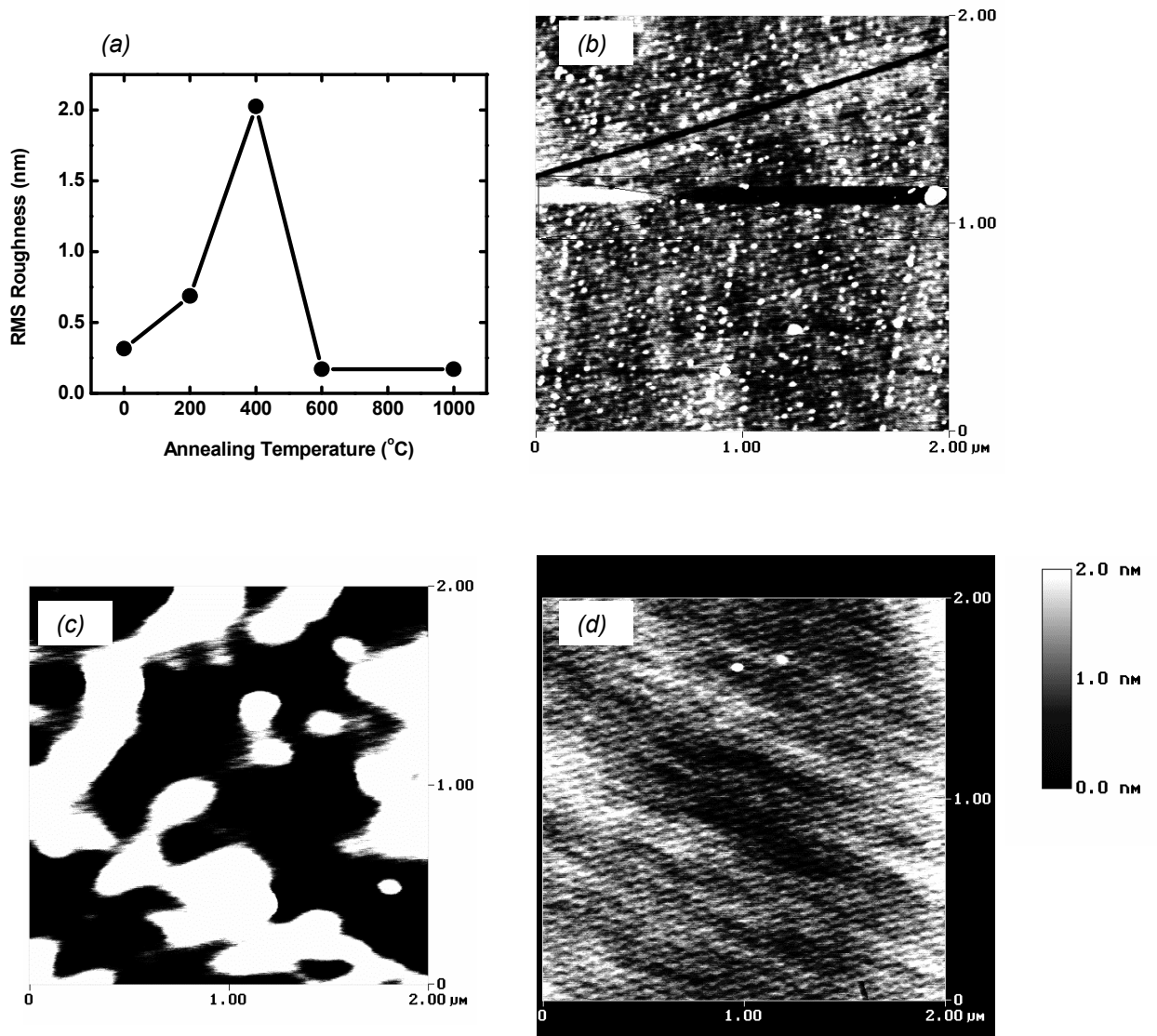


Figure 16 (a) RMS roughness as a function of  $T_{\text{ANNEAL}}$  for ZnO single crystals annealed in air. Error bars are within the size of the points on the plot. AFM surface morphology plots for (b) Unannealed single crystal ZnO, (c) 400°C and (d) 1000°C anneals. Diagonal lines are artifacts of the scanning process.

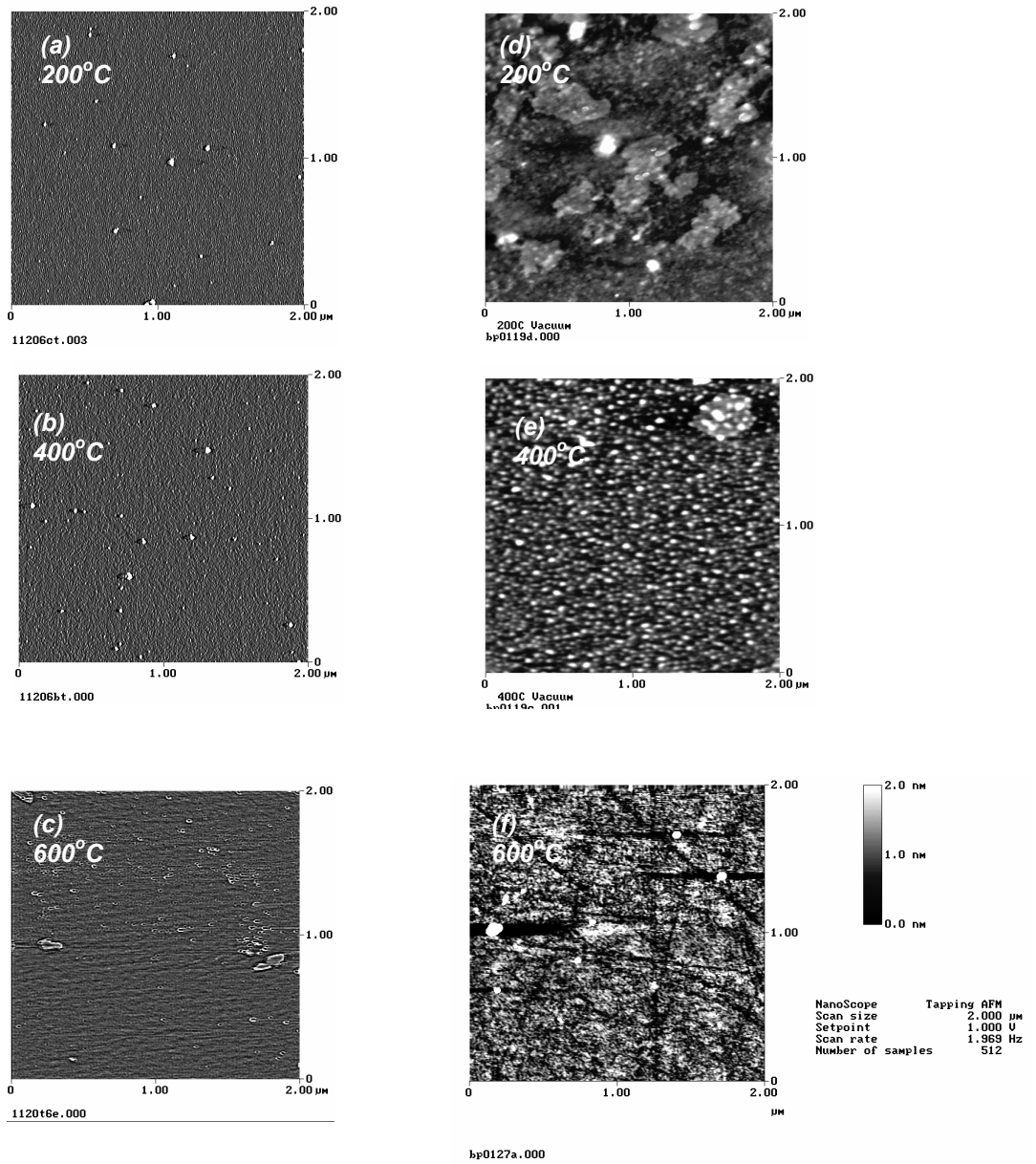


Figure 17 AFM images of samples annealed non-oxidizing ambients as a function of  $T_{ANNEAL}$ . Left column = argon-annealed, right column = vacuum-annealed. A height scale bar is provided in the lower right-hand column.

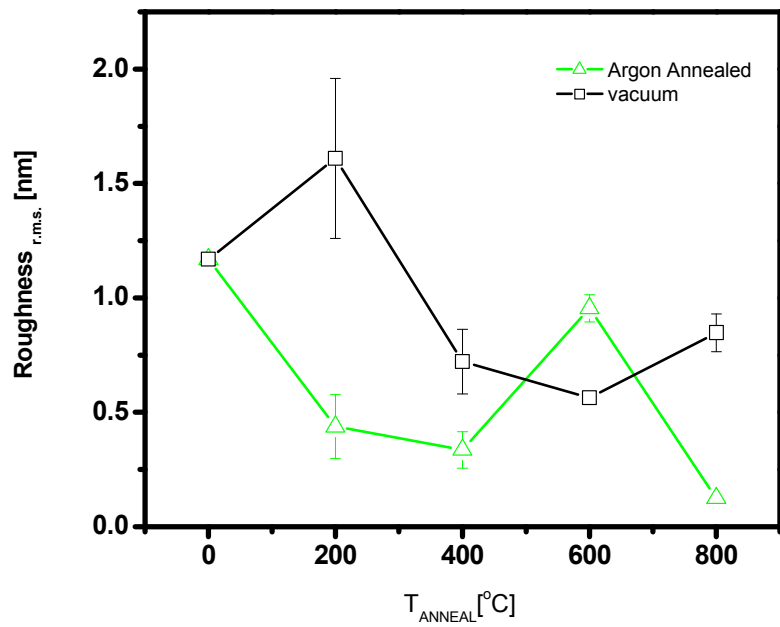


Figure 18 r.m.s. roughness for both non-oxidizing ambients—argon and vacuum.

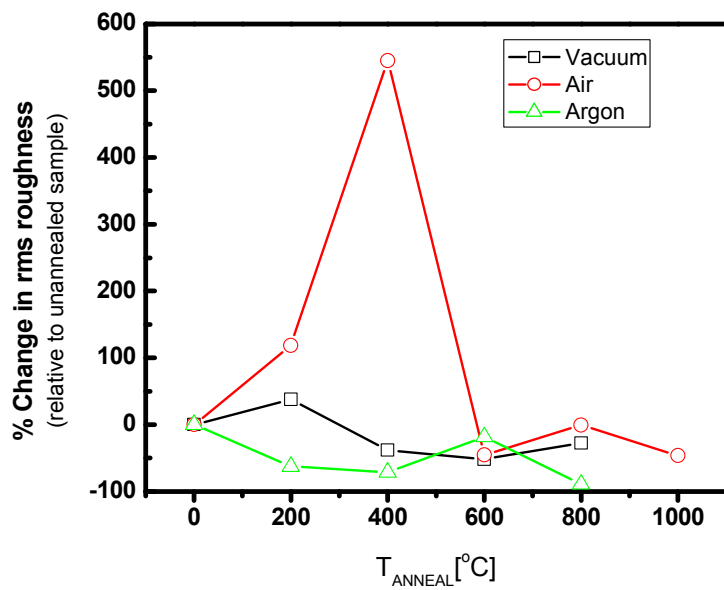


Figure 19 Percent change in r.m.s. roughness, relative to unannealed samples for all three annealing ambients.

### 5.3.2 Schottky Barrier Height

It is well-established that the formation of a Schottky contact is influenced by the surface chemistry of the semiconductor as well as interactions between the semiconductor and metal contact during processing. The presence of  $\text{Zn(OH)}_2$  and Zn-rich agglomerations would lead to variations in device properties, such as the Schottky barrier height ( $\phi_B$ ) and surface resistance as a function of  $T_{\text{anneal}}$ . A  $\text{Zn(OH)}_2$  will act like a thin insulating barrier, whereas a Zn-rich surface will act like a metallic contact<sup>112</sup>.

A survey of the literature shows a 20% drop in  $\phi_B$  comparing unannealed samples to samples annealed at  $200^\circ\text{C}$ <sup>113,114</sup>. Schottky junctions made with crystals annealed in air at higher temperatures ( $T < 500^\circ\text{C}$ ), show a saturation in the barrier value. The formation of  $\text{Zn(OH)}_2$ , which is an insulator, should lead to an increase in the Schottky barrier height if the surface is (0001)-oriented (Zn rich) due to the loss of metallic carriers from Zn atoms, now bound into the insulating  $\text{Zn(OH)}_2$ . It should lead to a reduction in the barrier height if the surface is (000 $\bar{1}$ )-oriented (O-rich), since some of the oxygen atoms will now have hydrogen surface terminations that serve as metallic,  $n$ -type carriers.

To confirm the presence of Zn-rich regions, Schottky barriers were fabricated onto the air-annealed ZnO single crystals using Au contacts. We used Schottky barrier measurements to better understand the surface composition variations with  $T_{\text{anneal}}$ . We applied non-reactive metal contacts (Au)<sup>115</sup> to the ZnO surface and conducted I-V measurements in order to extract the Schottky barrier height vs.  $T_{\text{anneal}}$ . Details on the

fabrication, measurement and analysis of the Schottky barriers can be found in Appendix 7.

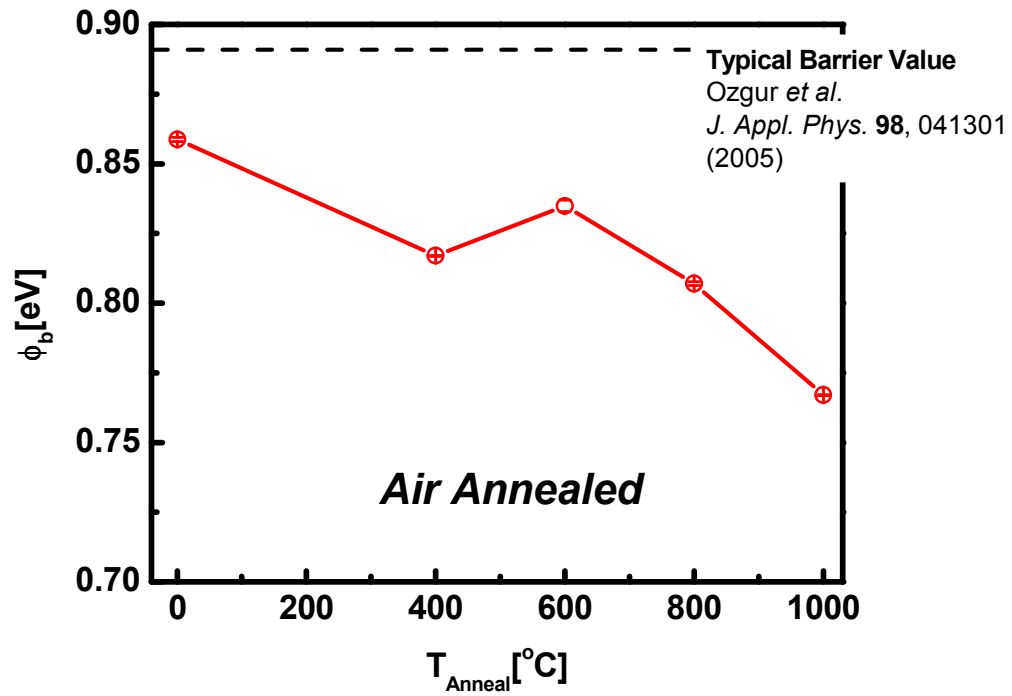


Figure 20 Schottky barrier height ( $\phi_B$ ) vs.  $T_{\text{Anneal}}$  for air annealed crystals.

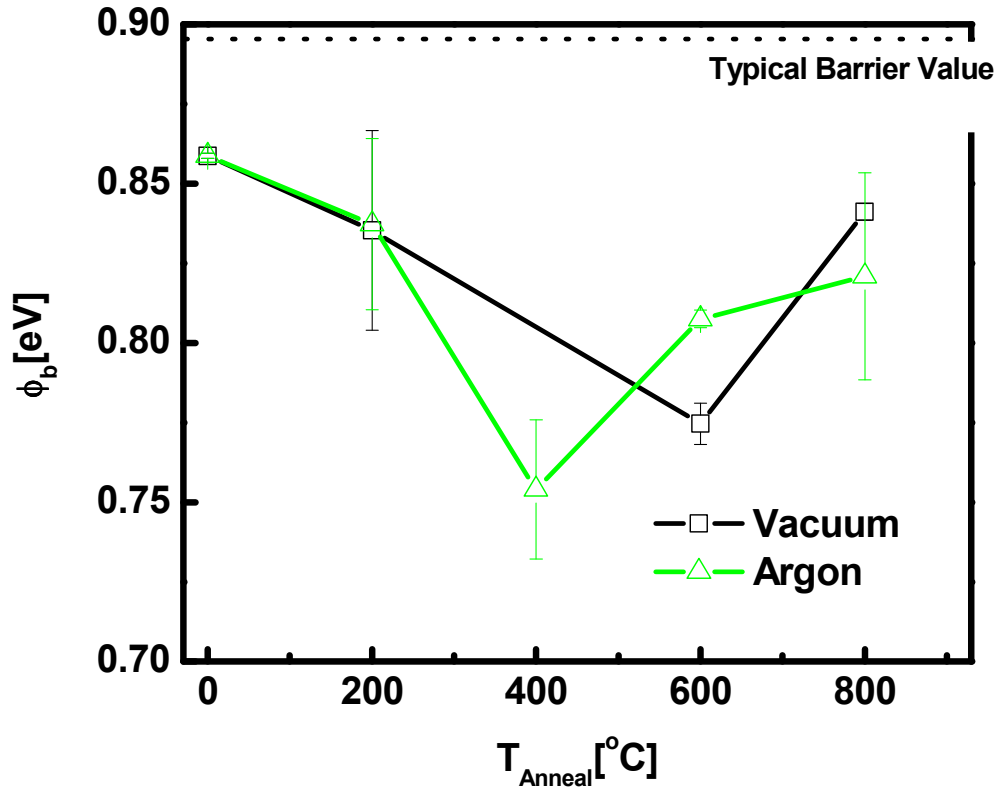


Figure 21  $T_{\text{ANNEAL}}$  dependence of Schottky barrier for argon- and vacuum-annealed samples.

All samples show Schottky barrier heights that are lower than the values reported in the literature. For air-annealed samples (Fig. 20), the barrier height shows a near-monotonic decrease with increasing  $T_{\text{Anneal}}$ . Argon-annealed samples (Fig. 21) show a minimum  $\phi_B$  at 400°C, close to the melting point of Zn at ambient pressure. Vacuum-annealed samples (Fig. 19) show a minimum in the barrier at 600°C.

For air-annealed samples, we observed a correlation between surface roughness and barrier height. For  $T > 600^\circ\text{C}$ , we observe the smoothest surfaces and  $T \geq 800^\circ\text{C}$ , we observe that the Schottky barrier monotonically decreases.

### 5.3.3 X-Ray Photoelectron Spectroscopy

The composition of surface pebbles on the air-annealed crystals was examined using XPS. Figure 22(a) shows XPS spectra of the O1s peaks for single crystals unannealed and annealed at  $T_{\text{ANNEAL}} = 400^{\circ}\text{C}$ ,  $600^{\circ}\text{C}$  and  $1000^{\circ}\text{C}$ . Three peaks were fit to the O1s data with  $r^2 > 0.99$  with a binding energy ( $E_B$ ),  $E_B \sim 530, 531$  and  $533$  eV. These three peaks correspond to three phases on the surfaces. An example of the fitting process is shown in Fig. 22(b).

The  $E_B \sim 530$  eV peak was attributed to  $\text{O}^{2-}$  on the ZnO wurtzite lattice<sup>116</sup>. From the mass concentration, on-stoichiometry ZnO is not the primary constituent at the surface.

The primary constituent of the single crystal ZnO surface is the O1s peak at  $\sim 531$  eV. The O1s binding energy of this peak is offset from the O1s position for optimally doped ZnO by  $-1$  eV<sup>117</sup>. This lower binding energy means that there is a weaker bond between Zn-O, suggestive of oxygen atoms being shared by more than 2 Zn atoms, implying that the Zn-O bonding is off stoichiometry, possibly due to interstitial Zn on the surface. An off-stoichiometry surface is consistent with the attribution of the 531 eV peak to  $\text{O}^{2-}$  ions in the oxygen-deficient regions of ZnO<sup>118</sup>. The third peak in the O1s spectrum has a binding energy of  $\sim 533$  eV and is associated with  $\text{Zn}(\text{OH})_2$ . This is consistent with our statement in Section 2.24, where the dominant form of hydrogen, unintentionally introduced to an O-terminated surface, would lead to the formation of a hydroxide.

The oxygen mass concentration for each of these peaks as a function of  $T_{\text{ANNEAL}}$  is shown in Figure 23(a). The total mass concentration of oxygen is approximately 70%, which is consistent with the commercial supplier's statement that the single crystal is (000 $\bar{1}$ )-oriented, that is, the surface is oxygen-terminated. Looking at Fig. 23(a), the primary constituent on the crystal surface is off-stoichiometry ZnO, specifically ZnO with oxygen-vacancies ( $\text{ZnO}_\delta$ ). O1s peaks associated with ZnO and off-stoichiometric ZnO showed a reduction in the mass concentration of oxygen for  $T_{\text{ANNEAL}} < 600^\circ\text{C}$ . Above  $600^\circ\text{C}$ , oxygen concentration increases, with the difference in the concentration of oxygen bound in ZnO and  $\text{ZnO}_\delta$  being constant (overall, there is a 5% difference in the mass concentrations for the two phases).

The Zn 2p peak contributions to the XPS spectra,  $2p_{1/2}$  and  $2p_{3/2}$  states<sup>119</sup> (Fig. 23 (b)), showed an increase in surface Zn concentration with  $T_{\text{ANNEAL}}$  up to  $600^\circ\text{C}$ . This indicates that Zn diffused from lower layers in the ZnO crystal, into the first 10 nm of the surface. The slope of the Zn  $2p_{3/2}$  curve is at its steepest where  $T_{\text{ANNEAL}} \sim 200^\circ\text{C}$ , indicating the largest change in mass concentration of Zn occurs in that temperature region.

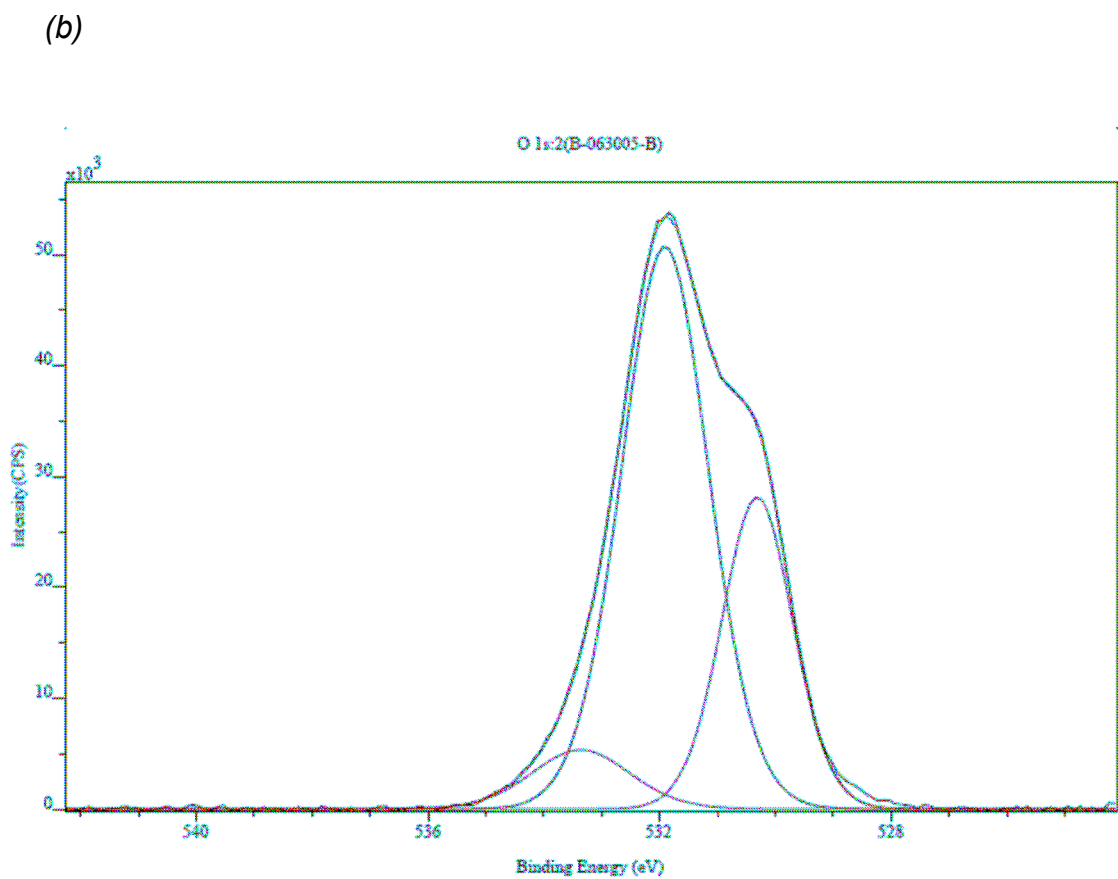
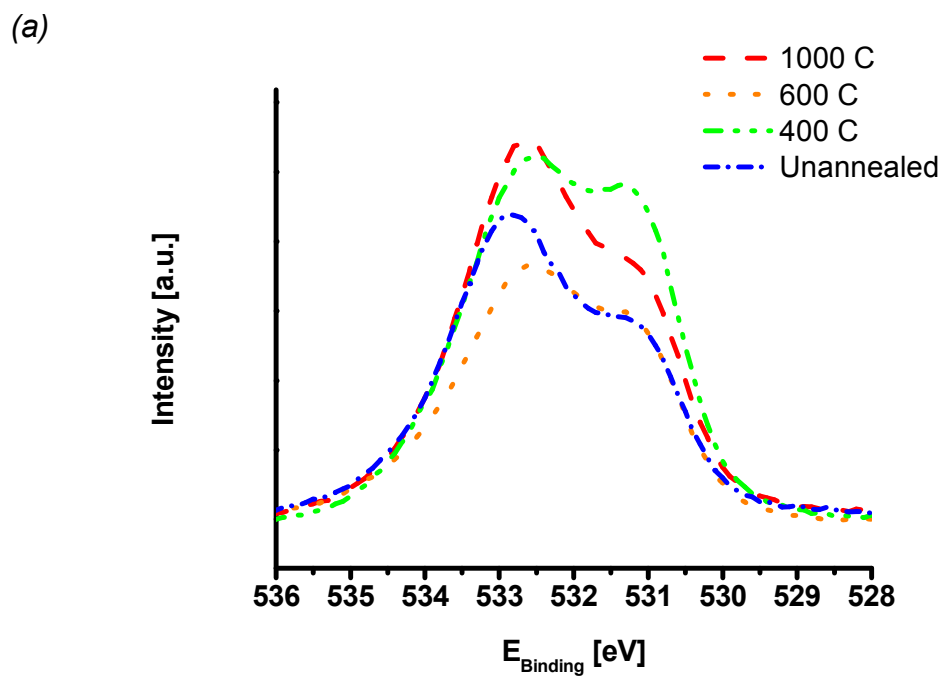


Figure 22 (a) O1 s spectra for ZnO samples annealed in air at  $T_{\text{anneal}} = \text{unannealed}, 400, 600$  and  $1000^\circ\text{C}$ . (b) An example of an O1s spectrum, uncorrected for adventitious carbon peak  $E_B$ , with fits.

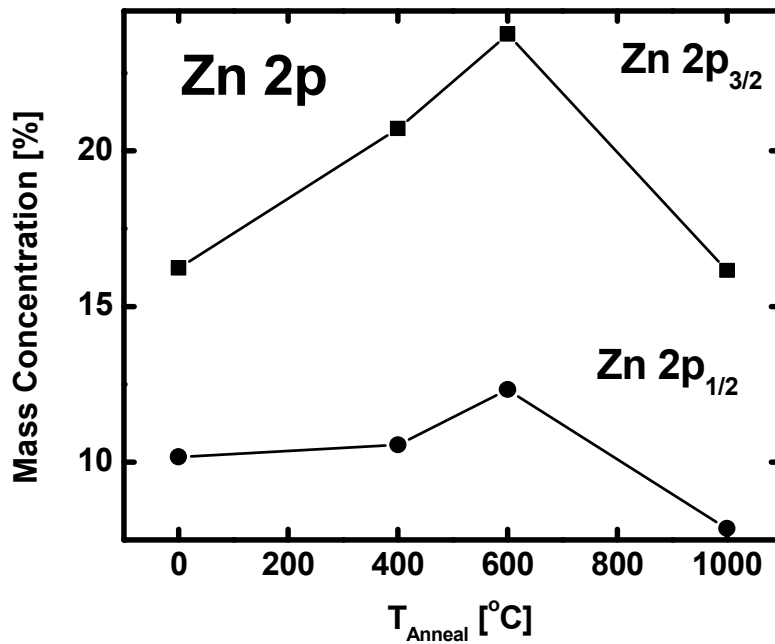
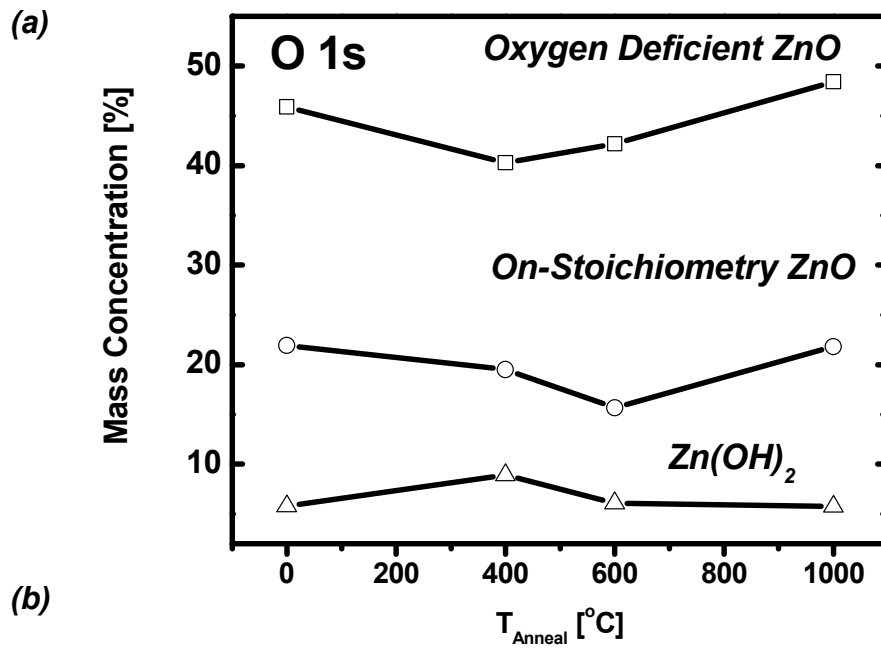


Figure 23

(a) O1s mass concentration of off-stoichiometry ZnO (ZnO, squares), on-stoichiometry ZnO (circles) and  $\text{Zn}(\text{OH})_2$  (triangles) as a function of  $T_{\text{A}}$ . (b) Zn 2p mass concentration vs.  $T_{\text{A}}$ .

Combining the XPS mass concentration results with AFM data we observed that there are two temperature regions for roughness generation: one for  $T_{\text{ANNEAL}} \leq 400^{\circ}\text{C}$  and another for  $T_{\text{ANNEAL}} > 400^{\circ}\text{C}$ .

For samples annealed at  $T_{\text{ANNEAL}} \leq 400^{\circ}\text{C}$  in air, XPS shows two main contributions to the surface roughness: excess Zn atoms and  $\text{Zn}(\text{OH})_2$ .

The roughness peaks at  $400^{\circ}\text{C}$ , which corresponds to a minimum in the oxygen-deficient phase of ZnO and a maximum in the mass concentration of  $\text{Zn}(\text{OH})_2$ .  $\text{Zn}(\text{OH})_2$  cannot be the primary source of roughness as its mass concentration represents only a 4 at. % change of the total O1s mass concentration. This is roughly equivalent to the growth of approximately 0.4 monolayers (1 at. % of OH is equal to 0.1 monolayer), making the total contribution of  $\text{Zn}(\text{OH})_2$  equal to approximately 1 monolayer at  $400^{\circ}\text{C}$ . Such a small change is consistent with the stabilization behavior of other polar oxide surfaces annealed and subsequently cooled at a slow cooling rate<sup>120</sup>. Thus, the primary source of morphological changes must arise from another source.

We argue that the source of morphological changes arises from the agglomeration of Zn atoms that have either diffused to the surface or are associated with the loss of surface oxygen. Fig. 24, which shows the total mass concentration for both Oxygen and Zinc, plotted vs.  $T_{\text{ANNEAL}}$ , shows a progressive increase in the mass concentration of Zn and a progressive decrease in surface oxygen mass concentration. That is to say that oxygen is leaving the surface and Zn is diffusing from the near-surface region to the immediate surface.

As  $T_{\text{ANNEAL}}$  increases beyond  $400^{\circ}\text{C}$ , Zn atoms at the surface either evaporate or oxidize and can contribute to the formation of on-stoichiometry or off-stoichiometry

ZnO. Mass loss or mass conversion (and subsequent integration into the host lattice) contributes to the overall smoothing of the surface. This is seen in the O1s mass concentration for all the phases. One example of mass conversion is  $\text{Zn(OH)}_2$  dehydrating into on-stoichiometry ZnO, which is a well-known conversion mechanism<sup>121</sup>. Conversion of the  $\text{Zn(OH)}_2$  is consistent with the O1s data for on-stoichiometric ZnO, which initially shows a drop for  $T_{\text{ANNEAL}} \leq 400^\circ\text{C}$ , but begins to rise for  $T_{\text{ANNEAL}} > 400^\circ\text{C}$ . The percent change in O1s mass concentration lost for the  $\text{Zn(OH)}_2$  peak between 400 and  $600^\circ\text{C}$  and the mass concentration gained by  $\text{ZnO}_\delta$  are equivalent, within experimental error.

The significance of  $T_{\text{ANNEAL}}$  is no coincidence. The melting temperature of Zn is  $410^\circ\text{C}$ <sup>122</sup>. The loss of Zn mass concentration observed via XPS is consistent with this explanation. Thus the mechanism for surface roughness generation is that Zn in the oxygen deficient ZnO near surface region is diffusing from the near-surface region to the immediate surface and agglomerating. The agglomerated Zn atoms and, to a lesser extent, the  $\text{Zn(OH)}_2$  are the sources of roughness for samples annealed in air for  $T_{\text{ANNEAL}} \leq 400^\circ\text{C}$ .

As  $T_{\text{ANNEAL}}$  increases above  $400^\circ\text{C}$ , the Zn-rich surface melts, followed by oxidation of the residual Zn atoms or evaporation of those atoms, producing regions of either stoichiometric or non-stoichiometric ZnO. The oxidation or loss of the excess surface Zn leads to an overall smooth surface.

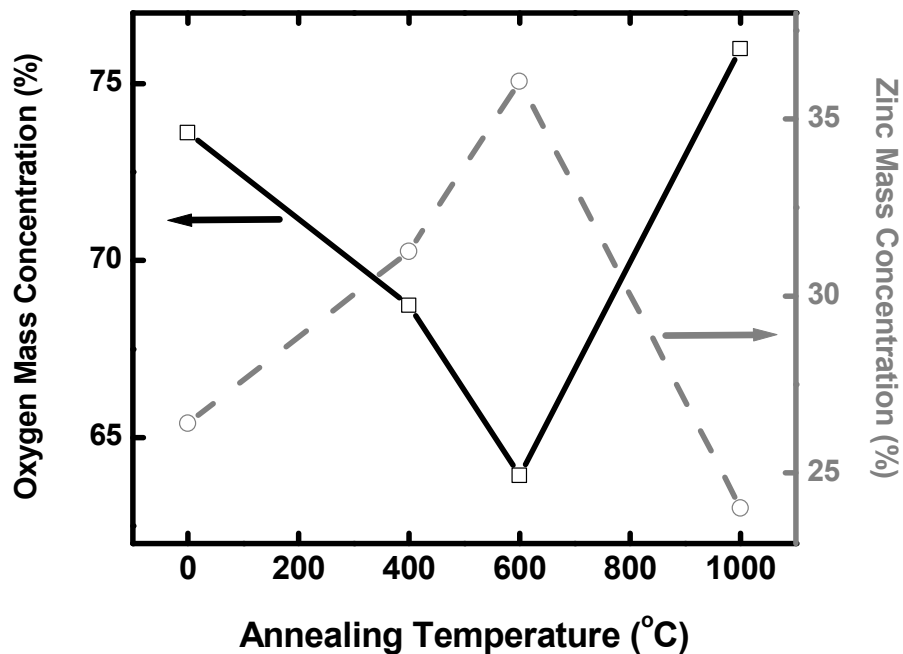


Figure 24 Comparison of total oxygen mass concentration (squares) with total zinc mass concentration (circles) as a function of annealing temperature. Mass concentration for oxygen and for zinc were calculated independently using the approach discussed in Appendix 5.

Returning to the Schottky barrier height data—recall that barrier height starts out at 0.86 eV for unannealed samples and drops by 5% when annealed at 400°C. The decrease in the barrier height at this annealing temperature is the point at which Zn(OH)<sub>2</sub> is at its maximum and the non-stoichiometric ZnO is at its minimum. Oxygen on the oxygen-rich surface is being consumed and terminated with carriers that participate in the conduction process, leading to a surface that is overall more metallic in character at 400°C. At 600°C, there is a ~2.5% rise in the barrier height relative to the 400°C barrier. This corresponds to the minimum in oxygen concentration and maximum in Zn concentration in the XPS data. As  $T_{\text{anneal}}$  increases further,  $\phi_B$  continues to drop.

From the XPS data alone, we concluded that the source of variable surface morphology for samples annealed in arises from surface agglomeration of Zn. The reduction of the Schottky barrier for single crystals annealed at  $T_{\text{anneal}} < 500^{\circ}\text{C}$  is consistent with an increasingly more metallic surface, as would be the case for migration and coalescence of Zn atoms from ZnO. Thus, the increase in roughness from 200-400 °C is likely attributable to the out-diffusion of Zn atoms and is consistent with the rise in Zn mass concentration observed in the surface region via XPS. As  $T_{\text{Anneal}}$  increases, these atoms likely oxidize or evaporate.

#### ***5.3.4 Rutherford Backscattering Spectrometry***

If, as the XPS and Schottky barrier results from the previous section indicate, Zn is diffusing from the near-surface region of the single crystal towards the surface or oxygen is leaving the near-surface region, then atomic positions in the near-surface lattice are experiencing a local reordering in response. This local crystalline reordering should be observable (in both composition and crystallinity) via Rutherford Backscattering Spectroscopy (RBS).

The full RBS channeling spectra for air-annealed samples are shown in Fig. 25. The Zn edge and O peak are labeled.

Looking at channeling of the Zn peak as a function of  $T_{\text{ANNEAL}}$  (Fig. 26), we see two main changes with increasing  $T_{\text{ANNEAL}}$ :  $\chi_{\text{min}}$  peaks at 200°C, indicating that atomic positions are maximally changing at quite a low temperature and then monotonically decreases with increasing  $T_{\text{ANNEAL}}$ .

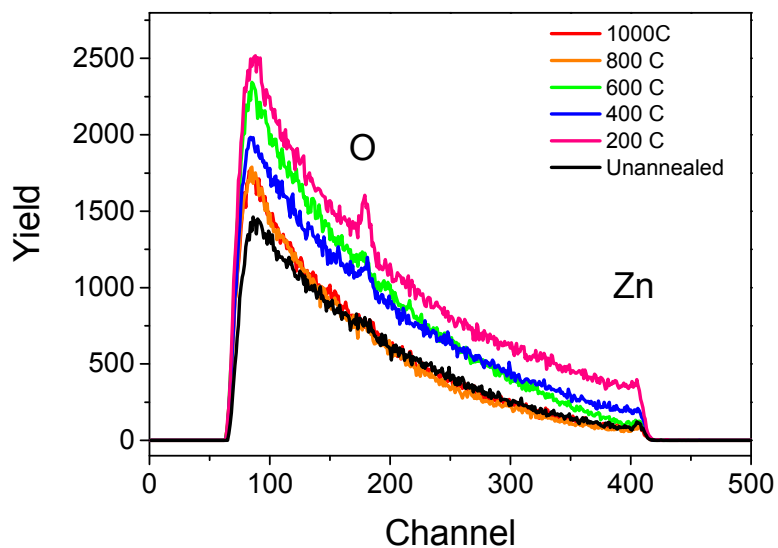


Figure 25 RBS Spectra for air-annealed single crystals at various  $T_{\text{ANNEAL}}$

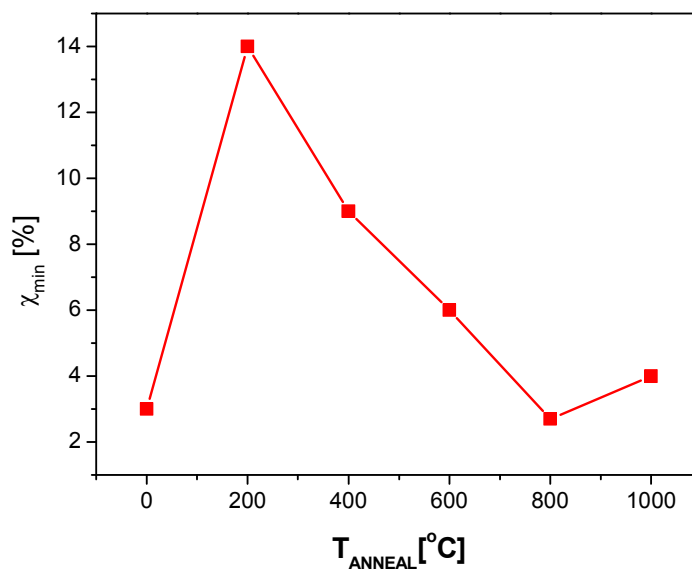


Figure 26 Channeling yield vs. annealing temperature for single crystal ZnO annealed in air.

XPS showed that Zn atoms increase in concentration at the surface (Section 5.3.2). RBS shows a temperature-dependent variation in the channeling, whose measurements include the surface, but probe into a depth that is greater than the  $\sim 10$  nm probed by XPS. The rise in the channeling peak for samples annealed at  $T_{\text{ANNEAL}} =$

200°C, combined with the Zn XPS data are evidence that Zn diffuses from the first 20 – 100 nm depth (the depth probed by RBS channeling) towards the surface. In channeling mode, RBS is a near- surface probe (20-100 nm), the region where the lattice reorders. Since the channeling data shows atomic disruptions (increases in  $\chi_{\min}$ ) for samples annealed at lower  $T_{\text{ANNEAL}}$ , we conclude that channeling has the capacity to detect the onset of diffusion in ZnO prior to the appearance of Zn at the surface, making RBS in channeling mode a predictor of the onset of diffusion. Thus, it can be said that the peak that was observed in  $\chi_{\min}$  at  $T_{\text{ANNEAL}} = 200^\circ\text{C}$  is a thermal snapshot of the beginning of the diffusion process.

Looking at the channeling yield as a function of  $T_{\text{ANNEAL}}$  for the samples annealed in non-oxidizing ambients (Fig. 27), we see channeling yields for samples annealed in argon and vacuum show peaks with  $\chi_{\min} \sim 14 - 16\%$ . This is comparable to the  $\chi_{\min}$  of the air-annealed sample and suggests that the degree of disorder for ZnO is independent of annealing ambient. Like the air-annealed samples, samples annealed in argon and vacuum showed similar maximum values for  $\chi_{\min}$ . All samples showed a minimization of  $\chi_{\min}$  for  $T_{\text{Anneal}} \geq 800^\circ\text{C}$ .

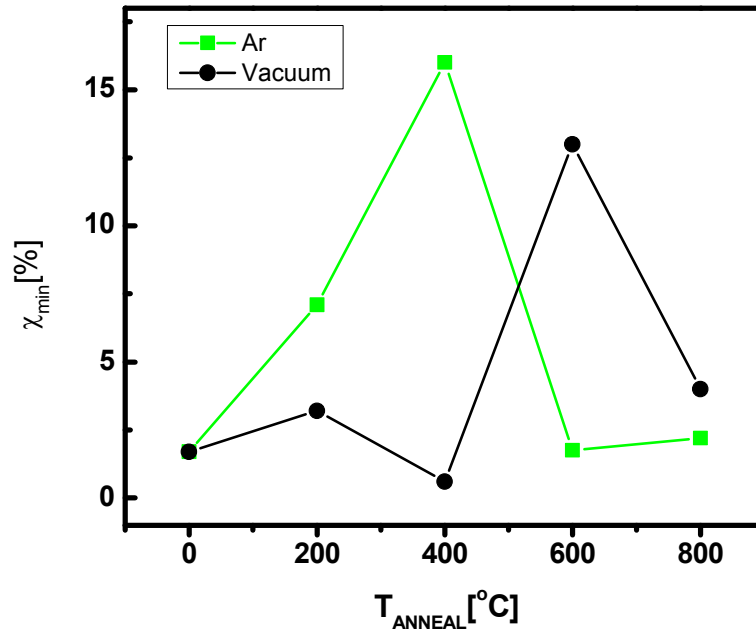


Figure 27 RBS channeling yield for argon- and vacuum-annealed samples.

### 5.3.5 X-ray Diffraction

Strain effects are dependent upon the different annealing ambients. Air-annealed and vacuum annealed (Fig. 28 (a), (c)) samples show c-axis strain that is < 1%. Argon-annealed samples show a large, temperature dependent variation in strain (Fig. 28 (b)). This contrasts with the behavior of the c-axis rocking curve FWHM (Fig. 29). The temperature dependence of strain appeared to be similar to the temperature dependence observed in channeling.

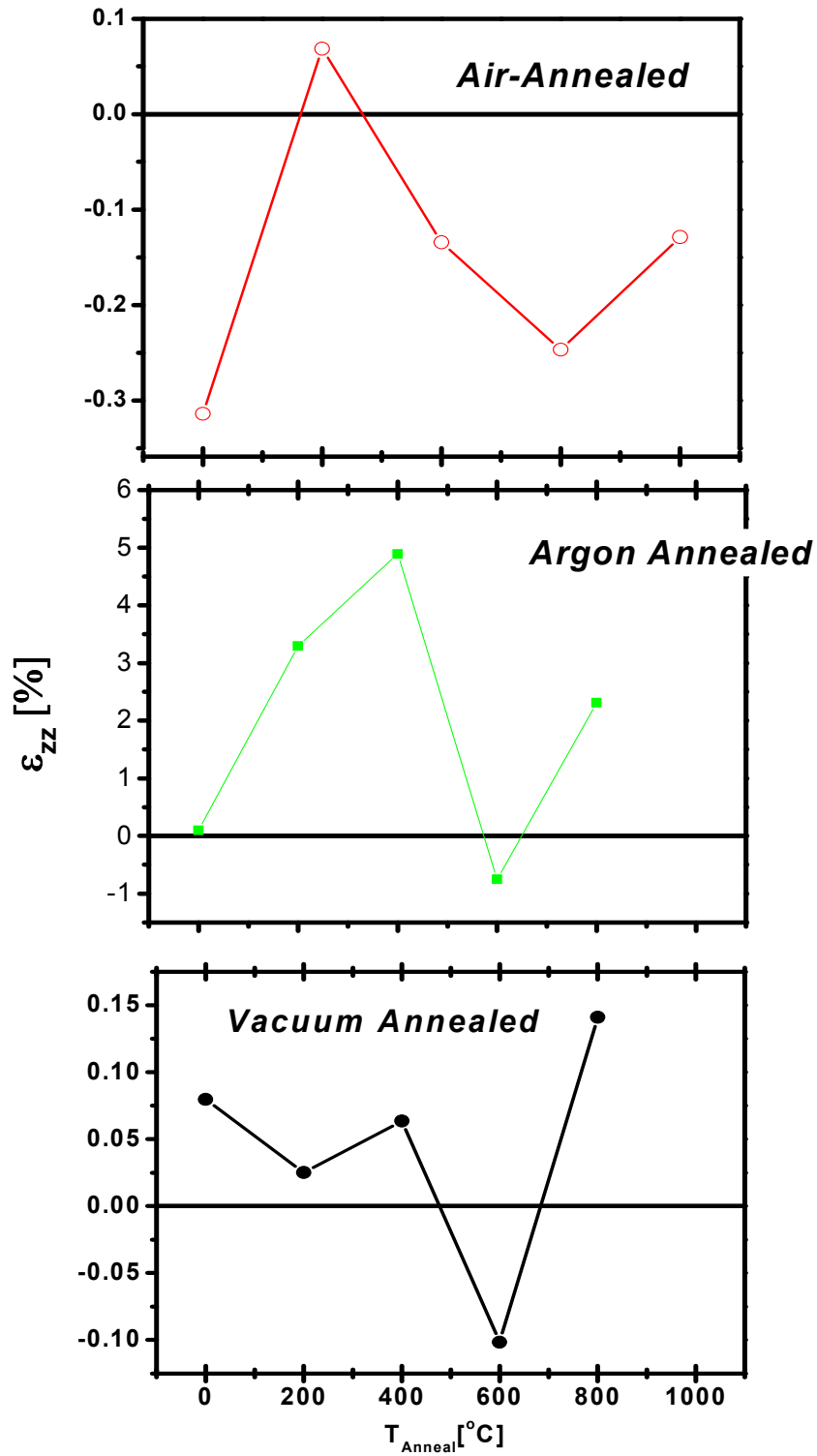


Figure 28 Strain vs.  $T_{\text{anneal}}$  for air-annealed (a), argon-annealed (b) and vacuum-annealed samples (c).

### ***Correlating Crystallinity as Measured via XRD to Channeling***

Temperature-dependent changes in the crystal structure can be further probed at a greater depth in the sample using x-ray diffraction (XRD) rocking curves. In the same way that  $\chi_{\min}$  is often invoked as a measure of crystallinity, the FWHM of an x-ray diffraction rocking curve is informally referred to as a measure of “the degree of crystallinity” for a film or single crystal. Typically, the parallels between FWHM and channeling yield that are typically made in the literature are informal and of a limited capacity--the literature connects a low value of channeling yield or narrow FWHM with well-oriented samples. In this section, we show that the parallels between  $\chi_{\min}$  and the FWHM of the x-ray rocking curve are measures of disruptions in crystallinity with two very important differences:

- *Depth of Measurement:* RBS Channeling is limited to 100 nm at most, whereas XRD rocking curves probe 100s of microns.
- *Sensitivity to Atomic Displacements:* RBS and XRD both show results of a superposition of atomic displacements from a variety of sources. XRD has the advantage of directly measuring interlattice separations as well as strain, whereas RBS indirectly measures such separations.

Broadly speaking, the XRD FWHM does reflect the degree of crystallinity. However, there are several terms that influence the FWHM of a rocking curve:

$$\beta_m^2(hkl) = \beta_o^2(hkl) + \beta_d^2(hkl) + \beta_\alpha^2(hkl) + \beta_\varepsilon^2(hkl) + \beta_L^2(hkl) \quad (5.1)$$

Where  $\beta_o^2(hkl)$  = the intrinsic rocking curve; the lowest possible value for a perfect single crystal,  $\sim 10$  arcseconds;  $\beta_d^2(hkl)$  = instrumental broadening;  $\beta_\alpha^2(hkl)$  = mosaicity-rotation at dislocations;  $\beta_\epsilon^2(hkl)$  = strain broadening (surrounding dislocations);  $\beta_L^2(hkl)$  = crystal size broadening.

The minimum channeling yield is related to the atomic spacing:

$$\chi_{\min} = N d \pi \rho^2 \quad (5.2)$$

Where  $N$  = number of atoms,  $d$  = atom spacing in a given row of atoms and  $\rho$  = r.m.s. thermal vibration amplitude of the atoms in the lattice in the plane of the sample.

Isolating each term directly can be challenging, since a detailed knowledge of the thermal vibration amplitude is needed and there are limits in measuring the number of atoms via RBS.

Thus, the convention to correlate FWHM to  $\chi_{\min}$  seems to have limited application to samples whose crystallographic orientations are equivalent when looking parallel and perpendicular to the surface (cubic structures and perhaps mildly orthorhombic structures). This is a consequence of the fact that channeling measures atomic displacements perpendicular to the surface normal, whereas FWHM is a measure of lattice displacements parallel to the surface normal.

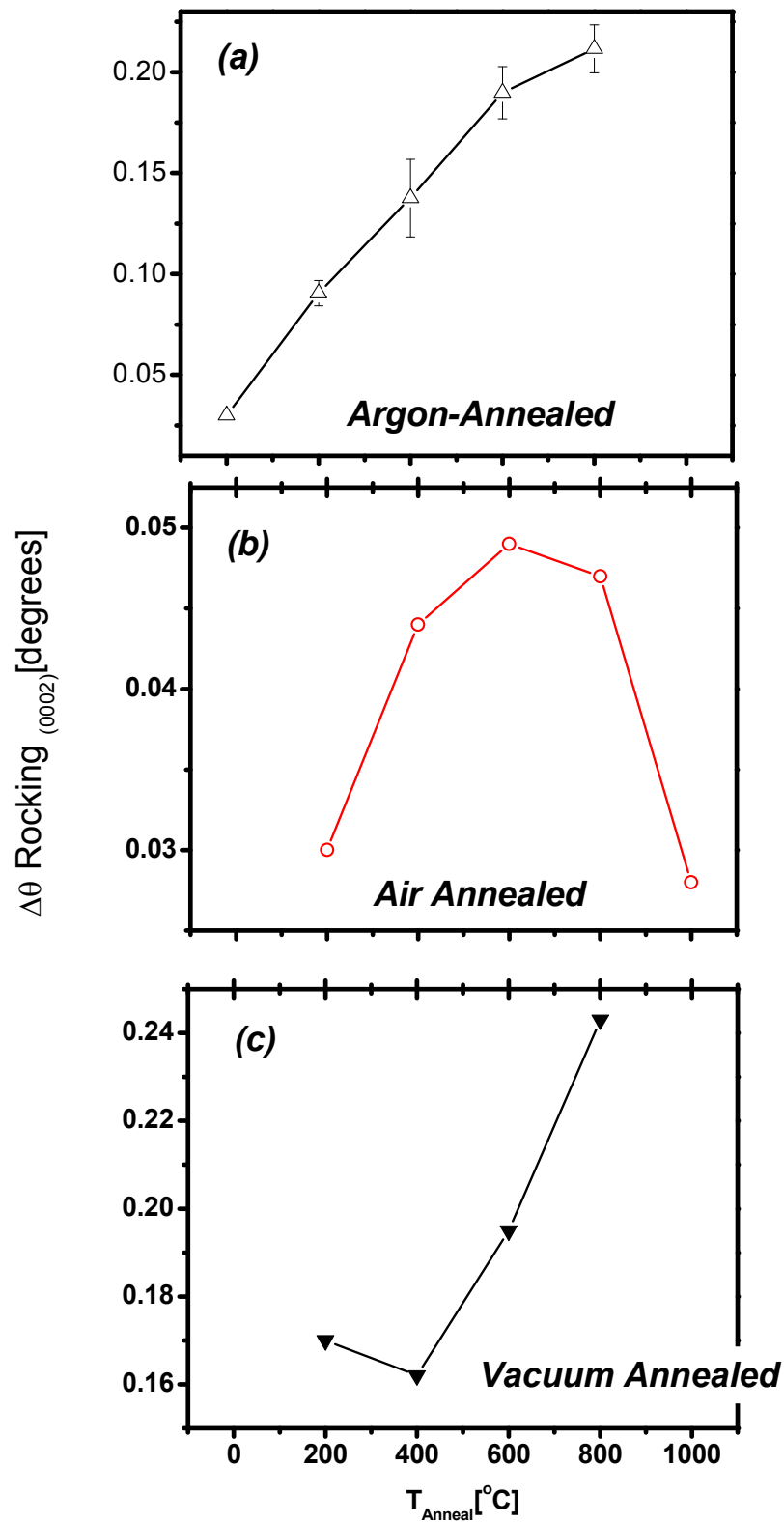


Figure 29 c-axis FWHM vs.  $T_{\text{Anneal}}$  for (a) air-, (b) argon- and (c) vacuum-annealed samples.

We tested these limitations by comparing the RBS channeling and XRD FWHM data for the different annealing ambients. For samples annealed in air, the FWHM of

the (0002) rocking curve broadens with increasing  $T_{\text{Anneal}}$ , (Fig. 29 (a)) but unlike, channeling, it does not peak at  $T_{\text{ANNEAL}} = 200^{\circ}\text{C}$ . Since it is widely accepted that channeling and FWHM are invoked during discussions of the “degree of crystallinity,” this discrepancy is surprising.

If instead, we look at a direct measure of the lattice spacing, via the  $c$ -axis length or even the strain,  $\varepsilon_{zz}$ , air-annealed films show a dip at  $200^{\circ}\text{C}$ , indicating a sudden change from a state of mild tensile strain to a state of mild compressive strain. Thus, the strain is a better parallel to  $\chi_{\text{min}}$ . This is consistent with the 0<sup>th</sup> order equation for channeling yield, which is dependent upon atom spacing, as well as all higher order approximations<sup>123</sup>. While there is some correlation between channeling yield and FWHM of a given orientation, in this case, the channeling yield has a stronger correlation as a function of  $T_A$ , to the uniaxial strain component along the  $c$ -axis direction,  $\varepsilon_{zz}$ , calculated relative to the bulk value, as listed in the JCPDS<sup>124</sup>.

Analogous to the undoped thin films, the generation of oxygen vacancies would lead to a reduction in lattice volume, giving rise to compressive strain. The vacancies are likely oxygen vacancies (vs. Zn vacancies) due to the lower enthalpy of formation of  $V_o$  vs.  $V_{\text{Zn}}$  as well as the low diffusion barrier associated with oxygen vacancies and is predicted upon formation of oxygen vacancies<sup>125</sup>. Such a large lattice relaxation from a previously strained state is observed in the argon-annealed samples for  $T_{\text{ANNEAL}} > 400^{\circ}\text{C}$ . The formation of these vacancies may be associated with the low diffusion barrier for oxygen in ZnO<sup>126</sup>.

### 5.3.6 Photoluminescence Spectroscopy

In the previous chapter, we used UV-Vis spectrophotometry in order to measure  $E_{\text{gap}}$ . That technique is well-suited for measuring thin-film or transparent semiconductors, but is not suitable for samples that are not fully transparent or are thick (as is the case for our work with single crystals). In order to measure the optical properties of the single crystal samples vs.  $T_{\text{anneal}}$ , photoluminescence (PL) was conducted.

PL is a near-bulk sensitive measurement that non-destructively evaluates the electronic structure of a solid. PL probes a depth on the order of 10s of microns. Like UV-Vis spectrophotometry, it is possible to measure  $E_{\text{gap}}$  as well as measure defect states in the material using PL. Please see Appendix 3 for a detailed overview of the technique.

A typical PL spectrum for ZnO contains two significant classes of emission lines: UV and visible. Emission lines in the UV region are a consequence of direct recombination of free exciton pairs, associated with the band-edge and near-band edge states. Visible emission lines are a consequence of radiative recombination centers associated with defect states and possibly states within the gap.

Three main regions of emission lines can be found in ZnO PL spectra—UV, green and yellow wavelength regions. These are listed in Table 6.

**Table 6: Common peaks found in ZnO photoluminescence spectra**

Energy [eV]	Transition	Reference
5.4	Zn intersititals	127
3.38 – 3.45	DX and AX complexes	
3.37	Band Edge	128
3.20	Donor-Acceptor Pair (DAP)	132
3.16	DAP	
3.10	DAP	
3.06	Zn vacancy, $V_{Zn}$	129,130,131,132,133
2.36	Oxygen intersitital, $O_i$	134, 135
2.2	$Li^+$ Impurities	136
2.07	Oxygen Vacancy, $V_O$	137, 138, 139

### 5.3.6. a Results: Main Spectral Lines (not associated with defects)

*Band Edge Peak:* In the case of the air-annealed samples, the population of states that luminesce at 3.37 eV at room temperature has a maximum for samples annealed at 400°C and declines with increasing  $T_{anneal}$ . This indicates the formation of non-radiative recombination centers. This behavior is consistent with existing thermal oxidation studies on Zn metal thin films exposed to oxidizing ambients, which attribute the peaking of the PL band edge peak intensity at  $T_{ANNEAL} = 400^\circ\text{C}$  to improved crystallinity of the thin films in this study<sup>140</sup>.

The vacuum annealed sample showed distinct peaks on the tail of the band edge of the band-edge peak. These peaks are typically observed for PL taken below room temperature. Typically, PL spectra of ZnO single crystals of films taken at room

temperature show quenched spectral line intensities<sup>141, 142</sup> or lines that are thermally smeared into a single band<sup>143</sup>.

When argon gas is introduced into the annealing ambient, these features become less and less distinct. For example, the Argon annealed samples do show peaks at the zero-, one-, two-, and three-LO-phonon assisted donor-acceptor pair transitions, but of lower intensity for all  $T_{\text{ANNEAL}}$ .

*Near Band Edge Peak:* The feature that contributes to the near-band edge peak at  $\sim 3.20$  eV shows an intensity that peaks at  $T_{\text{ANNEAL}}$ . This peak is attributed to the donor-acceptor pair transition<sup>144</sup>.

The fact that this peak shows up is an indication that there are acceptor complex states in the crystal, but they are of much lower concentration than the donor states. The intensity of the near-band edge peaks at  $400^\circ\text{C}$ . For  $T_{\text{ANNEAL}} > 400^\circ\text{C}$ , the intensity of the near-band edge peak drops below the intensity of the unannealed sample, indicating that the near-band edge peak contribution is reduced for  $T_{\text{ANNEAL}} > 600^\circ\text{C}$  beyond that of the pristine, unannealed state.

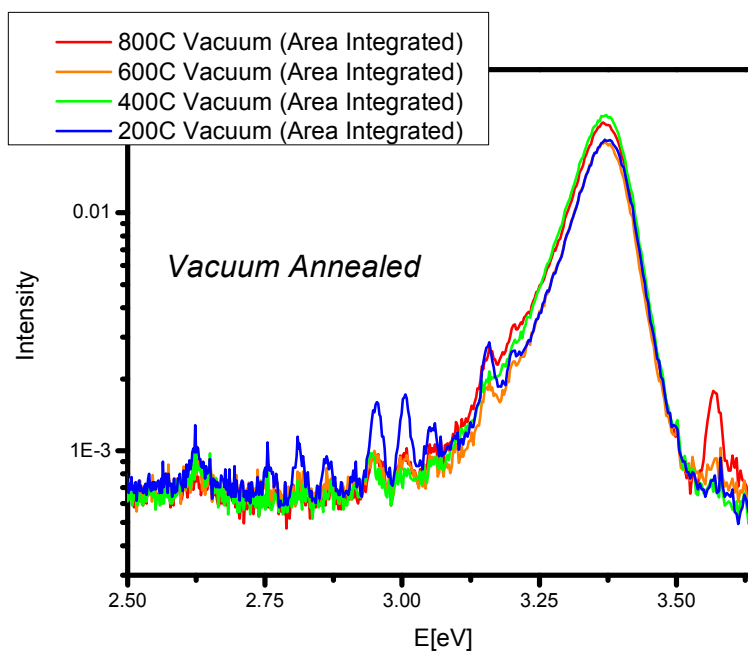
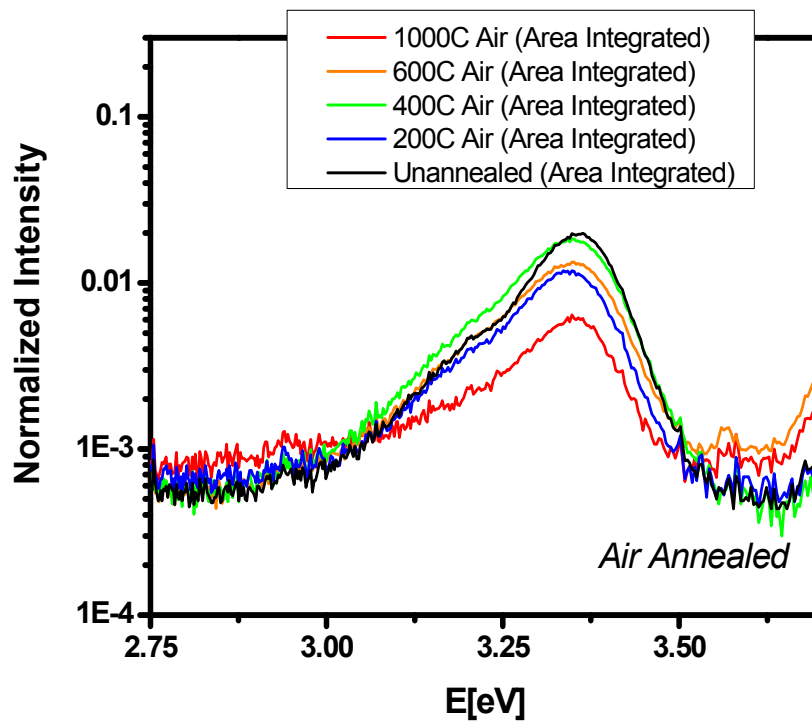


Figure 30 PL spectra of band edge peak for different  $T_{\text{ANNEAL}}$  for vacuum-annealed samples.

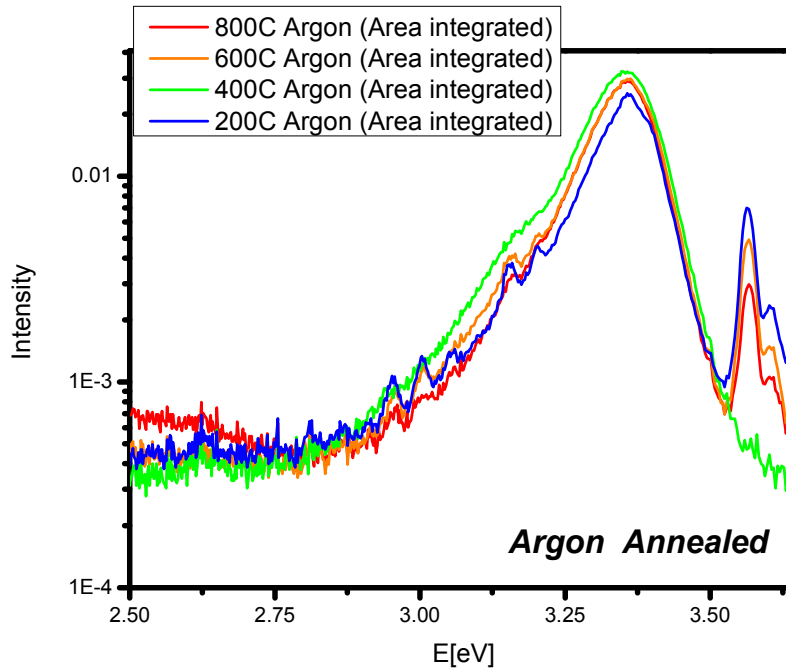


Figure 31 PL spectra of band edge peak for different  $T_{\text{ANNEAL}}$  for air-annealed samples.

### 5.3.6. b Results: Defect-Associated Spectral Lines

Two main classes of defect-associated spectral lines were observed:

- Lines associated with the formation of donor and acceptor complexes, *DX and AX Centers*
  - Lines associated with  $V_{\text{O}}$  and  $\text{Zn}_i$ : *Green Band* defects
- 
- *DX and AX Centers*

The band-edge PL peaks of samples annealed in all three ambients are asymmetric. The asymmetry is associated with several different states that are associated with donor-acceptor pairs, AX and DX centers. The presence of a DX center

is of significance to our quest to *p*-type dope ZnO, as the presence of a DX center has the capacity, via the introduction of donor states, to compensate efforts to *p*-type dope ZnO. Thus, in evaluating single crystals thermally treated at a range of deposition temperatures, in three different deposition atmospheres, we were able to gain a better understanding of those conditions that might best support *p*-type doping using a single crystal approach (discussed in Section 6.4).

The peak at 3.2052 eV was attributed to the donor-acceptor pair transition. Fig. 30 shows that this portion of the spectrum is dominated by the DX center contribution near 3.37 eV.

Individual peaks appear between 3.30 – 3.63 eV, associated with DX and AX complexes<sup>145</sup>. These are of highest intensity for argon-annealed samples and of lowest intensity for air-annealed samples.

The DX center states around 3.50-3.60 eV are of significance. Co-existence of donor (DX) states and acceptor (AX) complexes in phosphorus-doped thin films of ZnO are considered a possible source of thwarted *p*-type conductivity in ZnO<sup>146</sup>. The competition between the donors from the DX states with acceptors in the AX states was shown to produce an ambiguous electrical conductivity. Hence, annealing conditions which minimize DX centers may yield a higher change of producing *p*-type conductivity in ZnO.

Peaks at 2.954, 3.006, 3.052, 3.098, 3.159 eV are identified as zero-, one-, two-, and three-LO-phonon assisted donor-acceptor pair transitions. They are equivalently spaced with a separation of  $\sim 55$  meV. This is consistent with reports of LO-phonon

mode energy in ZnO<sup>147</sup>. These LO-phonon assisted donor-acceptor pair transitions are known to be associated with samples possessing rough surfaces<sup>4</sup>.

In this case, air-annealed samples show the lowest intensity for the DX center peaks. Thus, of the three annealing ambients, air-annealing will provide the best opportunity for *p*-type doping ZnO using single crystals.

- *Green Band:*

Five sharp peaks at  $E \sim 2.05, 2.12, 2.37, 2.48, 2.63$  eV were observed to be superimposed on top of the wide green band spectra.

In ZnO thin films, the peak at 2.48 eV, superimposed upon the wide green band, is thought to be associated with deep donor level oxygen vacancies, as it shows a reduction in PL intensity with increasing  $p(\text{O}_2)$ <sup>148</sup>. The thought is that increasing  $p(\text{O}_2)$  will be adsorbed by the ZnO film, helping to fill oxygen vacancies and reducing the deep donor level contribution to the PL spectrum.

Samples annealed in argon at low  $T_{\text{ANNEAL}}$  (200°C and 400°C) do not possess a broad green band emission (Fig. 32). They do show isolated emission peaks. As  $T_{\text{ANNEAL}}$  increased, the defect states broadened into a typical green band, similar to what was observed in the air-annealed samples. It is an indication that samples annealed in Argon have some amount of off-stoichiometry. The degree of the off stoichiometry worsens with increasing temperature. Air Annealed samples have a lesser degree of off stoichiometry (Fig. 32).

Unlike the argon- and air-annealed PL spectra, PL spectra of vacuum annealed samples do not show a broad green band (Fig. 33). The lack of a green band indicates

that a continuum of defects does not exist. Isolated peaks do appear within the green band region. These same isolated states were observed in argon-annealed samples.

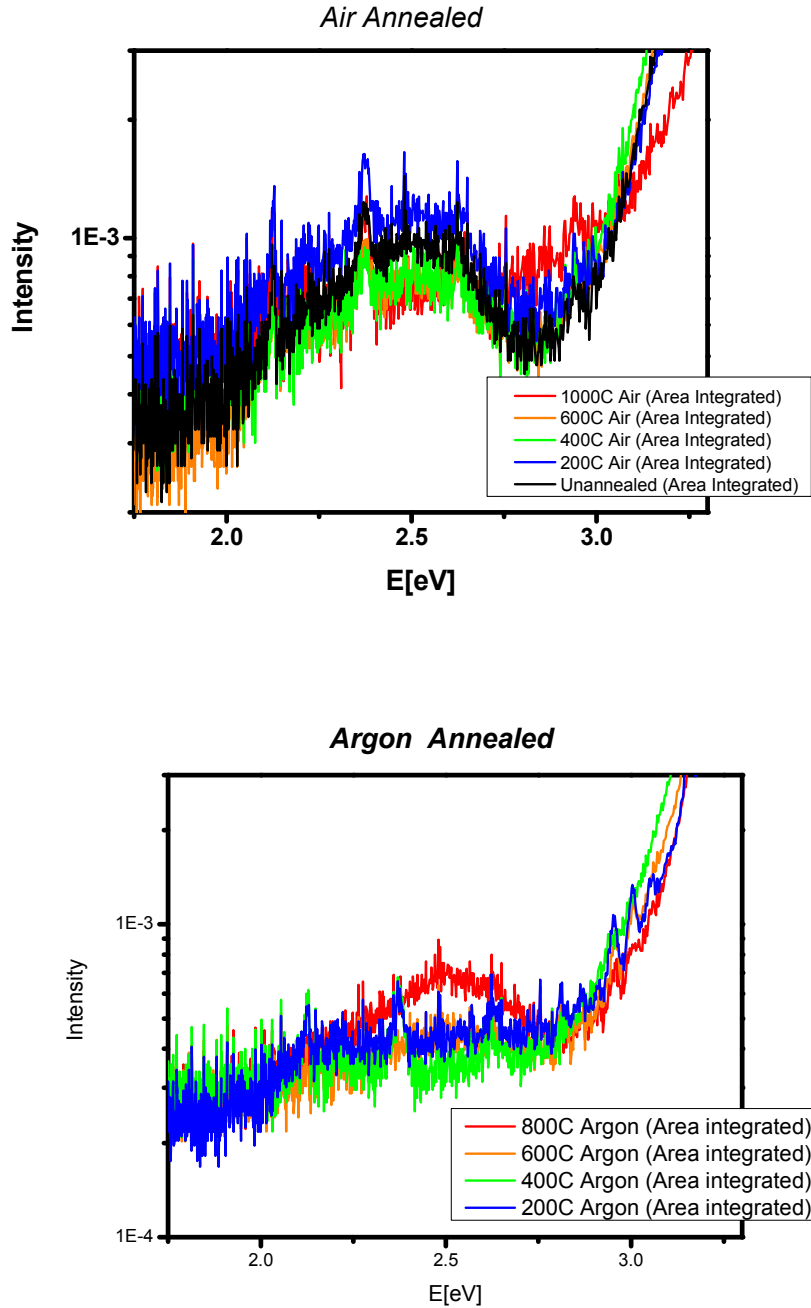


Figure 32 Green band region of PL spectrum for undoped single crystal ZnO annealed in air (top) and argon (bottom) at a range of  $T_{\text{Anneal}}$

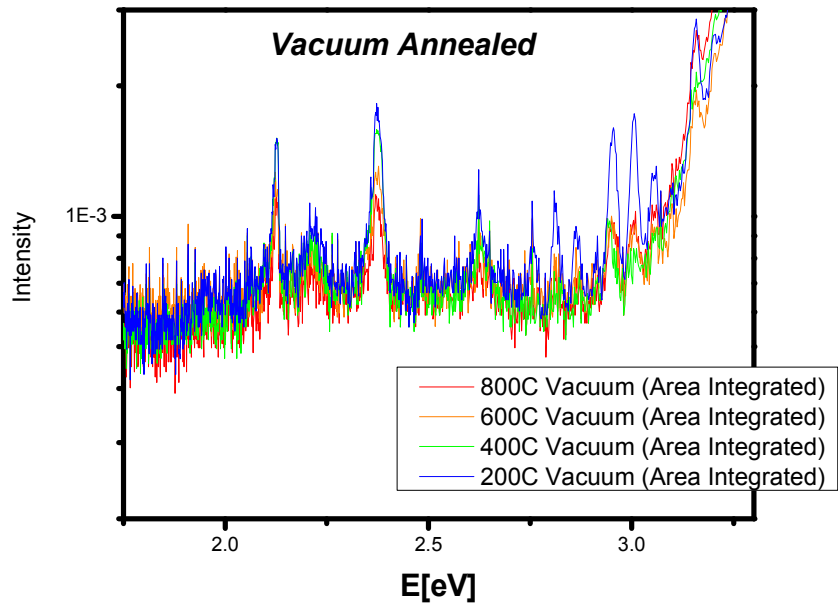


Figure 33 Green band region of PL spectrum for undoped single crystal ZnO annealed in vacuum at a range of  $T_{\text{Anneal}}$

# Chapter 6: Phosphorus Dopant Incorporation in ZnO Thin Films and Single Crystals

## 6.1 The History of Phosphorus as a *p*-type Dopant in ZnO

### 6.1.1 Thin Film Doping

Phosphorus has been introduced as a dopant to ZnO thin films using a variety of different sources including—ion implantation of P ions<sup>149</sup> and various solid sources such as Zn<sub>3</sub>P<sub>2</sub><sup>150,151</sup> and P<sub>2</sub>O<sub>5</sub> (phosphorus pentoxide).<sup>152</sup> To date, there are a limited of studies on the use of P<sub>2</sub>O<sub>5</sub> as a *p*-type dopant for ZnO.

Some of the more referenced investigations which report *p*-type doping in ZnO, may actually be reporting effects associated with competing phase formation. Looking at the phase diagram for Zn-P and the phase diagram for ZnO-P<sub>2</sub>O<sub>5</sub> (Figs. 32 and 33), it is clear that it is possible to form other phases such as Zn<sub>3</sub>P<sub>2</sub> and Zn-phosphates. Zn<sub>3</sub>P<sub>2</sub> and ZnP<sub>2</sub> are *p*-type semiconductors.

For example, in one study, high percentages of phosphorus doping—3% at. wt.<sup>153</sup> were used with the intent to drive *p*-type doping of ZnO with such a high percentage of dopant material. Such a high percentage leaves open the possibility the *p*-type behavior arises from a competing phase, such as Zn<sub>3</sub>P<sub>2</sub>, especially because the initial doping source was Zn<sub>3</sub>P<sub>2</sub>. The group did not conduct any follow-up studies to distinguish *p*-type behavior in ZnO from *p*-type behavior from competitive phases such as Zn<sub>3</sub>P<sub>2</sub>. For example, a simple *p-n* junction would help determine if the source was from Zn<sub>3</sub>P<sub>2</sub> ( $E_{\text{gap}} \sim V_{\text{turn on}} \sim 1.62 \text{ eV}$ ) or from *p*-doped ZnO ( $E_{\text{gap}} \sim V_{\text{turn on}} > 3.5 \text{ eV}$ ).

A report of “anomalous” *n*-type conductivity was made for 5% wt. P<sub>2</sub>O<sub>5</sub> + 95% ZnO thin films deposited by RF sputtering<sup>154</sup>. From this work, the investigation concluded that P<sub>2</sub>O<sub>5</sub> was not suitable as a *p*-type dopant for ZnO. We note that the study utilized impure starting materials—ZnO purity = 99.99%, P<sub>2</sub>O<sub>5</sub> purity = 99.98%, so the nature behind the observed *n*-type conductivity may rest in the impure nature of the starting materials vs. the actual behavior of phosphorus in the lattice.

### ***6.1.2 Single Crystal Doping***

In addition to thin films, we observed that at the time of this effort and also at the time of writing this dissertation, there were no reports of planar doping of ZnO using phosphorus.

## **6.2 P<sub>2</sub>O<sub>5</sub> as a Dopant Material**

### ***6.2.1 Basic Properties***

P<sub>2</sub>O<sub>5</sub> is orthorhombic with a sublimation point of T<sub>sub</sub>= 350°C at atmospheric pressure. Its phase diagrams for ZnO-P<sub>2</sub>O<sub>5</sub> and Zn-P<sub>2</sub>O<sub>5</sub> are shown in Figs. 34 and 35, respectively.

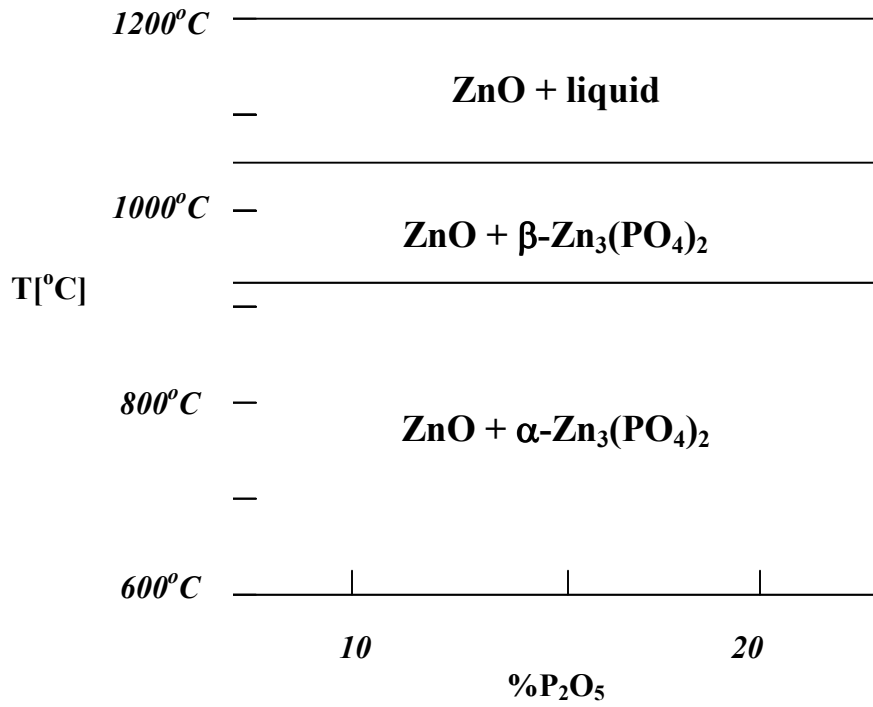


Figure 34 ZnO-P<sub>2</sub>O<sub>5</sub> phase diagram. Adapted from Reference 155

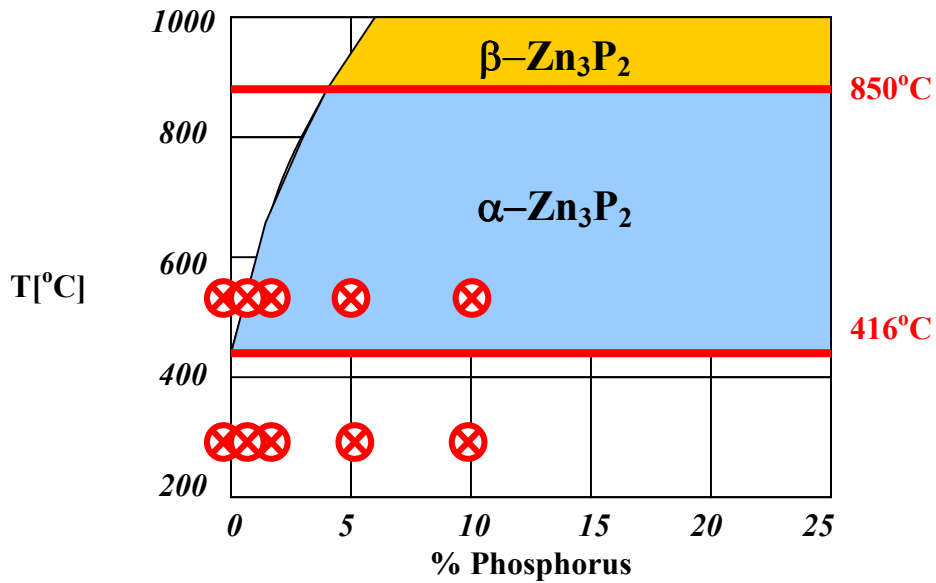


Figure 35 ZnO-Phosphorus phase diagram. Adapted from<sup>156</sup> Of the T<sub>dep</sub> studied in the thin film section, those on the phase diagram are labeled with ⊗

## **6.3 Phosphorus-Doped Thin Film Deposition**

### ***6.3.1 Background***

*Strain Associated with Extrinsic Defects (Dopant):* The size of the dopant-host element bond and the size of the dopant itself, relative to the host atoms, contribute to the strain on the resulting lattice.

In ZnO, the Zn-O bond length is 1.93 Å, while the P-O nearest neighbor separation in P<sub>2</sub>O<sub>5</sub> is 2.18 Å<sup>157</sup>. If we assume that phosphorus bonds into the ZnO lattice with the same coordination as it does in P<sub>2</sub>O<sub>5</sub>, then unless the lattice responds and changes size in response to dopant introduction, the 0.25 Å difference in bond length may induce local tensile strain around impurities.

In addition, the phosphorus atom has an ionic radius of 2.12 Å. This is significantly larger than the 1.38 Å ionic radius of oxygen and may magnify effects of tensile strain in the lattice.

Such large differences between the bond lengths of the dopant and host dopant as well as between radii of the host atoms and dopant atoms can induce large lattice strains around the impurity, should the impurity dissolve in the host lattice.

*Deposition Conditions:* All films were grown under the same conditions as the undoped films, as discussed in Chapter 4. Due to the low sublimation point of the dopant source, P<sub>2</sub>O<sub>5</sub>, it was necessary to periodically check that the stoichiometry of the as-deposited films did not vary significantly from the target stoichiometry. From run to

run, RBS confirmed no significant deviations of the film stoichiometry from the target stoichiometry.

### **6.3.2 Growth Parameter Influence on Structural Properties of P-Doped Films**

The crystallinity of the phosphorus-doped films improves with increasing  $T_{\text{dep}}$  for all phosphorus-doped samples, independent of whether the atmosphere was oxygen- or argon-rich (Fig. 34 (a), (b)).

We found that adding as low as 1% at. wt. P resulted in a broadening of the FWHM. As that percentage increased, the ZnO thin film amorphized, even at elevated  $T_{\text{dep}}$ , where near epitaxial behavior was observed for undoped ZnO and the  $T_{\text{sub}}$  of  $\text{P}_2\text{O}_5$  is exceeded.

Above  $T_{\text{dep}} = 250^\circ\text{C}$ , the FWHM saturated for all %P dopings and independent of the deposition atmosphere, indicating that at a given %P doping, the lattice structure reached a limit for the possible degree of crystalline ordering.

Rutherford backscattering data showed little variation in the % P concentration in films grown at low  $T_{\text{dep}}$  vs. films grown at high  $T_{\text{dep}}$ , for a given starting % P in the target. This indicated that in the case of a starting source like  $\text{P}_2\text{O}_5$ , with its low sublimation point, rf sputter deposition did not result in any significant loss of dopant, even for films grown at  $T_{\text{dep}} > T_{\text{sub}} (\text{P}_2\text{O}_5)$ .

### **6.3.3 Relationship between Strain and Optical Properties**

Strain along the  $c$ -axis ( $\epsilon_{zz}$ ) was examined as a function of deposition temperature,  $T_{\text{dep}}$ , for both argon-rich and oxygen-rich deposition conditions and as a function of % at. wt. phosphorus (Fig. 35 (a), (b)).

Films grown in both argon- and oxygen-rich atmospheres show tensile strain over the full range of  $T_{\text{dep}}$ . The strain approaches zero for films deposited at higher temperatures. The fact that the strain is primarily tensile in nature for this range of deposition temperatures is consistent with existing work on undoped ZnO thin films<sup>158</sup>.

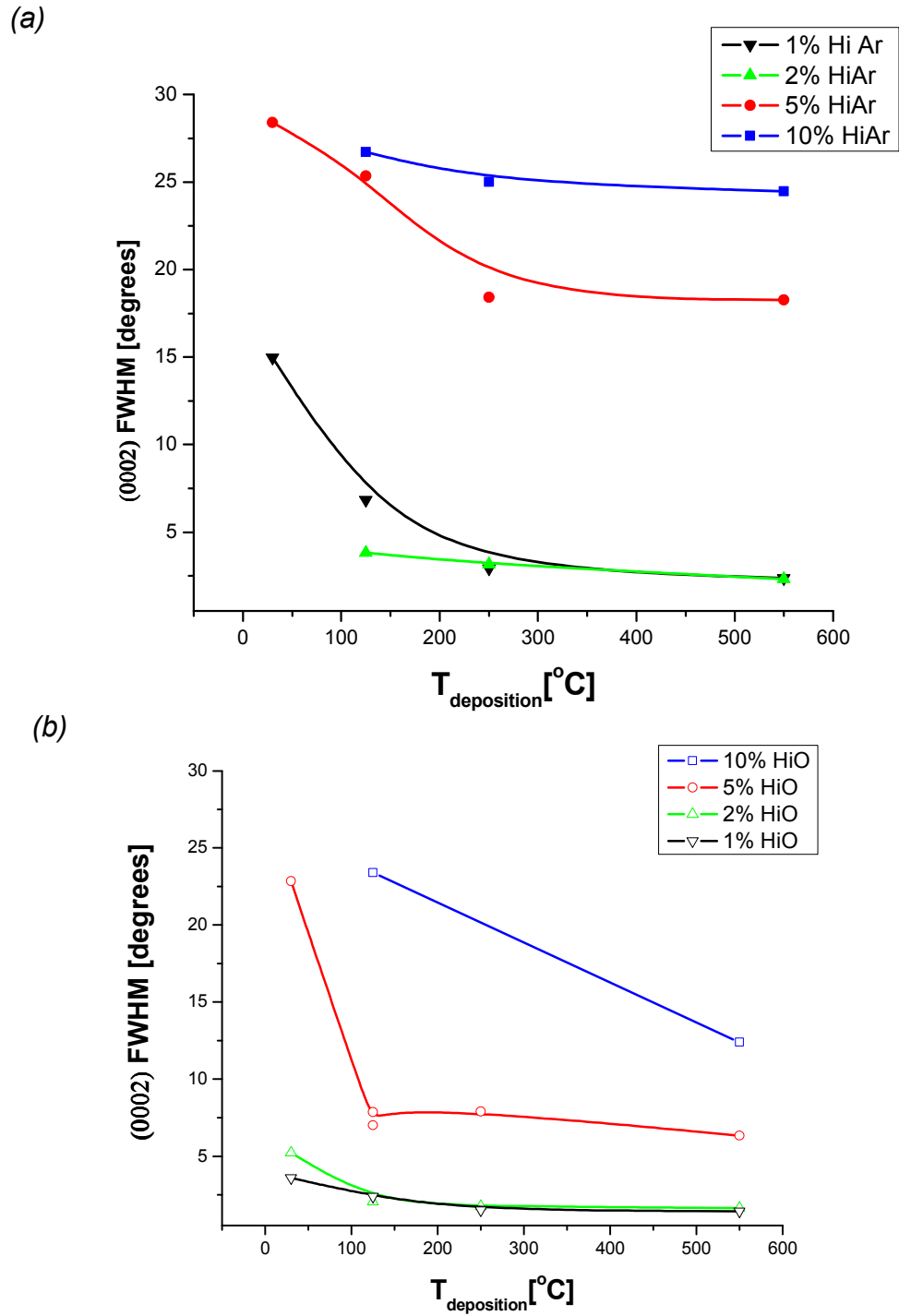


Figure 36 (0002) FWHM vs.  $T_{\text{deposition}}$  for Phosphorus-doped ZnO thin films (% Phosphorus = 1, 2, 5, 10% at. wt.) grown in an (a) an argon-rich atmosphere (b) oxygen-rich atmosphere.

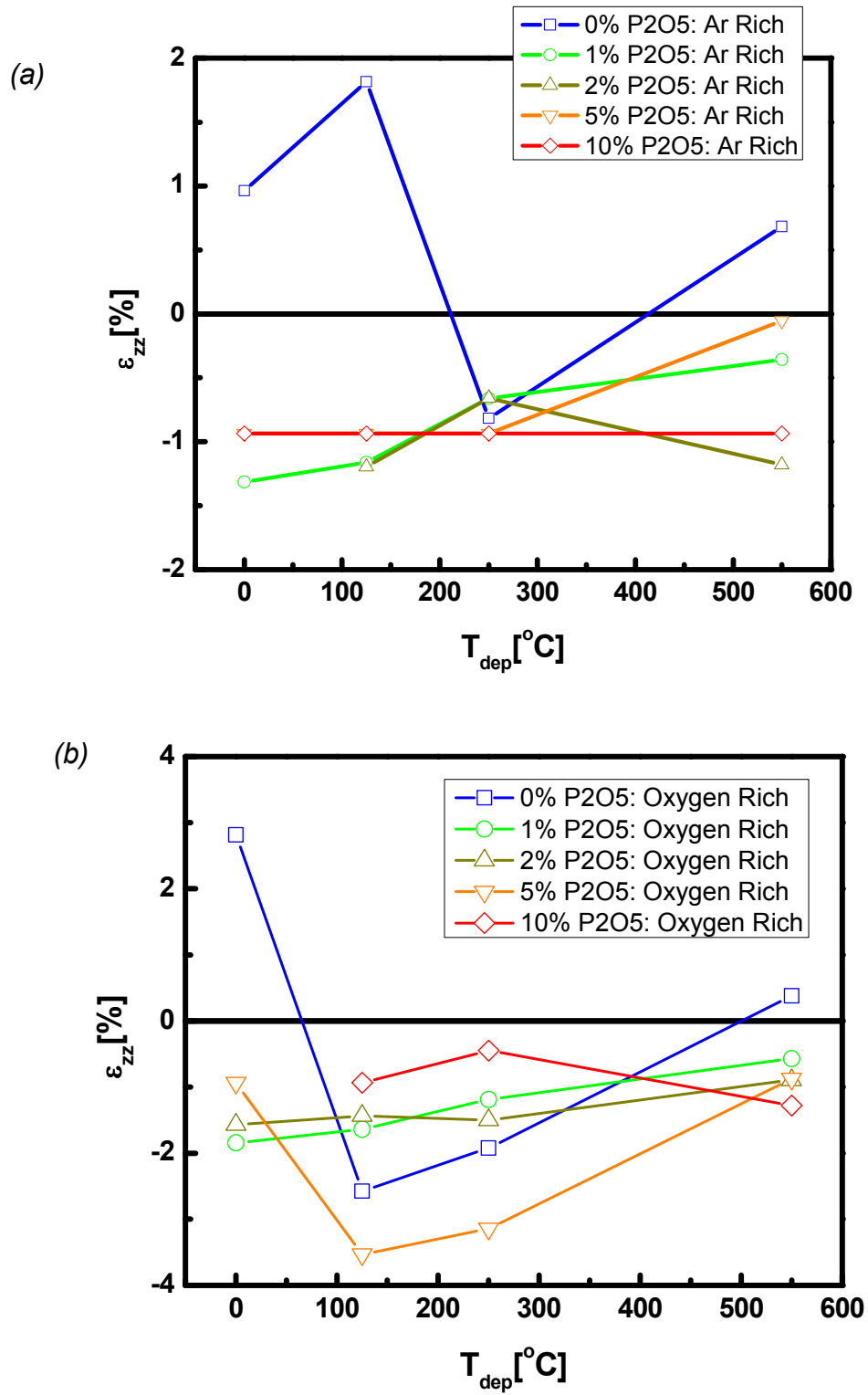


Figure 37  $\epsilon_{zz}$  vs.  $T_{deposition}$  for Phosphorus-doped ZnO thin films (% Phosphorus = 1, 2, 5, 10% at. wt.) grown in an (a) argon-rich atmosphere or (b) an oxygen-rich atmosphere.

$E_{gap}$  decreases for both 1 and 2 % Phosphorus doped films, but increases for both 5 and 10 % dopings. Looking at the compositional dependences of  $E_{gap}$  of the argon-rich and oxygen-rich films grown at the full range of  $T_{dep}$  (Figs. 36 (a), (b)), we found a non-linear compositional dependence at low dopings (<5%) and a linear dependence at higher dopings (5, 10 %).

Three main features can be commonly observed in semiconductors at the heavily doped limit:

1. *Formation of an alloyed phase*
2. *Band gap shrinkage*
3. *Band tailing*

1. *Formation of an alloyed phase*

Semiconductors that are alloyed to form a novel semiconducting material typically exhibit an optical band gap that is a compositionally-dependent superposition of the two parent compounds, that is:

$$E_{gap}(product) = x E_{gap}(compound 1) + (1 - x)E_{gap}(compound 2) \quad (6.1)$$

Where  $x$  is the fractional composition of compound 1. This is known as Vegard's Law<sup>159</sup>. Strictly speaking, it is a relationship involving the lattice constants rather than the energy gap.

If we assumed that Vegard's law held and calculated the band gaps for the alloyed compositions, we would obtain  $E_{\text{gap}} = 3.38 \text{ eV}$  for the 1%-doped case and  $E_{\text{gap}} = 3.39 \text{ eV}$  for the 2 % case, an overall increase in the band gap, in the opposite direction of what we measured.

Hence, either another compound or phosphorus alone is being incorporated into the ZnO thin film. If one imagines a scenario where  $\text{Zn}_3\text{P}_2$  ( $E_g = 1.3 \text{ eV}$ ) is being incorporated, this still leads to an increase in the band gap of the total compound relative to ZnO.

Furthermore, while there are versions of Vegard's Law that introduce correction terms, resulting in a relationship that deviates slightly from linearity (associated with band gap bowing)<sup>160</sup>, these correction terms are typically small (meV).

## 2. *Band gap shrinkage*

As the concentration of impurities increases, impurity levels merge to form impurity bands. When a large number of holes are introduced into the valence band (equivalently a large number of holes is introduced into the conduction band), hole-hole (electron-electron) interactions result from the overlapping of wavefunctions. The hole-hole (or electron-electron) interaction is composed of two terms: a Coulombic term and an exchange interaction. The exchange interaction arises from Pauli exclusion, which, in keeping holes (electrons) away from one another lowers the overall energy of the system. This is manifest as a shrinkage of the band gap.

Many semiconductors in the heavily doped limit exhibit band shrinkage. For example, GaAs shows shrinkage of approximately 16 meV. Such a small shrinkage cannot explain the observed magnitude of the change in the band gap.

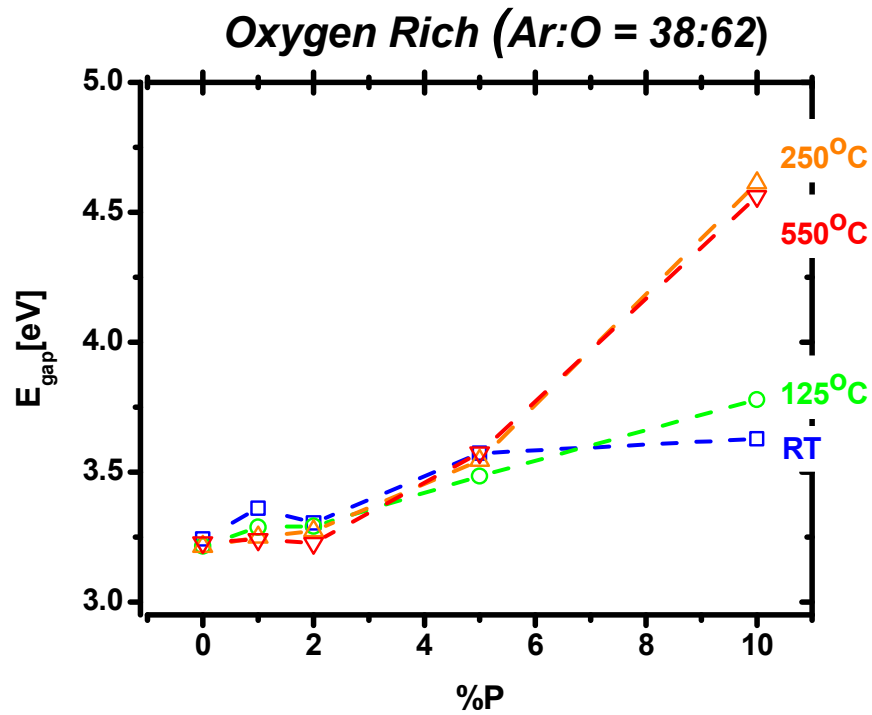
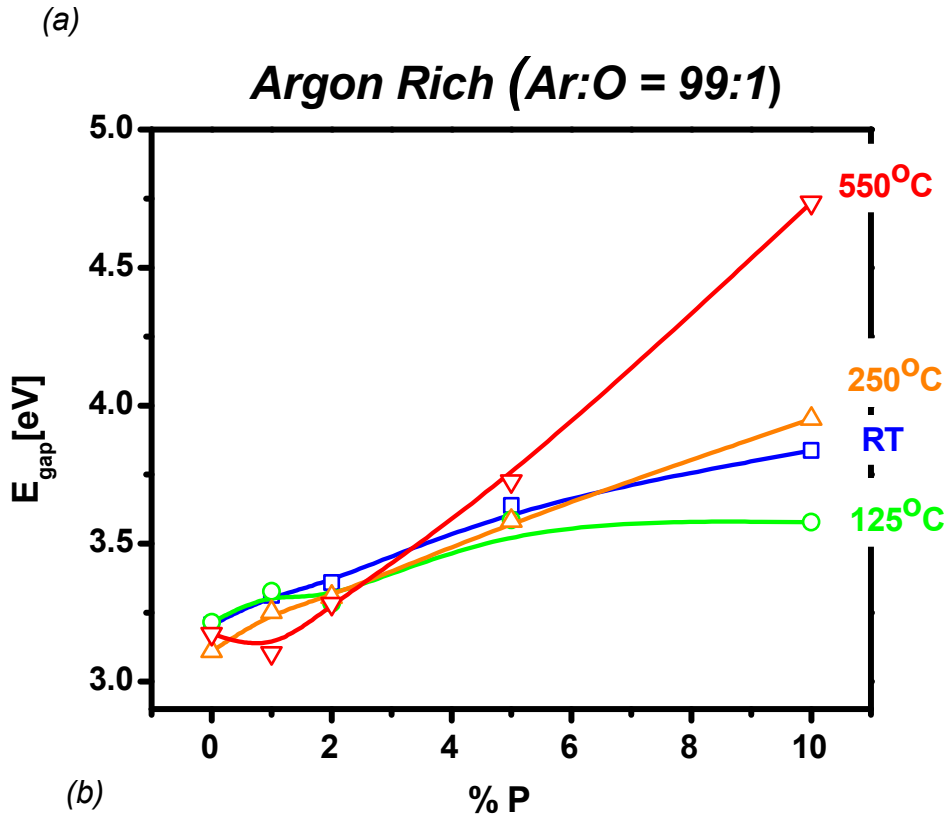


Figure 38  $E_{\text{gap}}$  as a function of % phosphorus (RBS) for oxygen-rich grown samples (top) and argon-rich grown samples (bottom)

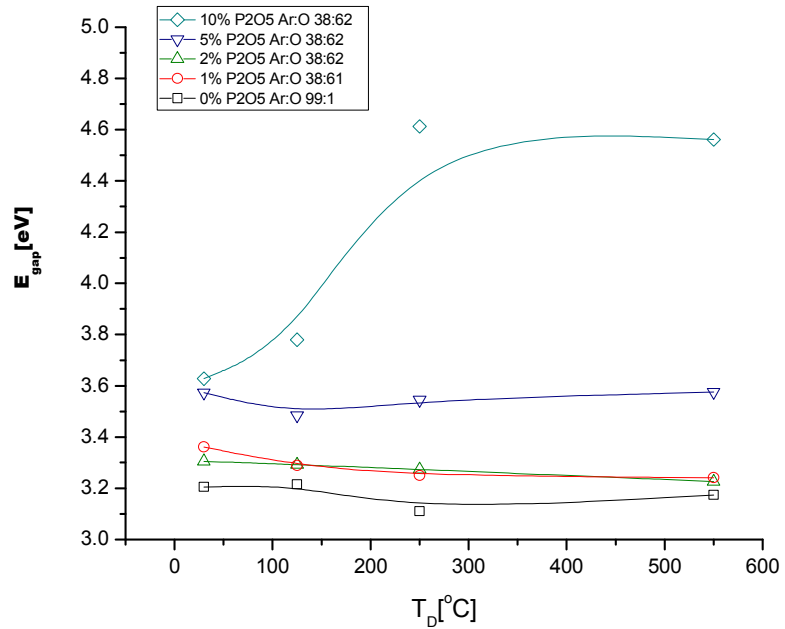
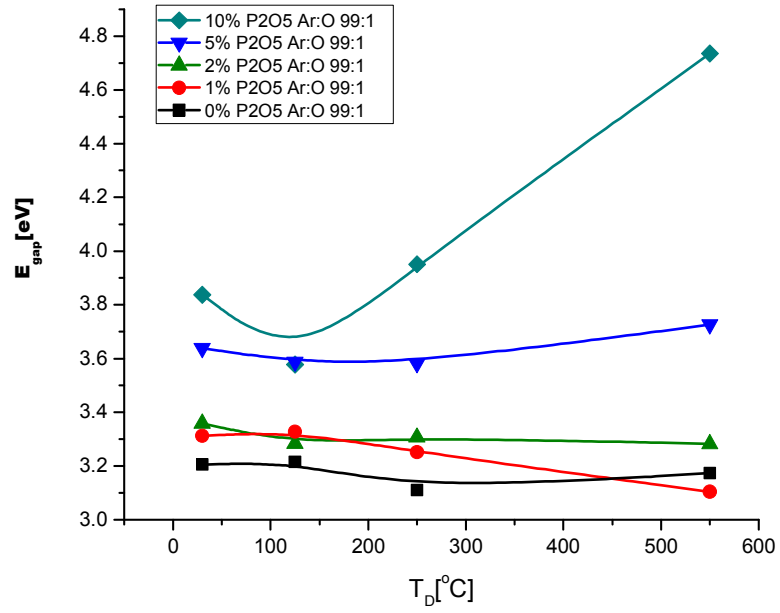


Figure 39

$E_{\text{gap}}$  vs.  $T_{\text{deposition}}$  for Phosphorus-doped ZnO thin films (% Phosphorus = 1, 2, 5, 10% at. wt.) grown in an argon-rich atmosphere (top) or an oxygen-rich atmosphere (bottom).

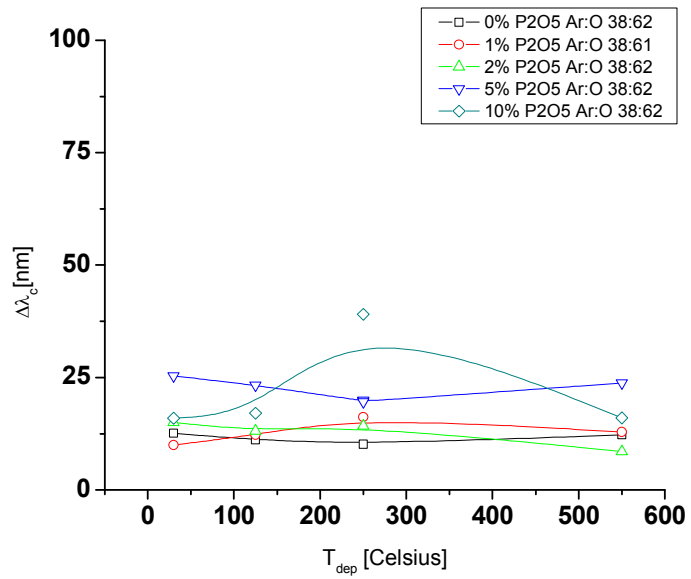
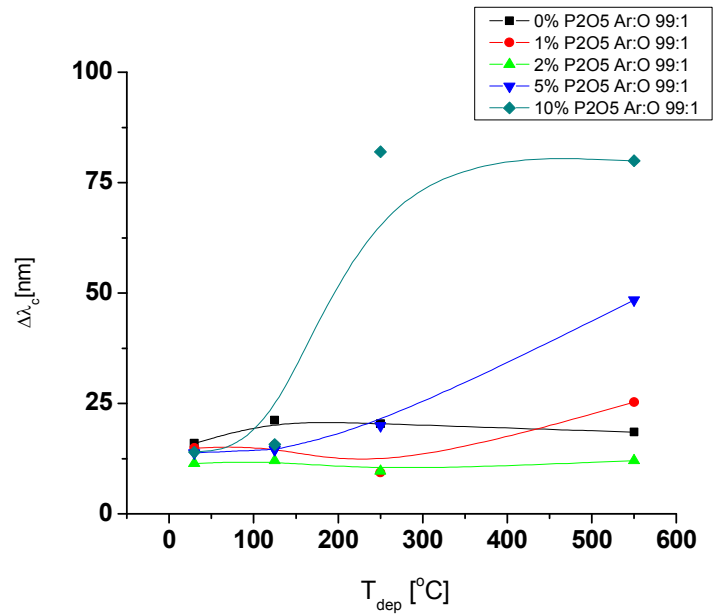


Figure 40  $\Delta\lambda$  vs.  $T_{\text{deposition}}$  for various % P doped films grown under Ar-rich deposition conditions (top) and Oxygen-rich deposition conditions (bottom)

### 3. *Band Tailing*

At the band edge, in the high impurity concentration limit, impurity atoms may become disordered on the host lattice. This leads to an overall broadening of the transition width, as the tail of the transmission spectrum contains extra states. The doping dependence of  $\Delta\lambda$  is presented in Fig. 40.

#### **6.3.4 *Electrical Properties***

Films doped at 5, 10% showed resistances in the  $G\Omega$  range, consistent with the formation of a glassy, insulating material, likely an alloy of ZnO- $P_2O_5$ . Room temperature carrier concentration measurements were attempted, but due to the inconsistency of the sign of the carriers, attributed to the noise of the signal, it was not possible to determine the carrier concentrations of these samples. *p*-type behavior was observed in p-n junctions fabricated from these highly doped samples, though not consistently.

## **6.4 Planar Doping of $P_2O_5$ into ZnO Single Crystals**

Single crystal ZnO samples were planar doped in air via annealing in a conventional annealing furnace. Freshly cleaned and etched crystal surfaces were dusted with  $P_2O_5$  powder and set to anneal in an alumina boat for a range of times and temperatures in air. Ramp up and down rates were set to a constant  $40^\circ\text{C}/\text{min}$ .

Table 7 shows a selection of annealed and planar-doped crystals. Carrier concentration was measured via four-contact Hall measurements at a range of

temperatures, up to 200°C, under dark conditions. Corner contacts were made in Van der Pauw geometry (corner contacts) and the Van der Pauw test method<sup>161</sup>, as outlined by the ASTM<sup>162</sup> and associated revisions<sup>163</sup> was followed. Au contacts were made, followed by In solder connections to Au wires<sup>164</sup>.

We found that of the annealing conditions tested (100°C, 400°C, 800°C; for durations of 1, 5, and 12 hours), we found that annealing an untreated crystal at 800°C for 12 hours consistently produced a *p*-type doped crystal with reasonable mobility and carrier concentration (Table 7).

The fact that the carrier type is *n*-type for samples annealed at 800°C, 1 hour is indicative of an improved *n*-type quality with minimal diffusion of P<sub>2</sub>O<sub>5</sub> into the lattice. The same process was repeated a year later in a common furnace and yielded *p*-type crystals of equal quality.

The measured electron concentrations and mobilities that we found are at par with reported measurements on single crystals (180 cm<sup>2</sup>/(V-s))<sup>165</sup>

The hole mobilities reported here are higher than the hole mobilities reported for *p*-type doping efforts of Group V elements into ZnO. There have been reports of hole mobilities as high as 40 cm<sup>2</sup>/(V-s) in phosphorous-doped ZnO thin films<sup>166</sup>. Other groups have reported the following hole mobilities for specific dopants<sup>167</sup>: Sb: 20 cm<sup>2</sup>/(V-s); N: 12-20 cm<sup>2</sup>/(V-s); O (native defect tailoring): 23 cm<sup>2</sup>/(V-s). The difference between the hole mobilities reported in the literature and those reported here may be associated with the fact that the values reported in the literature are for doped thin films, which may have a larger defect density than the single crystals employed in this effort, which may impede hole mobility.

**Table 7: Comparison of Undoped and P<sub>2</sub>O<sub>5</sub>-planar doped ZnO transport properties.**

	<b>Undoped ZnO</b> <i>800°C, 1 hour</i>	<b>Planar Doped</b> <i>400°C, 12 hrs</i>	<b>Planar Doped</b> <i>800°C, 1 hour</i>	<b>Planar Doped</b> <i>800°C, 12 hours</i>
Carrier Type	<i>n-type</i>	<i>indeterminate</i>	<i>n-type</i>	<i>p-type</i>
Mobility [cm <sup>2</sup> /(V-s)]	199	<i>indeterminate</i>	234	64
Carrier Concentration [cm <sup>-3</sup> ]	1.52 10 <sup>16</sup>	<i>indeterminate</i>	1.58 10 <sup>16</sup>	1.87 10 <sup>16</sup>

*p-n* junctions were fabricated using the 12 hour annealed samples. Au contacts were used as the contact on the *p*-type face of the crystal. In was used as the contact on the *n*-type fact of the crystal. *n*- and *p*-type contacts were simultaneously annealed at 600°C for 25 minutes in air via direct conduction (hotplate). A schematic of the device geometry is shown in Figure 41.

I-V characteristics for these junctions are shown in Fig. 42. Samples were measured above room temperature (80-100°C). Rectification was observed, with V<sub>turn on</sub> ~3.3 V. This is close to the value of the band gap for ZnO, indicating a *p-n* response for the contacts (vs. a Schottky response, as compared in Fig. 42 (a)).

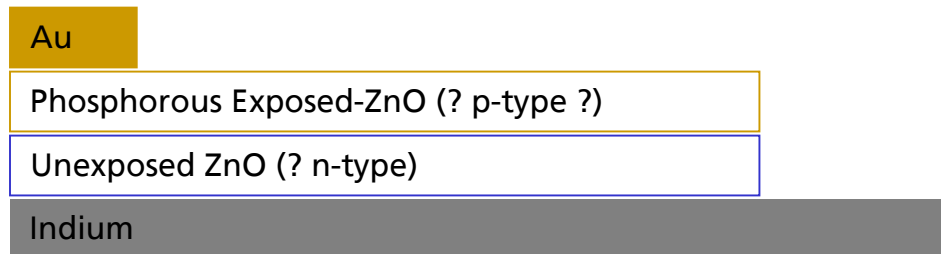


Figure 41 Device geometry of planar-doped *p-n* junctions

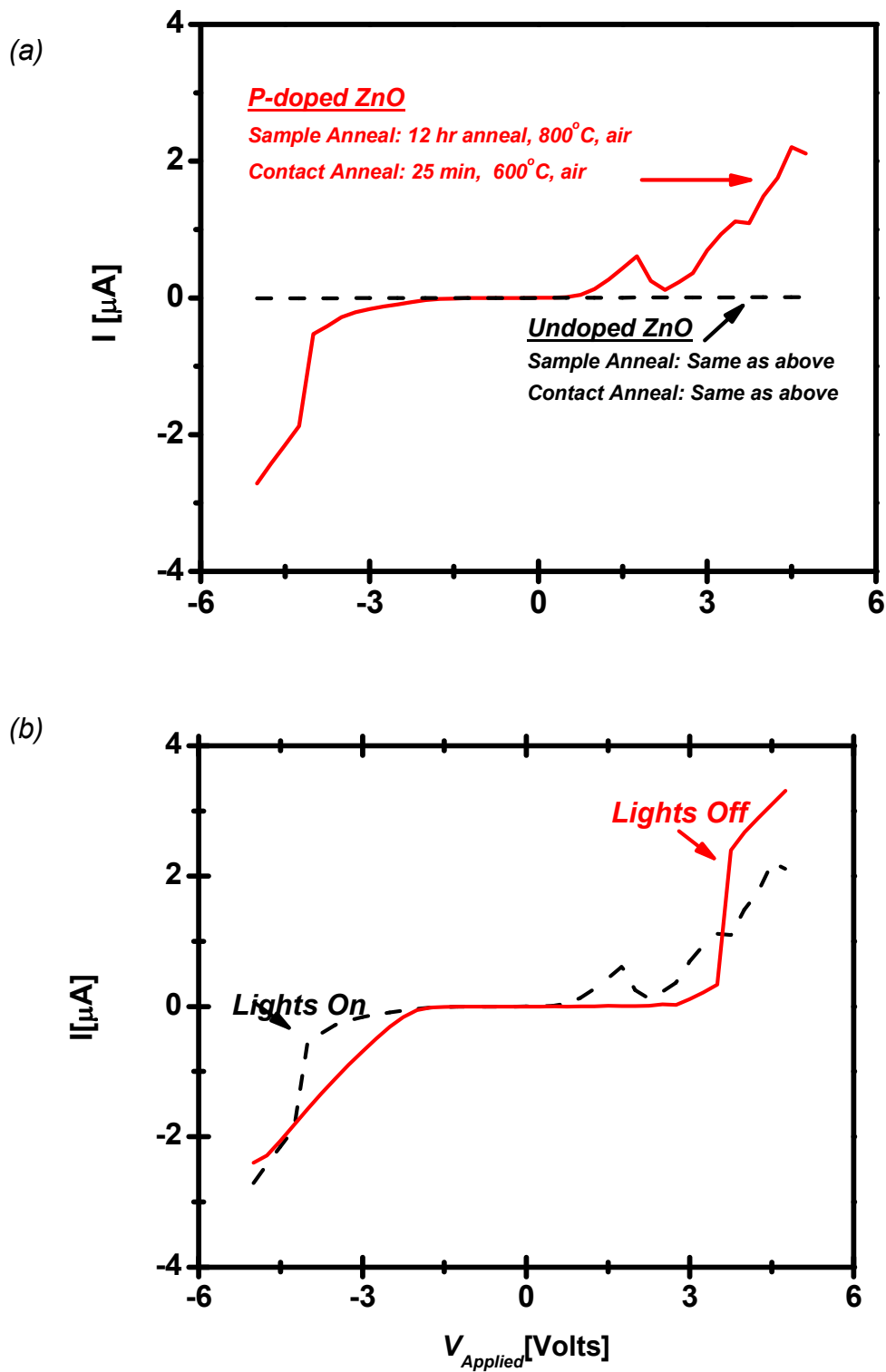


Figure 42 (a) Comparison of I-V Characteristics of undoped ZnO and phosphorus-doped ZnO, both prepared by heating in air at  $800^\circ\text{C}$  for 12 hours, followed by contact deposition (described in the text) and subsequent anneal at  $600^\circ\text{C}$ , 25 min. (b) I-V Characteristics of p-doped ZnO with room lights on (solid, red) and off (dashed, black)

The junctions are responsive to light (Fig. 42 (b)). I-V characteristics show several peaked structures.

In addition to  $P_2O_5$ , other phosphate compounds were tested for their viability as planar doping components—both in direct contact and spin-coated using distilled water. The phosphate compound ( $NH_4H_2PO_4$ ) under a range of annealing times and temperatures yielded samples whose conductivity type and carrier concentration proved difficult to measure due to the high resistance of the samples ( $>100\text{ G}\Omega$ ).

# Chapter 7: Implications for Unipolar and Bipolar Device Fabrication

## 7.1 Unipolar Devices

Single crystal results presented in Chapter 5 show that the best Schottky devices, with the lowest barrier heights are from samples annealed at  $T_{\text{Anneal}} \geq 600^{\circ}\text{C}$ . Of the three atmospheres studied in this work, the air-annealed samples produced reliable, low-barrier devices.

Samples annealed in air at  $1000^{\circ}\text{C}$  had the lowest Schottky barrier overall. These samples possessed clean surfaces with, as XPS has shown, a high concentration of oxygen, which likely improves the quality of the contact between the Schottky metal and semiconductor. Single crystals annealed between  $400 - 800^{\circ}\text{C}$  are oxygen-deficient and Zn-rich. Thus, the fabrication of unipolar devices under these conditions may prove to be less effective at surfaces prepared in this temperature range.

Argon and vacuum atmospheres produced samples with higher Schottky barriers that were at par with the existing barrier heights, as found in the literature. For argon-annealed samples, the lowest barrier was found in samples annealed at  $600^{\circ}\text{C}$ , while in vacuum annealed samples, the lowest barrier was found for samples annealed at  $200^{\circ}\text{C}$ . Surfaces for samples prepared at these temperatures showed minima in roughness for the temperature range studied. Further work to explore the pressure dimension of this parameter space is required in order to fully eke out effects associated with the vapor pressure of Zn and the rendering of a Zn-deficient (read: oxygen-rich) surface.

## **7.2 Bipolar Devices**

### ***7.2.1 Updating the Experimental Limits of the Failure to Dope Rule***

The failure to dope rule, as introduced in Subsection 2.2.4, is one of the most commonly invoked rules cited to explain the difficulties in  $p$ -type doping of ZnO. Since the initial announcements of  $p$ -type ZnO, these calculations have not been updated. Using our results, we update the failure to dope rule in this section.

As shown in Section 6.5, we found that  $p$ -type doped ZnO films and single crystals have carrier concentrations  $\sim 10^{16} \text{ cm}^{-3}$ . Given this, we re-calculated the position of the  $E_{Fermi,Experimental}^{(pin,p)}$ , as introduced in Section 1.3, so as to better represent the known limits for  $p$ -type doping ZnO.

We began by refreshing our memory of Eqn. 1.6, which we write here only in terms of the relevant  $p$ -type term:

$$N^p [T, E_{Fermi,Experimental}^{(pin,p)}] = \frac{1}{2\pi^2} [2m_p^*]^3 / 2 \int_0^\infty \frac{E^{1/2}}{[\exp(\beta(E - E_{Fermi,Experimental}^{(pin,p)})) + 1]} dE \quad (7.1)$$

In order to obtain a solution for  $E_{Fermi,Experimental}^{(pin,p)}$ , it was necessary to invert Eqn. 1.6. Rather than solve it analytically, we looked at the applicability of one of two existing approximations for the Fermi-Dirac distribution:<sup>168</sup>:

- Non-degenerate approximation
- Degenerate approximation

These approximations are used for solving the Fermi-Dirac integral above.

The non-degenerate approximation is utilized in cases where  $E_{Fermi}$  is well-above ( $3k_B T$ ) the valence band edge. At room temperature, the non-degenerate approximation would hold if  $E_{Fermi,Experimental}^{(pin,p)}$  was 78 meV away from the conduction or valence band. The degenerate approximation is utilized in cases where  $E_{Fermi}$  is inside the valence band.

Since Zhang's initial  $E_{Fermi,Experimental}^{(pin,p)}$  was predicted to be far from the valence band maximum and since we have no indication that the Fermi level should appear inside the valence band, since the valence band maximum may be at an even lower value than depicted in Zhang's article<sup>169</sup> we took the non-degenerate approximation as a reasonable starting point. In this case, the Fermi function can be replaced by a simple Maxwell-Boltzmann-like exponential:

$$N^p [T, E_{Fermi,Experimental}^{(pin,p)}] = 2 \left( \frac{2\pi m^* k_B T}{h^2} \right)^{3/2} \exp \left[ \frac{(E_{Fermi,Experimental}^{(pin,p)} - E_{valence})}{k_B T} \right] \quad (7.2)$$

Where  $E_{valence}$  = the valence band maximum.

Eqn. 7.2 is re-written in terms of  $E_{Fermi,Experimental}^{(pin,p)}$  as Eqn. 7.3 and is consistent with the approach taken by Walukiewicz to address the doping asymmetry in semiconductors<sup>170</sup>:

$$E_{Fermi,Experimental}^{(pin,p)} = E_{valence} + k_B T \ln \left( \frac{n_{holes}}{N_V} \right) \quad (7.3)$$

Where  $N_v$  is:

$$N_v = 2 \left( \frac{2\pi m^* k_B T}{h^2} \right)^{3/2} \quad (7.4)$$

Substituting in the electron effective mass  $m^* = 0.59m_e$ <sup>171</sup> into Eqn. 7.4, we obtain  $N_v = 1.13 \times 10^{25} \text{ m}^{-3}$  at 300K. Inserting this into Eqn. 7.3, along with  $n_{hole} = 1.87 \times 10^{16} \text{ cm}^{-3}$  (from Table 7), we obtained  $E_{Fermi, Experimental}^{(pin,p)} = -0.34 \text{ eV}$ . At the time of writing, there were no known cyclotron resonance measurements of the hole effective mass for phosphorus-doped ZnO, thus the electron effective mass was used in this calculation. This value does not differ significantly from the hole effective mass measured by cyclotron resonance in undoped single crystals<sup>172</sup>.

This is significantly different from the value calculated in the original paper by Zhang, which assumed the absolute worst-case scenario (a negligible hole concentration not explicitly stated by the authors) for ZnO and placed  $E_{Fermi, Experimental}^{(pin,p)}$  far above the valence band maximum. If one assumes that a “negligible” carrier concentration is of the order  $10^{13} \text{ cm}^{-3}$ , one obtains the  $E_{Fermi, Experimental}^{(pin,p)}$  shown in Fig. 4  $\sim +0.5 \text{ eV}$ .

The recalculation of  $E_{Fermi, Experimental}^{(pin,p)}$  will assist in efforts to refine and improve conditions to grow *p*-type doped thin films as well as future efforts to develop thin film as well as single crystal devices.

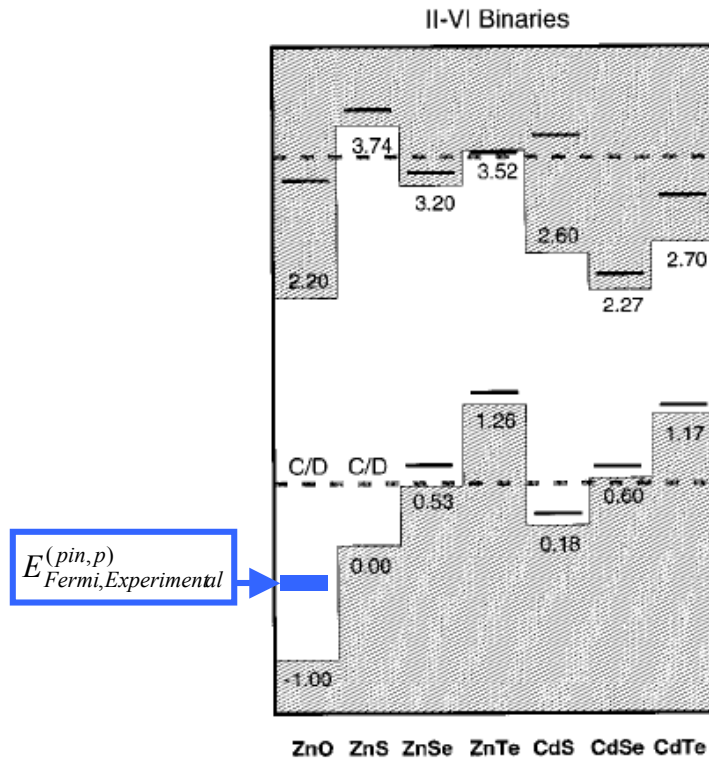


Figure 43 Modified band diagram from Figure 4. Modification schematically reflects a change of  $E_{Fermi,Experimental}^{(pin,p)}$  (thick solid line) value as recalculated in the text. Originally,  $E_{Fermi,Experimental}^{(pin,p)}$  appeared at the dashed line labeled “C/D”

### 7.2.2 Single Crystal Planar Doping Conditions

Surfaces were found to be Zn rich for samples annealed in air between 400 – 800°C. 800°C anneals may be ideal for planar doping if enough dopant can diffuse in—any Zn interstitials that existed in the near-surface/near-bulk region may have diffused out to the surface. Table 7 shows that a 12-hour anneal produces a reasonable mobility.

There may be a density of Zn vacancies that can support  $p$ -type conduction or at least a minimum in the concentration of Zn interstitials able to participate in extrinsic dopant compensation.

### ***7.2.3 Phosphorus-Doped Thin Film Growth Conditions***

The conditions that promote  $p$ -type conduction in thin films are less straightforward. This may be attributable to competing donor and acceptor states.

In both undoped and doped cases, the lattice strain is tensile and relaxes with increasing  $T_{\text{dep}}$ , except in the case of the 1% doped films grown in an argon-rich, which show an increase in tensile strain with increasing  $T_{\text{dep}}$ .

It is plausible that the larger tensile strain observed in 1% P-doped films supports formation of compensatory defects, such as oxygen vacancies, since a reduction in  $E_{\text{gap}}$  is observed with increasing strain along the (0002) direction, where we would expect, from theory involving effects of epitaxial strain alone, an increase in the band gap.

If compensatory defects are not to blame, strong lattice relaxation may be the source of the dopant energy level deep within the gap<sup>173</sup>, which would require device operation at temperatures greater than room temperature in order for ionization of carriers to occur.

An argon-rich atmosphere may set the stage for oxygen vacancies, since the source of oxygen in the film is limited to oxygen in the target and the limited oxygen ambient.

While it is true that the oxygen-rich ambient may not be a likely ambient to support oxygen vacancies in the film, the reduction in band gap suggests that the

resulting ZnO is not stoichiometric, possibly from the presence of excess Zn, which would sit as interstitials. If this is the case, then this deposition condition will not facilitate *p*-type doping, as Zn interstitials are a known source of *n*-type enrichment<sup>174</sup>.

## **Appendices**

## *Appendix 1: RF Sputter Deposition*

### **A1.1 Introduction to Sputter Deposition**

Sputter deposition is a method of thin-film deposition that occurs via ion bombardment of a target. Argon gas is ionized by a large applied electric field. The field gradient accelerates the argon gas ions towards a target. The accelerated ions bombard the target and via momentum transfer, cause knock-on collisions with target atoms near the surface. A fraction of the knocked-on target atoms move through several atomic layers before they are ejected. The ejected material then travels through the chamber space and condenses on the substrate surface. Depending upon  $T_{\text{dep}}$ , the condensed material has variable levels of mobility and interacts with other condensed atoms on the substrate surface.

Sputtering has an advantage over many other deposition techniques in that the transfer of material is typically stoichiometric. It tends to produce films with good adhesion strength, homogeneity in composition and uniformity of thickness.

Sputtering can occur using a DC power supply or an RF power supply. DC sputtering, which is commonly used to sputter metals, utilizes a DC voltage gradient between the target cathode and substrate anode to produce an accelerating voltage. DC sputtering has limited use for high-resistivity materials (some semiconductors and all insulators). The high negative potential applied to the insulating target leads to positive charge build up on the target surface and an eventual cessation of sputtering<sup>175</sup>. RF sputtering allows for the deposition of non-conductive materials.

Sputtering can occur in *reactive* or *non-reactive* modes. In reactive mode, the target is one source of elements and the ionized gas, which contains some amount of reactive gas (e.g. oxygen, ammonia, nitrogen) is the other source. For example, ZnO can be produced in reactive mode when a Zn metal target is sputtered in an oxygen atmosphere. In many cases of reactive sputtering, it is not known if the desired compound is formed (1) at the target surface and then transferred to the substrate; (2) in the plasma and then transferred to the substrate; (3) on the substrate surface.

## **A1.2 Experimental Details**

An RF Plasma Products RF5S RF generator operating at 13.56 MHz was used to generate the plasma and accelerate ions to the target. A 1" diameter target was bonded to a copper backing plate using thermally conductive silver epoxy. The backing plate was thermally coupled to a water-cooled face of the sputter gun using thermally conductive silver grease. Water-cooling serves to continuously dissipate heat associated with ion bombardment. Cooling is important, since excess heating of the target can drive changes in its stoichiometry.

Undoped ZnO targets were fabricated using 99.999% ZnO powder isostatically pressed to minimize void formation. Phosphorus-doped ZnO targets were fabricated using 99.999% P<sub>2</sub>O<sub>5</sub> powder mixed with 99.999% ZnO powder. To alleviate concerns for contamination from the Al<sub>2</sub>O<sub>3</sub> mortar and pestle (the conventional route for mixing during target fabrication), the powder mixture was placed in suspension with n-heptane solvent and was stirred using a Teflon-encased stir bar in a Pyrex beaker for 24 hours.

After the stirring period, the n-heptane was gently boiled off, ( $T_{\text{boil}} = 98^{\circ}\text{C}$ ). The dried powder was isostatically pressed at 10,000 psi into a target without use of binders such as polyvinyl alcohol, again, in order to minimize contamination. Targets were neither hot-pressed nor thermally sintered, so as to avoid loss of  $\text{P}_2\text{O}_5$  during the sintering process and to minimize native defect evolution, which can occur during conventional thermal processing of target materials.

All substrates underwent pre-cleaning using a three-solvent process. Substrates were placed in a Fluoroware chip boat and cleaned in pyrex beakers. Substrates were degreased in trichloroethylene for 10 minutes under ultrasonic agitation. A 5-minute ultrasonic acetone rinse followed. Finally, the substrates were ultrasonically cleaned in methanol for 10 minutes. Substrates were blown dry with pressurized  $\text{N}_2$ , immediately mounted to the substrate heater, and placed in the deposition chamber.

Substrates were mounted to a rotating substrate heater using silver paint. The rotating substrate heater was heated by four internally-mounted quartz lamps. These lamps were controlled using a Eurotherm PID controller, using a thermocouple that was electrically isolated and was screened from the RF source.

Prior to deposition, the chamber was pumped down to  $p < 1 \times 10^{-6}$  Torr. The chamber was baked out with heater tape the day before deposition occurs in order to drive off any potential sources of hydrogen. The chamber was quickly opened and the substrates (which have been cleaned using the procedure described below) were mounted. The chamber was pumped down using a diaphragm pump and single-stage turbo pump.

With the shutter in place, the target was pre-sputtered for 30 minutes prior to deposition in an oxygen-rich atmosphere. Pre-sputtering was conducted in order to:

- Clean the oxide target surface
- Equilibrate sputtering rates of the target's constituents (reproducibility)
- Coat the chamber walls so as to minimize contamination due to chamber outgassing during the deposition process.

The RF matching network was tuned to minimize reflected power and maximize forward power.

Prior to opening the shutter, the atmosphere was set to the standard deposition pressure and composition and an additional stage of pre-sputtering takes place for 30 more minutes. During this time, the substrate heater was set to its target temperature. The heater stage was set to rotate in order to insure compositional uniformity across the sample. Target to substrate distance was fixed at 6 cm for the depositions described in this investigation. Power was fixed at 100W. Once the two stages of pre-sputtering are complete, the shutter was lifted and the deposition process began.

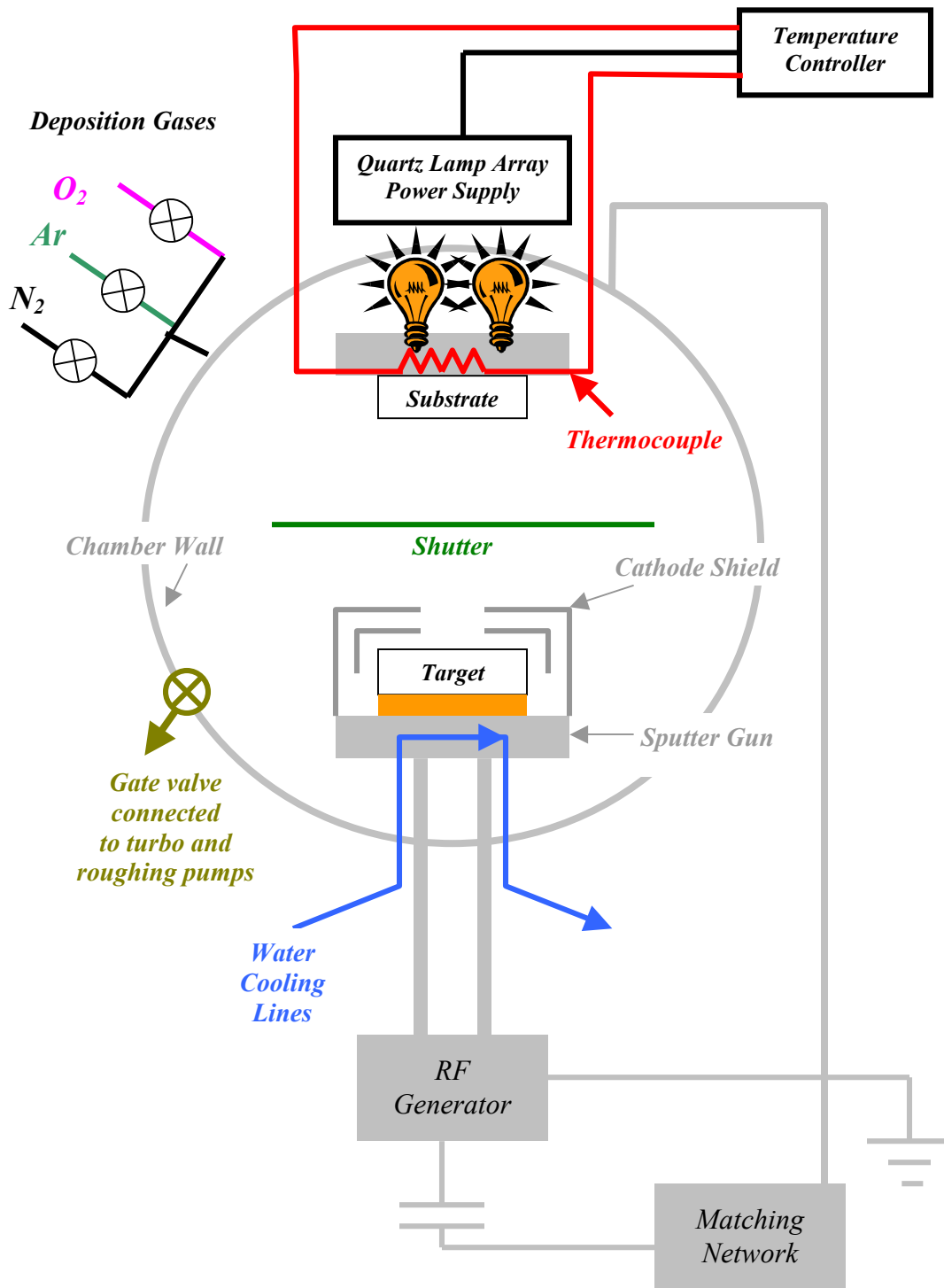


Figure 44 Top view schematic of rf sputter deposition chamber and associated electronics and gas handlers.

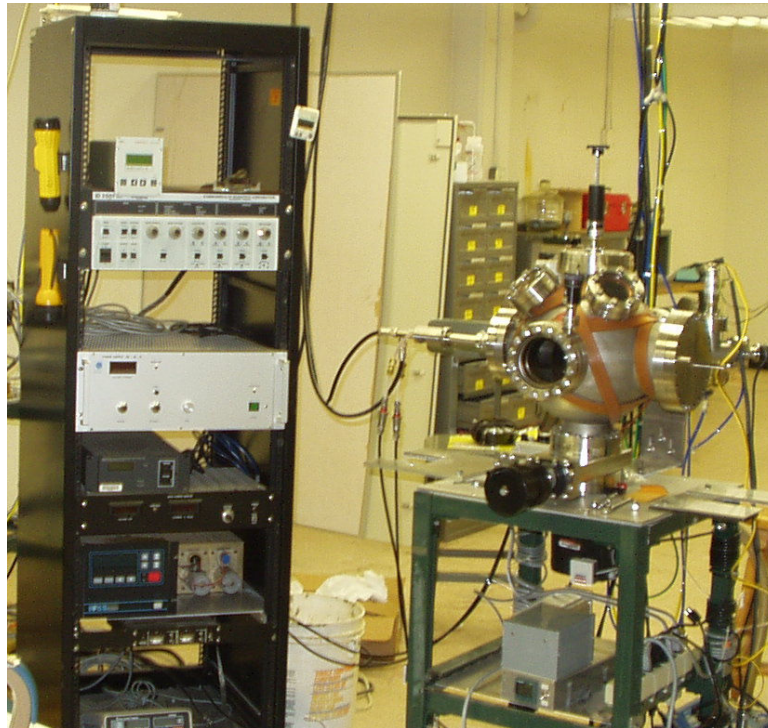


Figure 45      Photograph of rf sputter chamber and electronics rack

## Appendix 2: Atomic Force Microscopy

### **A2.1 Introduction**

Atomic Force Microscopy (AFM) is a common method of mapping surface morphology on the nanometer scale. In its simplest form, *contact mode*, a cantilever with a pointed tip is pressed against a sample surface with forces on the order of nanoNewtons. In order to keep the cantilever deflection (equivalently, the force applied) constant, the  $z$ -position of the cantilever is varied. The cantilever is scanned across the sample surface--( $x,y$ ) direction—yielding a map of  $z$ -direction across the surface.

A variation on contact mode, *tapping mode*, drives the cantilever at its mechanical resonance frequency and the tip is brought into close proximity to the sample surface, but is not in direct contact. Variations in the tip-sample interaction forces give rise to variations in the resonance frequency, affecting the amplitude of the cantilever's motion. Unlike contact mode, which is just sensitive to short-range tip-sample interactions (by virtue of it being in direct contact with the sample), tapping mode is sensitive to short- and longer-range forces.

### **A2.2 Experimental Details**

An SPM MultiMode system from Digital Instruments was operated in tapping mode at room temperature and atmosphere over (2 x 2) and (10 x 10)  $\mu\text{m}^2$  areas with a (512 x 512) resolution. Drive frequencies were on the order of 290 kHz. Roughness

measurements were obtained after looking at three regions that were spatially separated by at least 20  $\mu\text{m}$ , relative to the location of the initial measurement.

### A2.3 Analysis

Roughness was calculated over the full 2 x 2  $\mu\text{m}^2$  region of interest. Three different regions were scanned, separated by a distance 10  $\mu\text{m}$  or more. The root-mean-square (rms) average roughness of a surface is calculated over the entire area of interest,  $A$ , by integrating over  $r(x,y)$ , the roughness profile:

$$R_{rms} = \sqrt{\frac{1}{A} \int_0^2 \int_0^2 r^2(x,y) dy dx} \quad (\text{A2.1})$$

## **Appendix 3: UV Spectroscopy**

### **A3.1 Introduction**

ZnO is optically active material—if a photon has an  $E > E_{gap}$ , then it is possible to drive an electron from the valence band into the conduction band. Ultraviolet spectroscopy allows for such an event to take place by driving a semiconductor with photons of  $\lambda=400\text{-}200$  nm of the electromagnetic spectrum. Two approaches were used in this thesis: spectrophotometry—which varies the excitation wavelength and looks at the emitted response at that wavelength and luminescence which pumps a fixed wavelength in and looks at the emitted response.

### **A3.2 UV-Visible Spectrophotometry—Experimental Details & Analysis**

#### *Purpose*

UV-Visible Spectrophotometry is a technique that allows for the extraction of the optical properties of a material (reflectance, absorption and transmission) as well as the band gap of the material.

#### *Experimental Details*

A Shimadzu UV-2501PC commercial spectrophotometer was used to make transmission measurements at room temperature and ambient atmosphere. A schematic of the system in transmission mode is shown in the figure below. The system contains

two light sources: a conventional tungsten source, which illuminates the sample for measurement in the visible range down to the near-UV (800 – 360 nm); the second source is a deuterium (D<sub>2</sub>) lamp, which illuminates the sample in the UV (360 – 188 nm). A single photomultiplier tube serves as the detector across the ranges of both sources.

A standard source, such as an uncoated substrate, is placed in the standard arm of the spectrophotometer and the response of this is measured and subtracted from the thin film + substrate, which is placed in the measurement arm.

### *Analysis*

UV-Vis Spectrophotometry directly measures the percent transmission as a function of wavelength for a thin film relative to the underlying substrate. The cutoff wavelength,  $\lambda_c$ , is defined as the wavelength at which the transmission is at 50% of its value at 800 nm. Cutoff wavelength,  $\lambda_c$ , was extracted using Boltzmann fits to %T vs. wavelength data in the form:

$$\%T(\lambda) = \frac{T(\lambda_f) - T(\lambda_i)}{1 + e^{(\lambda - \lambda_c) / \Delta\lambda}} + T(\lambda_i). \quad (\text{A3.1})$$

Here,  $T(\lambda_f) = 188$  nm,  $T(\lambda_i) = 800$  nm and  $\lambda_c =$  cutoff wavelength,  $\Delta\lambda$  is the transition width.

This is converted to a band gap,  $E_{\text{gap}}$ , since  $E_{\text{gap}} = \frac{hc}{\lambda_c}$ . Here,  $h = 6.62 \times 10^{-34}$  J-s and  $c$  is the speed of light. This result is then converted from Joules into electron volts, using the conversion:  $1 \text{ eV} = 1.6 \times 10^{-19} \text{ J}$ .

This approach was selected over the typical approach by Pankove<sup>176</sup>, which converts transmission to an absorption coefficient and then attempts to fit a line to the

transition edge of the absorption curve. Pankove's approach involves qualitative "guess work" in defining the range to fit a line to the transition edge of the absorption curve, in order to determine the value of the band gap.

All measurements conducted in this dissertation were conducted between 800-200 nm, with an 0.2 nm step size and slit width = 0.2 nm. The sample aperture window was ~ 4 mm x 6 mm. The scan speed was set to a medium scan rate. Measurements were conducted relative to a blank sapphire substrate in the reference arm.

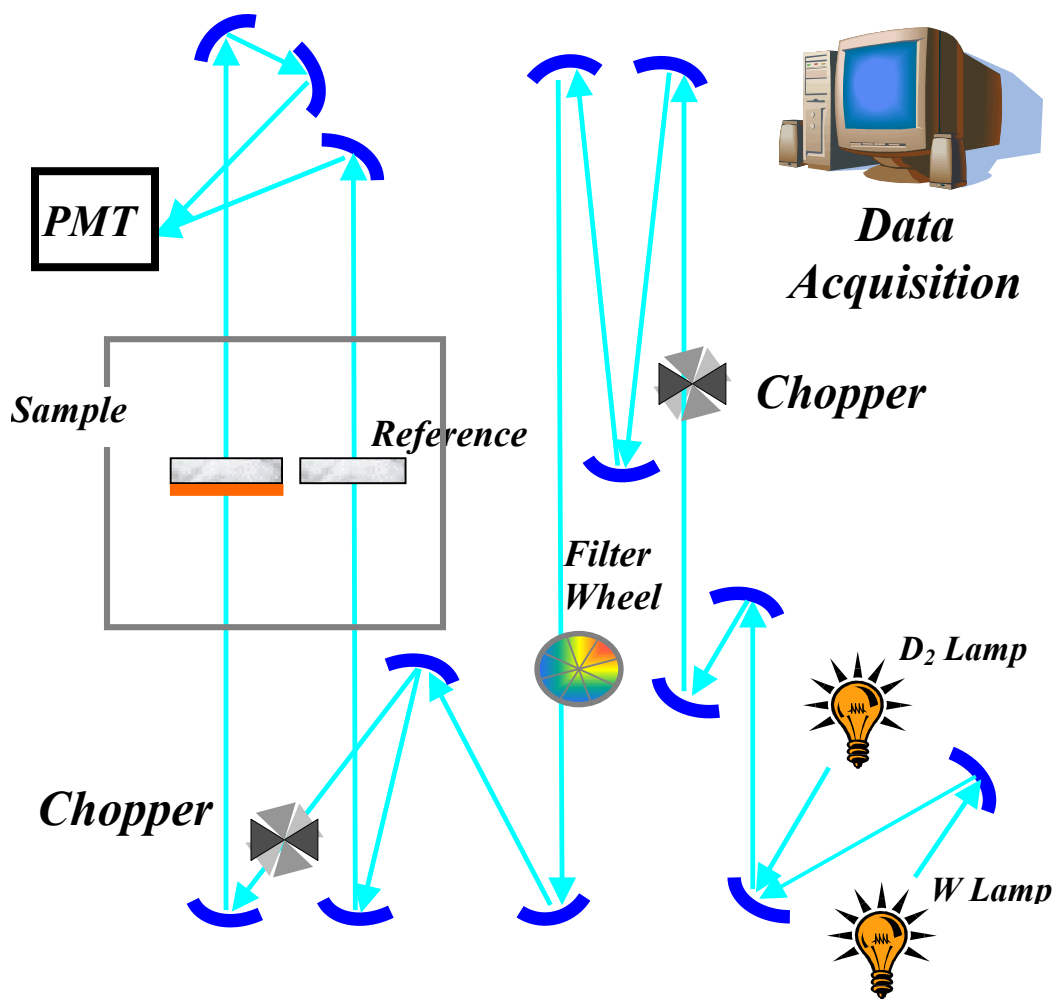


Figure 46 UV-Visible Spectroscopy, Transmission Mode. The beam path is indicated by the cyan arrows and the position of Reflectance Mode attachment is indicated by a gray box around the sample and reference. (Adapted from W. Yang, thesis)

### A3.3 Photoluminescence—Theory and Experimental Details

Photoluminescence spectroscopy (PL) is a non-destructive technique used for probing the electronic structure of materials. As the name suggests, photons with  $E > E_{\text{gap}}$  are directed onto a sample, which absorbs energy into the material. The excitation generates electron-hole pairs.

Eventually, these electron-hole pairs recombine. The recombination event may be accompanied by light whose wavelength is proportional to  $E_{\text{final}} - E_{\text{initial}}$ , known as a *radiative recombination* process. It is possible that some fraction of energy during the recombination event may not include the emission of light. This is known as a *non-radiative recombination* process.

PL was used for:

1. *Determination of  $E_{\text{gap}}$* : Very simply, the wavelength of the peak with the maximum intensity corresponds to the band gap.  $E_{\text{gap}} = h\nu_{\text{gap}}$ .
2. *Monitoring of crystalline quality*: Compressive and tensile strains effect band position. Crystalline quality, as observed in the XRD FWHM, affects peak widths. We discuss this in greater detail, as applicable, in the body of the dissertation.

#### *Experimental Details*

All measurements were conducted in reflection mode at room temperature using an  $\text{N}_2$  pulsed laser with  $\lambda = 337$  nm, set to the maximum repetition rate of 10 Hz. The

pulse width was  $< 4$  ns (FWHM). At 30 Hz, the average power was  $\sim 7.5$  mW. Prior to measurement, a GaN MOVPE-grown sample, 60 microns in thickness, was used to calibrate the intensity. The  $N_2$  peak position at 337 nm was used as the calibration point for the fiber optic spectrometer and was removed during normalization.

Data was collected using an Ocean Optics SD2000 fiber optic spectrometer. An optical fiber of 1000  $\mu\text{m}$  was used for the purposes of calculating the integrated intensity. The spectrograph was set to operate with a 25  $\mu\text{m}$  slit and a resolution of 0.6 nm in wavelength. The spectrometer was controlled with a PC1000 interface board, containing an A/D converter on an ISA bus card.

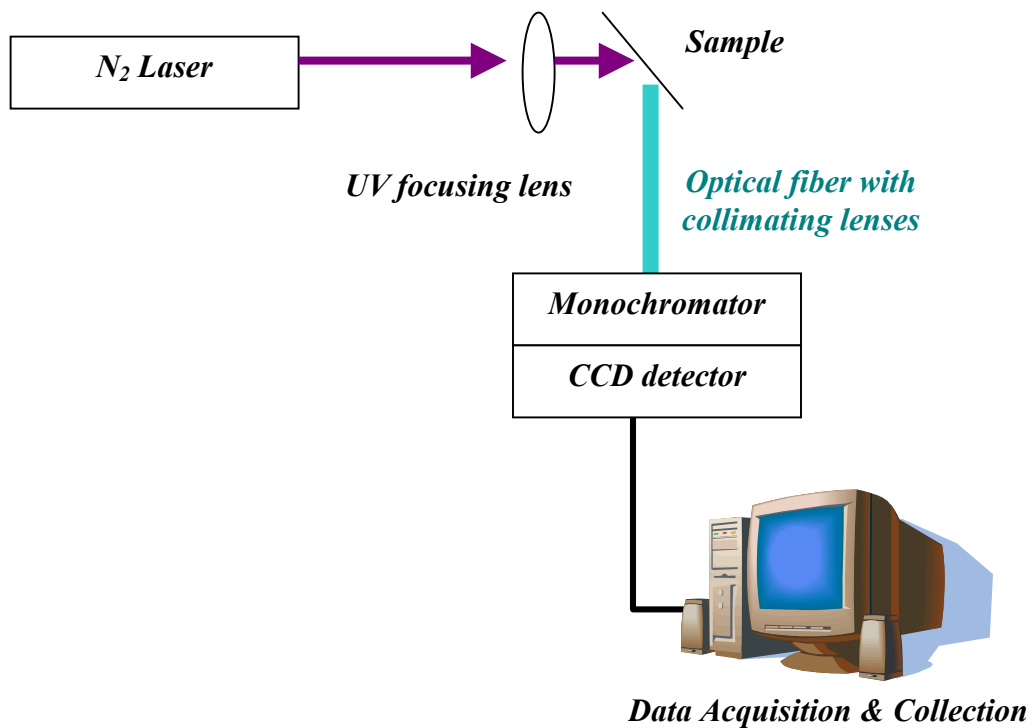


Figure 47 Top view schematic of PL system.

## **Appendix 4: Rutherford Backscattering Spectrometry and Channeling**

### **A4.1 Introduction**

Rutherford Backscattering Spectrometry is no more than a sophisticated version of Lord Ernest Rutherford's original 1911 experiment involving helium ions impacting a gold foil<sup>177</sup>.

A collimated monoenergetic beam of  $\alpha$ -particles ( ${}^4\text{He}^+$ ) with a spot size of approximately 1 mm in diameter and  $0.01^\circ$  divergence is generated with an accelerator source. The beam is directed towards the sample under investigation using magnetic steering mechanism. Upon reaching the sample, the individual  $\alpha$ -particles have several possible paths of interaction: they may interact with the near-surface region of the sample by elastically scattering off of surface atoms or by entering the sample, scattering within some depth of the sample, losing energy along the way and backscattering out into an annular barrier detector. The energy of the backscattered  $\alpha$ -particle is proportional to the atomic mass (Eqn. A4.1). The result is an energy spectrum of the backscattered  $\alpha$ -particles as a function of energy (or in terms of the detector's channel numbers, which are directly proportional to the backscattered energy). A schematic is depicted in Figure 48.

Rutherford Backscattering Spectrometry (RBS) has several applications:

- Composition determination to within 3% of the atomic mass

- Thickness determination of thin films, to within 5 nm
- Crystallinity (when measured in Channeling Mode).

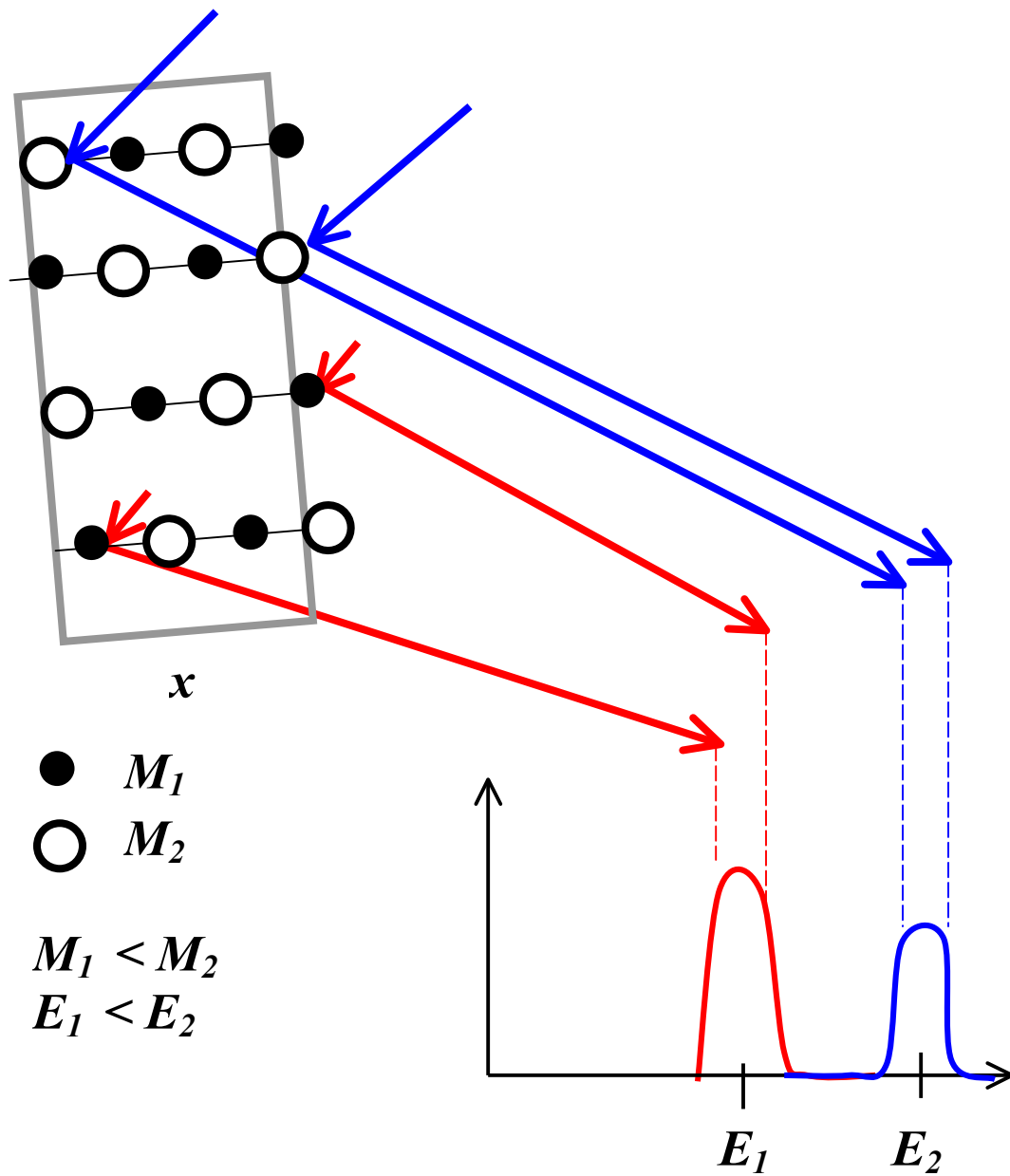


Figure 48 Diagram of RBS in randomly aligned mode for a binary system (such as ZnO). Arrows indicate incident and backscattered energy.

*Elemental Composition:*

The energy of the backscattered particle is influenced primarily by the atomic mass in the sample and the scattering angle—the higher the backscatter energy, the higher the atomic mass:

$$\frac{E_{backscatter}}{E_{initial}} = 1 - \left[ \frac{2M_2M_1}{(M_1 + M_2)^2} \right] (1 - \cos\theta) \quad (\text{A4.1})$$

Where  $E_{initial}$  = energy of the incident  $\alpha$ -particles,  $M_1$  = atomic mass of the incident particle,  $M_2$  = atomic mass of the sample under study.

The number of backscattered particles that have been detected is known as the yield,  $Y$ , and is defined as:

$$Y = QN_s \left( \frac{d\sigma}{d\Omega} \right) \Delta\Omega \quad (\text{A4.2})$$

Where  $Q$  = number of incident ions,  $N_s$  = surface density (atoms/cm<sup>2</sup>),  $\left( \frac{d\sigma}{d\Omega} \right)$  = the probability that a collision will result in a detected particle, the differential cross-section; and  $\Delta\Omega$  = the solid angle of the detector.

The differential cross-section is<sup>178</sup>:

$$\left( \frac{d\sigma}{d\Omega} \right) = \left( \frac{Z_1Z_2e^2}{4E} \right) \left( \frac{4}{\sin^4\theta} \right) \frac{\left\{ \left[ 1 - \left( \frac{M_1}{M_2} \sin\theta \right)^2 \right]^{1/2} + \cos\theta \right\}^2}{\left[ 1 - \left( \frac{M_1}{M_2} \sin\theta \right)^2 \right]^{1/2}} \quad (\text{A4.3})$$

*Film Thickness:* The film's thickness,  $t$ , is determined by measuring the width of the peak(s) of the constituent element,  $\Delta E$ . This must be normalized by the

stopping power,  $S_o$ , (expressed in units of [eV/Å]) which is the rate of energy loss of the  $\alpha$ -particles as a function of penetration depth:

$$\Delta E = S_o t \quad (\text{A4.4})$$

*Crystallinity:* The degree of crystalline order in a film or single crystal material is determined via RBS by operating the spectrometer in Ion Channeling Mode. In this mode, any rows of atoms that are aligned with the  $\alpha$ -particles beam will allow the beam to pass—a typical lattice spacing is on the order of Ångstroms, whereas a  $\alpha$ -particles has a wavelength that is  $10^4$  times smaller (for MeV operations). So, an  $\alpha$ -particles can move as a point particle through the channels defined by the lattice structure. The degree of crystallinity is expressed as the percent channeled (%  $\chi$ ), is a percentage that is calculated relative to the random (unaligned) backscattered signal. A specimen with “excellent” channeling (typically a single crystal) has  $\chi \sim 1\text{-}2\%$ .

Near-perfect channeling would imply little to no backscattering, since the  $\alpha$ -particles would be able to pass through the perfectly aligned “channels” of the lattice. Any misalignment of the lattice serves as barriers for further travel (see the picture on the right in the figure below). Consequently, backscattering of an element can occur. So, when aligned, samples that do not channel well will have backscattered signals with larger amplitudes compared to those that do channel well. A typical  $\chi$  for such a specimen is  $>10\%$ .

In channeling mode, the backscattered yield is often higher at the surface than it is in the bulk. This gives rise to a surface peak<sup>179</sup>.

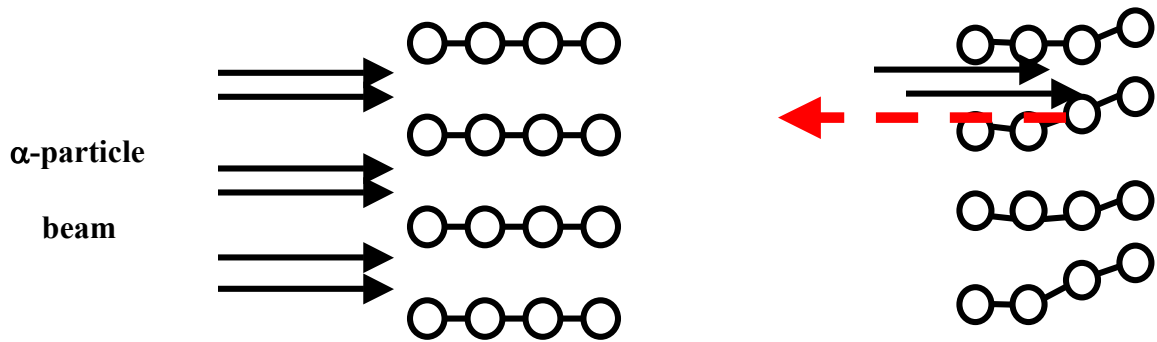


Figure 49 RBS Channeling Modes. (a) Channeling in a perfectly aligned lattice. (b) Channeling in an imperfect lattice. The backscattered element, a consequence of the imperfection of the lattice is represented by the dashed arrow.

### Limitations

RBS is unable to measure low-Z elements, such as oxygen, unless it is measured in a special resonance mode, where oxygen concentration is then measurable with an accuracy of  $\sim 3\%$ . Furthermore, elements with neighboring Z values may not possess readily resolvable peaks, depending upon the thickness of the film containing that element.

## A4.2 Experimental Details

$\alpha$ -particles are generated in a Pelletron, which is an electrostatic accelerator. Pellets made of insulating material, linked to one another to form a chain (similar to a belt in a Van der Graaf generator), are used to build up an electrical potential. The pellet chain is housed in a vessel containing  $\text{SF}_6$ , which serves to isolate the chain. The resulting voltage gradient is used to accelerate  $\alpha$ -particles towards the specimen<sup>180</sup>.  $\alpha$ -

particles collide with the specimen and by classical mechanics, momentum transfer occurs and an atom of a particular  $Z$  is scattered back into a detector.

The beam used in this dissertation was  $\sim 2$  MeV. Samples were mounted on a four-axis goniometry to permit alignment of the crystal for the purposes of channeling measurements (discussed below).



Figure 50 Photograph of Pelletron accelerator and RBS beam line (Courtesy of S. Dhar)

## Appendix 5: X-ray Photoelectron Spectroscopy

### A5.1 Introduction

X-ray photoelectron spectroscopy (XPS) is a technique for determining surface composition based on the photoelectric effect. A sample is placed under ultrahigh vacuum conditions (typically  $10^{-11}$  Torr) and irradiated with x-ray photons from an x-ray tube (or in some cases a synchrotron). Via the photoelectric effect, the surface atoms eject an electron from the core-level of the electronic structure. The electrons are separated according to energy in a hemispherical analyzer and counted.

The energy of the emitted electrons is related to the atomic bonding environment at the surface and is referred to as the *binding energy*,  $E_B$ . The number of emitted electrons that are collected at a given energy is related to the concentration of the particular atomic bonding state of an element. So, the kinetic energy of the electrons ejected from the solid are related to the binding energy ( $E_B$ ) and incident energy of the x-ray photons ( $h\nu$ ) and the spectrometer work function,  $\phi_{\text{spectrometer}}$ , via:

$$E_{\text{KE}} = h\nu - E_B - \phi_{\text{spectrometer}} \quad (\text{A5.1})$$

## A5.2 Experimental Details

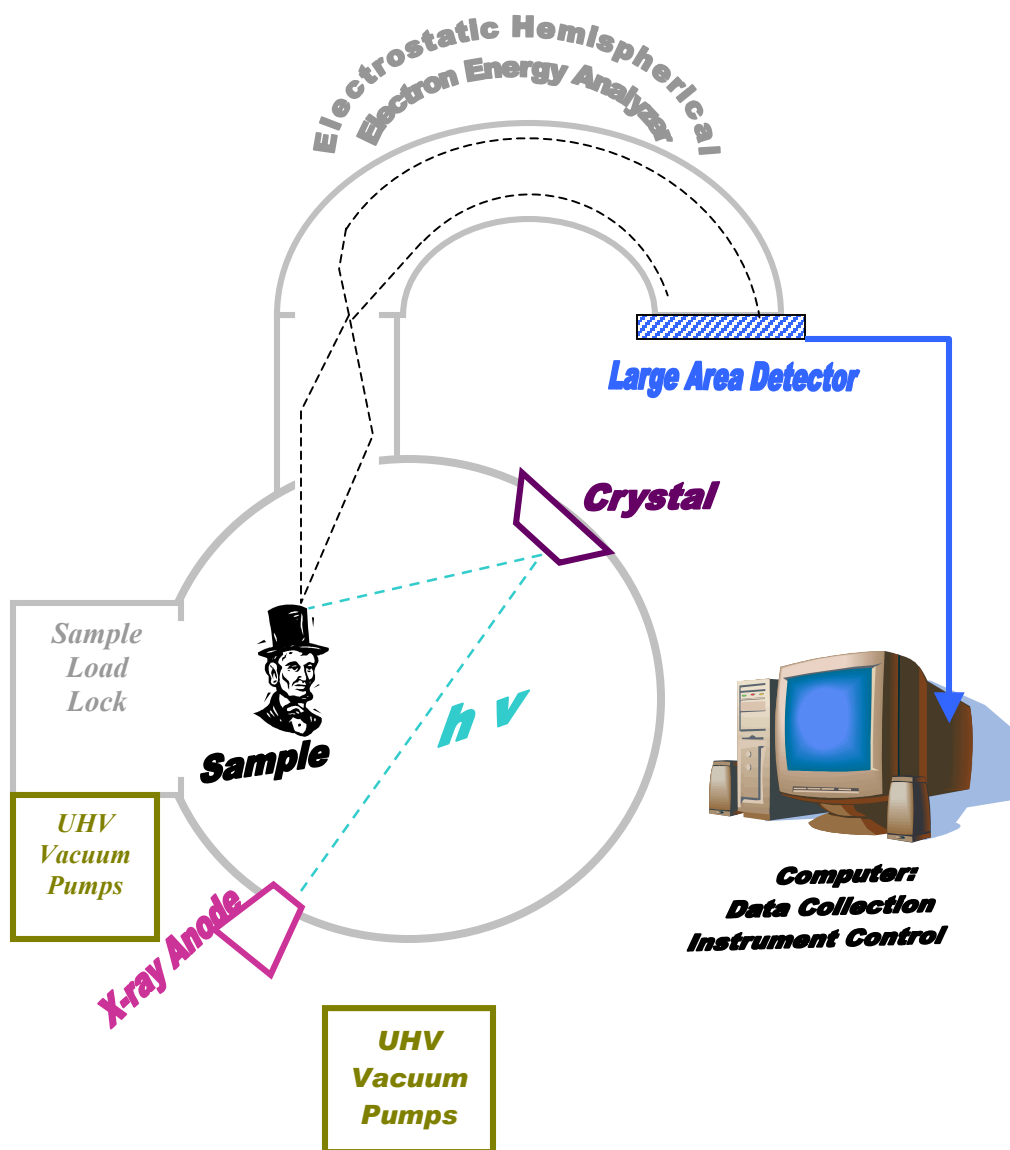


Figure 51 Top view schematic of X-ray Photoelectron Spectroscopy setup.

### A5.3 Analysis

Typically the 1s peak for carbon is found at 285.0 eV. Deviations from this value set the scale for the surface charge energy,  $E_{Ch}$ , which adds another correction term to the  $E_{KE}$  equation:

$$E_{KE} = h\nu - E_B - \phi_{\text{spectrometer}} - E_{Ch} \quad (\text{A5.2})$$

The precise  $E_B$  for a given atom on the surface depends upon its local chemical environment. Variations in the degree of attraction or repulsion between core-level electrons and the nucleus give rise to variations in  $E_B$ . These are known as *chemical shifts*. For example, if a collection of atoms of the same element have two oxidation states—those atoms with a high oxidation state will have a lot of valence electrons to donate and so will produce an XPS peak that is chemically shifted to a higher  $E_B$  compared to atoms at the lower oxidation state. The lower oxidation state has fewer core-level electrons interacting with the nucleus and so the strength of interaction between the core level electrons and the nucleus is weaker, hence the binding energy is lower. Electronegativity effects also drive chemical shifts. For example, a typical hydrocarbon bond C-H has a C1s binding energy of 285.0 eV. If a fluorine atom is bound to carbon (C-F), the C1s binding energy shifts to 287.8 eV.

The area under an XPS peak is related to the quantity of each element present. By measuring peak areas and adequately correcting peak position relative to the adventitious carbon peak position, it is possible to determine the % composition of a given element:

$$I_{ij} = K T(E_k) L_{ij}(\gamma) \sigma_{ij} \int n_i(z) e^{-z/\lambda(E_k)\cos\theta} dz \quad (\text{A5.3})$$

Where:

- $I_{ij}$  = the area of the peak j from element i
- $K$  = instrument specific constant
- $T(E_k)$  = transmission function of the analyzer
- $L_{ij}(\gamma)$  = angular asymmetry factor for orbital j of element i
- $\sigma_{ij}$  = photoionization cross-section of peak j from element i
- $\lambda(E_k)$  = inelastic mean free path length
- $\theta$  = take-off angle of the photoelectrons measured relative to the surface normal

## **Appendix 6: Four-Circle X-ray Diffraction**

### **A6.1 Introduction**

X-ray diffraction is a powerful technique for microstructural investigation of a material's properties. These properties include: atomic spacing, phase composition, epitaxy, crystallinity, grain size and defect structure. It is a non-destructive technique.

Crystals consist of atomic planes spaced some distance,  $d$ , apart. X-rays from an x-ray tube source (here, a Cu source) are diffracted by atomic planes in the crystal, constructively interfering and giving rise to a measurable diffraction peak. The condition for constructive interference is given by Bragg's Law:

$$n\lambda = 2d_{hkl} \sin \theta_{hkl} \quad (\text{A6.1})$$

Where  $n$  = the order of diffraction,  $d_{hkl}$  = d-spacing between  $(hkl)$  planes,  $\theta_{hkl}$  is the angle between atomic planes and the incident x-ray beam and  $\lambda$  is the wavelength of the incident x-ray beam ( $\lambda = 1.54066\text{\AA}$ , for the Cu  $K_\alpha$  line). In order to observe the diffraction peak, the detector is at  $2\theta_{hkl}$ .

In the case of thin films, a distribution of orientations is visible. In this case, the diffracted x-rays emerge as a cone with an opening about  $2\theta_{hkl}$ . The most common geometry for observing thin films is the Bragg-Bretano geometry<sup>181</sup>. In this geometry, x-rays are incident upon the sample at an angle  $\theta$ . The sample is rotated at  $\frac{1}{2}$  the

angular velocity of the detector. In this geometry, only information about the (hkl) planes parallel to the surface is obtained because the incident and diffracted x-rays are at the same angle relative to the sample surface.

Interplanar spacing is seldom uniform. Deviations from the standard value of interplanar spacing are associated with strain. The effect of strain, to a first approximation, is a superposition of diffraction lines shifted away from the unstrained position at a range of  $d$ -values, with the intensity of those lines reflecting the distribution of strain.

When the detector is set to a fixed  $2\theta$  value, satisfying the Bragg condition at a given  $d$  value and the sample is moved along (“rocked”) in  $\theta$ , the resulting peak that is measured is an indicator of the degree of crystallinity of the film. That is to say that it is a measure of the degree of misorientation.

## **A6.2 Experimental Details**

A Siemens D5000 X-ray diffractometer with  $\text{CuK}_\alpha$  source was operated at 40kV, 30mA. All thin film measurements commenced with substrate alignment. Scans of film peaks were aligned in  $\phi$  and  $\chi$  prior to all measurements.

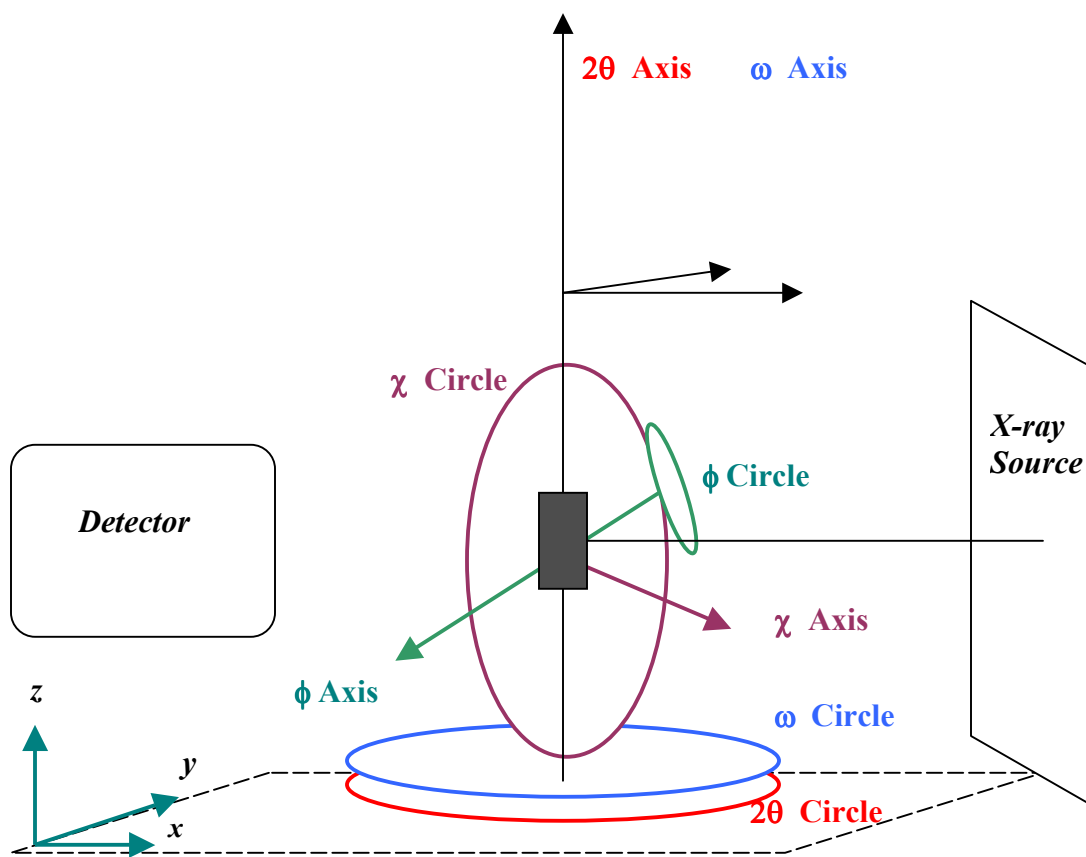


Figure 52 Diagram of XRD four-circle.

## Appendix 7: I-V and Schottky Barrier Measurements

### A7.1 Introduction

When a metal is placed in contact with a semiconductor,  $E_{\text{Fermi}}$  of the metal and semiconductor come into equilibrium in the absence of an externally applied electric field. As they come into equilibrium, a potential barrier between the metal and the semiconductor forms. This barrier is known as a Schottky barrier. In this case, the contact has diode-like (non-linear) I-V characteristics. In some cases, there is no potential barrier at the surface and thus, the contact is a conventional Ohmic contact and has conventional (linear) I-V characteristics.

Schottky barriers arise because of a difference between the positions of  $E_{\text{Fermi}}$  in a metal vs. in a semiconductor. In equilibrium, the  $E_{\text{Fermi}}$ s of the two different materials must line up. In order for this to occur, electrons will flow from the semiconductor into the metal, leaving empty, ionized states behind. These states, combined with their recently-flowed electron counterparts on the other side of the interface, produce a dipole electric field (and its associated potential). The potential associated with this dipole is continuous, decaying into the semiconductor as one moves away from the metal-semiconductor interface. Using Poisson's equation it can be written as:

$$\phi(x) = \frac{-qN_d}{2\epsilon}(x - x_o)^2 \quad (\text{A7.1})$$

Where  $N_d$  = donor concentration,  $x$ —distance away from the metal-semiconductor interface and  $x_o$  = position of the interface. It is the potential that gives rise to band-bending at the metal-semiconductor interface.

In order for electrons to flow, the potential barrier associated with the band bending must be overcome. This barrier is known as the *Schottky barrier*,  $\phi_B$ , and is dependent upon the metal as well as the processing conditions.  $e\phi_B = e\phi_{\text{vacuum}} - e\chi$ .

Where  $\phi_{\text{vacuum}}$  is the work function and  $\chi$  is the electron affinity (see diagram).

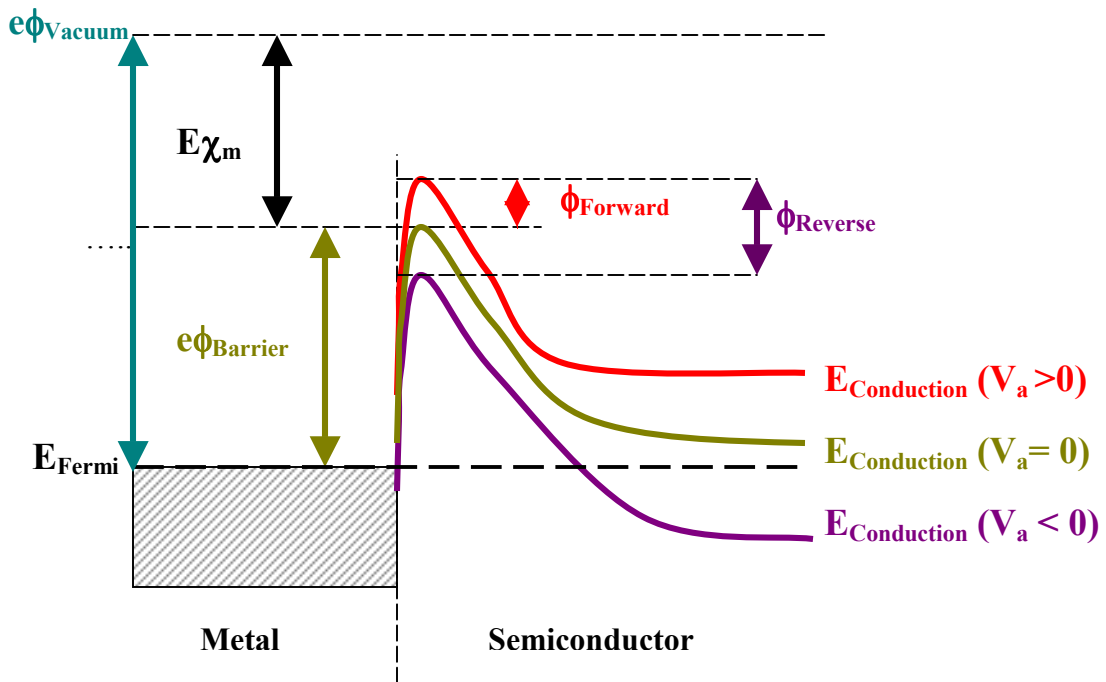


Figure 53 Diagram of band-bending and Schottky barrier for various applied voltages (not to scale!)

## A7.2 Experimental Details

An I-V measurement setup was constructed for the purposes of measuring low-noise, low-current measurements. A photograph of the probe station setup is shown in

Fig. 60. All measurements were made in a dark room, after 2-3 hours of settling in the darkness in order to minimize effects from persistent photoconductivity.

A Keithley 2400 Sourcemeter was connected to tungsten or beryllium-tungsten probe tips using coaxial test leads. The sample stage was guarded. Test leads were cleaned with methanol and a lint-free wipe prior to each run. Unconnected, the minimum measurable current through the leads was  $4 \times 10^{-11}$  Amps.

The Keithely Sourcemeter was controlled via LabView virtual instruments written for the purposes of I-V testing. Test resistors as well as test diodes were run in order to investigate the limits of the constructed system.

Au was used as the Schottky contact and soldered In were used as the Ohmic contact.<sup>182</sup>

Samples were measured between [-5, +5] V with 0.05 V steps. Measurements were averaged 5 times with a 5 second wait between voltage steps. Measurements were repeated in loops in 6 hour intervals to test for variations associated with persistent photoconductivity.

### A7.3 Analysis

The forward current can be written as:

$$I = I_s \exp\left(\frac{e(V_a - IR_s)}{nk_B T}\right) \quad (\text{A7.2})$$

Where  $e$  = charge of the electron,  $V_a$  = applied voltage,  $R_s$  = series resistance of the Schottky junction,  $T$  = temperature,  $I$  = measured current,  $n$  = ideality factor and  $I_s$  = saturation current, which is defined as<sup>183</sup>:

$$I_s = A^* T^2 \exp\left(\frac{-\phi_B}{nk_B T}\right) \quad (\text{A7.3})$$

Where  $A^*$  = Richardson constant for ZnO is =  $32 \text{ A cm}^{-2} \text{ K}^{-2}$  <sup>184,185</sup>.

The barrier height was calculated by extrapolating the  $\ln(I)$  vs.  $V$  curve to  $V = 0$ . This gives  $I_s$ . From this it is possible to determine the barrier height by inverting the previous equation such that<sup>186</sup>:

$$\phi_B = \frac{k_B T}{q} \ln\left(\frac{A^* T^2}{I_s}\right) \quad (\text{A7.4})$$

## Suggested Interview Questions for the Dissertation Defense

*My thanks to the principal and staff of Hollywood Elementary School, College Park, for the opportunities to judge their science fairs, participate in their career fairs and allow me to reproduce these questions (from their 2006 Science Fair) in my thesis!*

*Perhaps the committee will find this useful during the defense!*

<b>Project Area</b>	<b>Suggested Questions</b>
<i>Purpose/Question</i>	-Why did you select this project? -How did you develop an interest in this topic?
<i>Prediction/Hypothesis</i>	-Before you started, what did you think was going to happen in your investigations? -Why did you think that was going to happen? -What information did you get from your research?
<i>Materials and Procedures</i>	-What did you make sure to keep the same during your investigation? -Why did you use “x” samples in your investigation? -Why is it important to use metric units in your investigation? -Can you identify the independent variable? -Can you identify the dependent variable?
<i>Results</i>	-Can you use your graph to explain your experiment? -If you continued this investigation for a longer period of time, what might happen? -If you used _____ instead of _____, would you get the same results? Why or why not? -What pattern or trend does your graph show? -If your graph were to continue in such a pattern or trend, what might you conclude?
<i>Conclusion</i>	-What did you find out in your investigation? -What did you learn about your hypotheses or predictions? -How does your topic relate to real life? -How could you continue testing or experimenting to learn more about your topic? -Can you think of any new questions you might want to investigate that are related to your topic? -How could the information you found out in your project help someone in their career?

## Bibliography

- 
- <sup>1</sup> H.E. Brown, *Zinc Oxide Rediscovered*, (N.J. Zinc Company, N.Y., 1957).
  - <sup>2</sup> F. Seitz, *The Modern Theory of Solids* (Mc-Graw Hill Book Company, N.Y. 1940), p 448.
  - <sup>3</sup> J. Zhu, N.W. Ementoglu, Y. Chen, B.V. Yakshinsky and Y. Lu, *J. Elect. Mat.* **33**, 556 (2004).
  - <sup>4</sup> Ü. Özgür, *J. Appl. Phys.* **98**, 041301 (2005).
  - <sup>5</sup> See, for example: D.C. Look, *et al.*, *Appl. Phys. Lett.* **75**, 811 (1999) or A.Y. Polyakov, *et al.* *J. Appl. Phys.*, **94**, 2895 (2003).
  - <sup>6</sup> Cermet Corporation, Private Communication, 2005.
  - <sup>7</sup> C. Kittel, *Introduction to Solid State Physics*, (John Wiley & Sons, New York, 1971), p 376.
  - <sup>8</sup> G.A. Baraff and M. Schluter, *Phys. Rev. Lett.* **55**, 1327 (1985).
  - <sup>9</sup> F.A. Kroger and H.J Vink, *Solid State Physics* **III**, 310 (1956).
  - <sup>10</sup> G. Mandel, *Phys. Rev.* **134**, A1073 (1964).
  - <sup>11</sup> Y. Tsur and I. Riess, *Phys. Rev. B* **60**, 8138 (1999).
  - <sup>12</sup> For example, Walukiewicz, *J. Vac. Sci. Tech.* **B5**, 1062 (1987); Walukiewicz, *Appl. Phys. Lett.* **54**, 2094 (1989); Walukiewicz, *J. Vac. Sci. Tech.* **B6**, 1257 (1988).
  - <sup>13</sup> W. Faschinger, *J. Cryst. Growth* **159**, 221 (1996).
  - <sup>14</sup> S.B. Zhang, S. Wei, & A. Zunger, *J. Appl. Phys.* **83**, 3192 (1998).

- 
- 15 S.B. Zhang, S.-H. Wei and A. Zunger, *J. Appl. Phys.* **83**, 3192 (1998).
- 16 C.G. Van de Walle and J. Neugebauer, *Nature* **423**, 626 (2003).
- 17 C. Kittel, *Introduction to Solid State Physics*, (Wiley, Singapore, 1971) p 202-3.
- 18 S.B. Zhang, S.-H. Wei and A. Zunger, *J. Appl. Phys.* **83**, 3192 (1998).
- 19 D.M. Smyth, *The Defect Chemistry of Metal Oxides*, (Oxford University Press, Oxford, 2000, p 37).
- 20 H. Geistlinger, *J. Appl. Phys.*, **80**, 1370 (1996).
- 21 S.B. Zhang, S.H. Wei, A. Zunger, *Phys. Rev. Lett.* **63**, 075205 (2001).
- 22 A.R. Hutson, *Phys. Rev.* **108**, 222 (1957).
- 23 S.E. Harrison, *Phys. Rev.* **93**, 52 (1954).
- 24 F. Oba *et al.*, *J. Appl. Phys.* **90**, 824 (2000).
- 25 A. R. Hudson, *Phys. Rev.* **108**, 222 (1957).
- 26 E. Zeigler, *et al.*, *Phys. Status Solidi A* **66**, 635 (1981).
- 27 T. Minami *et al.*, *Jpn. J. Appl. Phys.* **23**, L280 (1983).
- 28 R.-J. Hong *et al.*, *J. Cryst. Growth* **249**, 461 (2003).
- 29 H. Tanaka *et al.*, *J. Vac. Sci. Tech. A* **22**, 1757 (2004).
- 30 T. Minami, *MRS Bull.* **25**, 38 (2002).
- 31 S.E. Harrison, *Phys. Rev.* **93**, 52 (1954).
- 32 S.B. Zhang, S.H. Wei, and A. Zunger, *Phys. Rev. B*, **63**, 075205.
- 33 For example, S.-H. Wei & S.B. Zhang, *Phys. Status Solidi b* **229**, 305 (2002).
- 34 L. Pauling, *The Nature of the Chemical Bond and Structure of Molecules and Crystals*, (Cornell University Press, New York, 1960).
- 35 C.G. Van de Walle, *J. Vac. Sci. Tech. A* **21**, S182 (2003).

- 
- 36 D.B. Laks, C.G. Van der Walle, G.P. Newmark and S.T. Pantelides, *Phys. Rev. Lett.* **66**, 648 (1991).
- 37 G. F. Neumark, *Phys. Rev. Lett.*, **62**, 1800 (1989).
- 38 A. Weber, P. Sutter, H. von Kanel, *J. Appl. Phys.* **75**, 7448 (1994)
- 39 G. Mandel, *Phys. Rev.* **134** A1073 (1964).
- 40 C.G. Van de Walle, *Phys. Rev. Lett.* **85**, 1012 (2000).
- 41 C.G. Van de Walle, *Phys. Stat. Sol. B* **229**, 221 (2002).
- 42 T.V. Butkhuzi *et al.* *J. Cryst. Growth* **117**, 366 (1992).
- 43 G. Xiong *et al.*, *Appl. Phys. Lett.* **80**, 1195 (2002).
- 44 S. Tüzemen *et al.*, *Physica B* **308-310**, 1197 (2001).
- 45 S. Tüzemen *et al.*, *Phys. Stat. Sol. A* **195**, 165 (2003).
- 46 S.-K. Kim *et al.*, *Appl. Phys. Lett.* **85**, 419 (2004).
- 47 M.G. Wandell, J.P. Goss and P.R. Briddon, *Phys. Rev. B* **71**, 155205 (2005).
- 48 E.-C. Lee, & K.J. Chang, *Phys. Rev. B* **70**, 115210 (2004).
- 49 Y. Kanai, *Jpn. J. Appl. Phys.* **1**Short Notes, **30**, 2021 (1991).
- 50 See analysis in S. Chopoon, Dissertation, University of Maryland, 2001.
- 51 M. Joseph, H. Tabata, T. Kawai, *Jpn. J. Appl. Phys.* **38**, L1205 (1999).
- 52 M. Joseph, H. Tababta, and T. Kawai, *Jpn. J. Appl. Phys. Part : Lett.* **38** (11A) L1205 (1999).
- 53 A. Kobayashi, O.F. Sankey, J.D. Dow, *Phys. Rev.*, **B28**, 946 (1983).
- 54 R.D. Shannon and C.T. Prewitt, *Acta Cryst.* **B25**, 925 (1969). An interactive version of this data can be found at:  
<http://abulafia.mt.ic.ac.uk/shannon/ptable.php>

- 
- 55 T. Yamamoto, in *Defect and Impurity Engineered Semiconductors and Devices III*, (Materials Research Society Proceedings, 2002)
- 56 J. Misiewicz, *J. Phys: Condens. Matter* **2**, 2053 (1990).
- 57 For Phosphorous: T.L. Chu, *et al. J. Appl. Phys.* **54** 2063 (1983).  
For Arsenic: F. Matossi and F. Stern, *Phys. Rev.* **111**, 472 (1958).  
For Antimony: R.G. Breckenridge *et al.*, *Phys. Rev.* **96**, 571 (1954); H. Komiya, K. Matsumito, and F.Y. Fan, *Phys. Rev.* **133**, A1679 (1964); P.J. Shaver, *Phys. Rev.* **141**, 649 (1966)
- 58 C.-C. Lin, *et al., Appl. Phys. Lett.* **84**, 5040 (2004).
- 59 H. Matsui *et al., J. Appl. Phys.*, **95**, 5882 (2004).
- 60 Y. Yan, S.B. Zhang, S.T. Pantelides, *Phys. Rev. Lett.*, **86**, 5723 (2001).
- 61 A. Tsukazaki, *et al., Nature Materials* **4**, 42 (2005).
- 62 T.M. Barnes, K. Olson and C.A. Wolda, *Appl. Phys. Lett.* **86**, 112112 (2005).
- 63 Y. Yan, S.B. Zhang, S.T. Pantelides, *Phys. Rev. Lett.*, **86**, 5723 (2001).
- 64 A. Kobayashi, O.F. Sankey, J.D. Dow, *Phys. Rev.* **B28**, 946 (1983).
- 65 T. Aoki, Y. Hatanaka, D.C. Look, *Appl. Phys. Lett.* **76**, 3257 (2000).
- 66 K.-K. Kim, *et al., Appl. Phys. Lett.* **83**, 63 (2003).
- 67 D.J. Chadi, *et al. Phys. Rev. Lett.* **79**, 4834 (1997).
- 68 D. J. Chadi, *Phys. Rev.* **B59**, 15181 (1999).
- 69 C.H. Park, S.B Zhang, S.-H. Wei, *Phys. Rev. B.* **66**, 073202 (2002).
- 70 R. M. Park, M. B. Troffer, C. M. Rouleau, J. M. Depuydt, and M. A. Haasse, *Appl. Phys. Lett.* **57**, 2127 (1990) and M. A. Haasse, J. Qiu, J. M. Deuydt, and H. Cheng, *Appl. Phys. Lett.* **59**,1272 (1991).

- 
- 71 Y.R. Ryu, T.S. Lee and H.W. White, *Appl. Phys. Lett.* **83**, 87 (2003).
- 72 Y.R. Ryu, T.S. Lee, J.H. Leem & H.W. White, *Appl. Phys. Lett.* **83**, 4032 (2003).
- 73 S. Limpijumnong, S.B. Zhang, S.-H. Wei and C.H. Park, *Phys. Rev. Lett.* **92**,  
155504 (2004).
- 74 T. Aoki, Y. Shimizu, A. Miyake, A. Nakamura, Y. Nakanishi and Y. Hatanaka,  
*Phys. Stat. Sol. B* **229**, 911 (2002).
- 75 J.L. Vossen, *Phys. Thin Films* **9**, 1 (1977) and A. Barker, S. Crowther, and D.  
Rees, *Sensors and Actuators A* **58** 229 (1997).
- 76 Ozgur *et al.*, *J. Appl. Phys.* **98**, 04301 (2005).
- 77 M.J. Stowell, *Thin Solid Films* **1**, 55 (1968).
- 78 T. Aoki, Y. Hatamake, D.C. Look, *Appl. Phys. Lett.* **76**, 3257 (2000).
- 79 A. Zunger, *Appl. Phys. Lett.* **83**, 57 (2003).
- 80 A. Kudo, H. Yanagi, K. Ueda, H. Hosono, H. Kawazoe and Y. Yano, *Appl.*  
*Phys. Lett.* **75**, 2851 (1999).
- 81 X. Liu, X. Wu, H. Cao, R.P. Chang, *J. Appl. Phys.* **95**, 3141 (2004).
- 82 I.L. Kim, S-H. Jeong, S.S. Kim, B.-T. Lee, *Semicond. Sci. Tech.* **19** L29 (2004).
- 83 O. Kluth *et al.*, *Thin Solid Films*, **442**, 80 (2003) and also P.F. Garcia, R.S.  
McLean, M.H. Reilley, and G. Nunes, *Appl. Phys. Lett.* **82**, 1117 (2003).
- 84 This setting is known to produce well-oriented ZnO films. See, for example:  
K.K. Kim *et al.* *J. Appl. Phys.* **87**, 3573 (2000).
- 85 Singh, Jasprit, *Electronic and Optoelectronic Properties of Semiconductor*  
*Structures*, (Cambridge University Press, Cambridge, UK, 2003) p 32, p 478-  
483.

- 
- 86 JCPDS Card Number 36-1451
- 87 S.O. Kucheyev, J.E. Bradby, J.S. Williams, C. Jagadish, M.V. Swain, *Appl. Phys. Lett.* **80**, 956 (2002).
- 88 Park, Zhang and Wei, *Phys. Rev. B* **66**, 07202 (2002).
- 89 C.H. Park, S.B. Wang, and S.-H. Wei, *Phys. Rev. B* **66**, 073202 (2002).
- 90 K.C. Ruthe, D.J. Cohen, and S.A. Barnett, *J. Vac. Sci. Tech.* **A22**, 2446 (2004).
- 91 G. Davies, *Identification of Defects in Semiconductors*, M. Stavola (Ed.), (Academic Press, NY, 1999), p 28.
- 92 Piprek, Joachim, *Semiconductor Optoelectronic Devices*, (Academic Press, New York, Elsevier Science, 2003), pp 13-39.
- 93 S.L. Chuang and C.S. Chang, *Semicond. Sci. Tech.* **12**, 252 (1997)
- 94 G.E. Pikus, *Sov. Phys. JETP* **14**, 899 (1962) and G.E. Pikus, *Sov. Phys. JETP*, **14**, 1075 (1962).
- 95 J.E. Rowe, M. Cardona and F.H. Pollak, *Solid State Comm.* **6**, 239 (1968).
- 96 V. Srikanth and D.R. Clark, *J. Appl. Phys.* **81**, 6361 (1997).
- 97 V. Srikanth and D.R. Clark, *J. Appl. Phys.* **81**, 6361 (1997).
- 98 From Landolt- Bornstein, *Semiconductor*, (Springer-Verlag, Berlin, 1982), vol. 17, pp 35-60:
- $$\epsilon_{xx} = \epsilon_{yy} = -C_{3333}/(C_{1133} + C_{2233}), \text{ where } C_{1133} = C_{2233} = 105.1 \text{ GPa and}$$
- $$C_{3333} = 210.9 \text{ GPa.}$$
- 99 See for example:
- B.W. Thomas and D. Walsh, *J. Phys. D: Appl. Phys.* **6**, 612 (1973);

- 
- E.V. Monakhov, J.S. Christensen, K. Maknys, B.G. Svensson, and A. Yu. Kuzentsov, *Appl. Phys. Lett.* **87**, 191910 (2005).
- <sup>100</sup> See U.S. Patents 5926727 (1999), 5629234 (1997), 5851909 (1998), 5656541(1997).
- <sup>101</sup> A. Wander, F. Scheden, P. Steadman, A. Norris, R. McGrath, T.S. Turner, G. Thornton, N.M. Harrison, *Phys. Rev. Lett.* **86**, 3811 (2001).
- <sup>102</sup> M. Kunat, St. Gil Girol, Th. Becker, U. Burghaus, Ch. Wöll, *Phys. Rev. B* **66**, 081402 (2002).
- <sup>103</sup> V. Staemmler, K. Fink, B. Meyer, D. Marx, M. Kunat, S. Gil Girol, U. Burghaus, and Ch. Wöll, *Phys. Rev. Lett.* **90**, 106102 (2003).
- <sup>104</sup> G. Kresse, O. Dulub and U. Diebold, *Phys. Rev. B* **68**, 245409 (2003).
- <sup>105</sup> V. Staemmler, *et al.* *Phys. Rev. Lett.* **90**, 106102 (2003).
- <sup>106</sup> R. Kahna, K. Ip, Y.W. Heo, D.P. Norton, S.J. Pearton, F. Ren, *Appl. Phys. Lett.* **85**, 3468 (2004).
- <sup>107</sup> A. Wander, *et al.*, *Phys. Rev. Lett.* **86**, 3811 (2001).
- <sup>108</sup> B.J. Coppa, R.F. Davis & R. J. Nemiach, *Appl. Phys. Lett.* **82**, 400 (2003).
- <sup>109</sup> R. Lindsay, C. A. Muryn, E. Michelangeli, G. Thornton, *Surf. Sci.* **565**, L283 (2004).
- <sup>110</sup> See, for example: S.B. Zhang and J.E. Northurp, *Phys. Rev. Lett.* **67**, 2339 (1991); D.G. Deppe and N. Holonyak, *J. Appl. Phys.* **64** R93 (1988) and R.W. Haliche, *J. Appl. Phys.* **62** 998 (1987).
- <sup>111</sup> C.R. Brundle, C.A. Evan, S. Wilson, *Encyclopedia of Materials Characterization*, (Materials Characterization Series, Butterworth, Oxford,

- 
- 1992) p 4 - 7
- 112 J.M. Shannon, *Solid-State Electronics* **19**, 537 (1976).
- 113 B.J. Coppa, R.F. Davis and R.J. Nemiach, *Appl. Phys. Lett.* **82**, 400 (2003).
- 114 R. Khanna, *et al.* *Appl. Phys. Lett.* **85**, 3468 (2004)
- 115 L.J. Brillson, *Surf. Sci. Rep.* **2**, 295 (1982).
- 116 <http://srdata.nist.gov/xps>, entry 23367
- 117 A.B. Velichenko *et al.*, *Appl. Surf. Sci.* **148**, 73 (1999).
- 118 M. Chen *et al.* *Appl. Surf. Sci.* **158**, 134 (2000).
- 119 Wagner, C. D.; Riggs, W. M.; Davis, L. E.; Moulder, J. F.; Muilenberg, G. E.;  
*Handbook of X-ray Photoelectron Spectroscopy*; (Perkin-Elmer Corporation,  
Physical Electronics Division: Eden Prairie, MN, 1979).
- 120 B. Domenichini, G. Pataut, S. Bourgeois, *Surf. And Interf. Anal.* **34**, 540 (2002).
- 121 <http://www.du.edu/~jcalvert/phys/zinc.htm#Chem>
- 122 Y.G. Wang *et al.*, *J. Appl. Phys.* **94**, 354 (2003).
- 123 L.C. Feldman, J.W. Mayer, S.T. Picraux, *Materials Analysis by Ion  
Channeling*, (Academic Press, New York, 1982) p 44-45.
- 124 P.S. Xu *et al.*, *Chin. Phys. Lett.* **15**, 457 (1998).
- 125 J. Carrasco, N. Lopez, and F. Illas, *Phys. Rev. Lett.* **93**, 22502 (2004).
- 126 J. Carrasco, N. Lopez, and F. Illas, *Phys. Rev. Lett.* **93**, 22502 (2004).
- 127 B.X. Lin *et al.*, *Appl. Phys. Lett.* **79**, 943 (2001).
- 128 Z.K. Tang *et al.*, *Appl. Phys. Lett.* **72**, 3270 (1998) and S. Cho *et al.* *Appl. Phys.  
Lett.* **75**, 2561 (1999).
- 129 S. Takata *et al.*, *Phys. Status Solidi A* **65**, k83 (1981)

- 
- 130 K. Vanhuedsen *et al.*, *J. Appl. Phys.* **79**, 7983 (1996).
- 131 B. Lin *et al.*, *J. Electrochem. Soc.* **148**, G110 (2001)
- 132 A.F. Kohan, *et al.*, *Phys. Rev. B.* **61**, 15019 (2000)
- 133 S.B. Zhang, S.H. Wei, and A. Zunger, *Phys. Rev. B* **23**, 579 (2001).
- 134 A. F. Kohan, G. Ceder, D. Morgan, and C. G. Van de Walle, *Phys. Rev. B* **61**,  
15019 (2000).
- 135 D. C. Reynolds, D. C. Look, B. Jogai, and H. Morkoc, *Solid State Comm.* **101**,  
643 (1997).
- 136 O.F. Schrimmer and D. Zwingel, *Sol. Stat. Comm.* **8**, 1559 (1970).
- 137 H.-J. Egelhaaf and D. Oelkrug, *J. Crystal Growth* **161**, 190 (1996).
- 138 T. Monteiro *et al.*, *J. Appl. Phys.* **98**, 013502 (2005).
- 139 B.K. Meyer *et al.*, *Phys. Status Solidi B* **241**, 231 (2004) and references therein.
- 140 Y.G. Wang, *et al.*, *J. Appl. Phys.* **94**, 354 (2003).
- 141 V.A. Karpina, *et al.*, *Crys. Res. Technol.* **11**, 980 (2004).
- 142 W.F. Zhang, Z. Yin, M.S., Z. I. Du and W.C. Chen, *J. Phys. Condens. Matt.* **11**,  
5655 (1999).
- 143 U. Ozgur *et al.*, *Appl. Phys. Lett.* **98**, 041301 (2005) and references therein.
- 144 D.C. Look, *et al.*, *J. Appl. Phys.* **81**, 1830 (2002).
- 145 D.W. Hamby, D.A. Lucca, and M.J. Klopstein, *J. Appl. Phys.* **97**, 043504  
(2005).
- 146 F.X. Xiu, Z. Yang, L.J. Manalapu, and J.L. Liu, *Appl. Phys. Lett.* **88** 152166  
(2006).
- 147 D.C. Reynolds *et al.*, *J. Lumin.* **82**, 173 (1999).

- 
- 148 Q.P. Wang *et al.*, *Optical Materials* **26**, 23 (2004).
- 149 Z.Q. Chen *et al.*, *J. Appl. Phys.* **97**, 013528 (2005).
- 150 V. Vaithianathan, B.-T. Lee, S.S. Kim, *J. Appl. Phys.* **98**, 043519 (2005).
- 151 Y.D. Kuo, *Appl. Surf. Sci.* **202**, 266 (2002).
- 152 K.-K. Kim *et al.*, *Appl. Phys. Lett.* **83**, 63 (2003).
- 153 V. Vaithianathan, B.-T. Lee, S.S. Kim, *J. Appl. Phys.* **98**, 043519 (2005).
- 154 Z.G. Yu, H. Gong, P. Wu, *Appl. Phys. Lett.* **86**, 212105 (2005).
- 155 F.L. Katknack and F.A. Hummel, *J. Electrochem. Soc.* **105**, 132 (1958).
- 156 Binary Alloy Phase Diagrams, page 1833
- 157 Maxwell, Hendricks, and Deming, *J. Chem. Phys.* **5**, 626 (1937).
- 158 R. Ghosh and D. Basak, *J. Appl. Phys.* **96**, 2689 (2004).
- 159 D.L. Smith, *Thin-Film Deposition: Principles and Practice*, (McGraw Hill, New York, 1995), p 229.
- 160 See, for example:
- T. Peng *et al.*, *Appl. Phys. Lett.* **71**, 2439 (1997),
- S.Z. Wang, *et al.*, *J. Appl. Phys.* **96**, 2010 (2004).
- 161 L.J. van der Pauw, *Phillips Res. Rep.* **13**, 1 (1958).
- 162 ASTM, "Standard Method for Measuring Resistivity, Hall Coefficient, and Determining Hall Mobility in Extrinsic Semiconductor Single Crystals," F76, 1985.
- 163 Z. Ndlela, C.W. Bates, *Rev. Sci. Instr.* **60**, 3482 (1989); D.A. Anderson and N. Apsley, *Semicond. Sci. Technol.* **1**, 187 (2002).
- 164 See, for example:

- 
- V. Vaithianathan, B.-T. Lee, S.S.Kim, *J. Appl. Phys.* **98**, 043319 (2005).
- 165 A.R. Hutson, *Phys. Rev.* **108**, 222 (1957).
- 166 See, for example:
- V. Vaithianathan, B.-T. Lee, S.S.Kim, *J. Appl. Phys.* **98**, 043319 (2005).
- 167 Antimony: *Appl. Phys. Lett.* **87**, 152101 (2005); Nitrogen: *Appl. Phys. Lett.* **87**,  
092101 (2005); *Appl. Phys. Lett.* **85**, 4070 (2004); Oxygen: *Appl. Phys. Lett.* **80**,  
1195 (2002).
- 168 B. Santic, *Semicond. Sci. Tech.* **18**, 219 (2003) and references therein.
- 169 C. Van der Walle, private communication, 2006
- 170 W. Walukiewicz, *J. Cryst. Growth* **159**, 244 (1996).
- 171 M. Shim and P. Guyot-Sionnest, *J. Am. Chem. Soc.* **123** 11651 (2001)
- 172 N.N. Srybu, I.M. Tiginyanu, V.V. Zalamai, V.V. Ursaki, and E.V. Rusu,  
*Physica B* **353**, 111 (2004).
- 173 Y.W. Heo, *et al.*, *Appl. Phys. Lett.* **83**, 1128 (2003).
- 174 E.E. Hahn, *J. Appl. Phys.* **22**, 855 (1951).
- 175 M. H. Francombe, *Growth of Epitaxial Films*, in *Epitaxial Films*, J.W. Matthews  
(Ed.), (Academic Press, New York, 1975), pp 109-182.
- 176 J.I. Pankove, *Optical Processes in Semiconductors*, (Dover Publications, New  
York, 1971).
- 177 E. Rutherford, *Phil. Mag.* **C21**, 669 (1991).
- 178 C.W. Magee & L.R. Hewitt, *RCA Review* **47**, 162 (1986).
- 179 J. Perriere, *Vacuum* **37**, 429 (1987).
- 180 <http://www.eagelabs.com/en-US/references/tutorial/rbstheo/cairtheo.html>

- 
- <sup>181</sup> C.R. Brundle, C.A.Evans, Jr. and S. Wilson, *Encyclopedia of Materials Characterization*, (Materials Characterization Series, Butterworth, Oxford, 1992) p 198.
- <sup>182</sup> K. Ip, Y.W. Heo, K.H. Paik, D.P. Norton, S.J. Pearton and F. Ren, *J. Vac. Sci. Tech.* **B22**, 171 (2004).
- <sup>183</sup> S.M. Sze, *Physics of Semiconductor Devices*, (Wiley Interscience, New York, 1981), p 250-254.
- <sup>184</sup> H. von Wenckstern, *et al.*, *Appl. Phys. Lett.* **84**, 79 (2004).
- <sup>185</sup> S.M. Sze, *Physics of Semiconductor Devices*, (Wiley Interscience, New York, 1981), p 849.
- <sup>186</sup> D.K. Schroder, *Semiconductor Material and Device Characterization*, (Wiley Interscience, New York), 1998, p 170.